NiTi Super Elastic Shape Memory Alloys for Energy Dissipation in Smart Systems for Aerospace Applications

A Thesis Submitted to
Mangalore University
for the Award of Degree of

Doctor of Science

in

Materials Science

by

G.N.Dayananda

2008

Advanced Composites Division
National Aerospace Laboratories,
Bangalore-560017, India.

DECLARATION

I hereby declare that the matter embodied in this thesis entitled "**NiTi Super Elastic Shape Memory Alloys for Energy Dissipation in Smart Systems for Aerospace Applications**" is the result of the investigations carried out by me in the last decade.

In keeping with general practice of reporting scientific observations, due acknowledgement has been made whenever the work described is based on the findings of other investigators. Any omissions, which might have occurred by oversight or error in judgment, are regretted.

Place: Bangalore
Date : (G.N.Dayananda)

Acknowledgements

It is a great pleasure for me to place on record a deep sense of gratitude to Dr. Manjunatha Pattabi, Professor and Chairman, Department of Materials Science, Mangalore University for his guidance and invaluable suggestions during the preparation of this thesis.

I wish to record my sincere appreciation and gratitude to Dr.A.R.Upadhya, Director, National Aerospace Laboratories(NAL) for his encouragement and support in this work. I also thank Dr.B.R.Pai, Former Director, NAL with whom I have had good interaction . I take this opportunity to express my deep gratitude to my peers at NAL. They are; Mr.M.Subba Rao, Former Head, Advanced Composites Division, Dr.R.V.Krishnan, Former Head, Materials Science Division, Dr.T.G.Ramesh, Former Head, Materials Science Division, Dr.M.R.Madhava, Head & Mr.H.N.Sudheendra, Deputy Head of Advanced Composites Division for their constant help and encouragement.

I wish to express my sincere thanks to Prof. Jan Van Humbeeck of Catholic University, Belgium and Dr Petr Sittner of Institute Of Physics, Czech Republic with whom I have had very good interactions over the last decade.

I take this opportunity to express my gratitude to Dr. M. Chandrasekaran, Smatec, Belgium with whom I had several discussions in this area.

I wish to thank Mr. H.V.Ramachandra, Mr. Satisha, Mr. P.Senthil Kumar, Mr. G M Kamalakannan, Mr. B.Ramanaiah, Dr. Byji Varughese, Mr. G. Kotresh and Mr. C.Shivashankar at the Advanced Composites Division, NAL for their help. The help rendered by Mrs. Thanuja kumari of the Advanced Composites Division in typing this thesis is acknowledged. Thanks are also due to Mr. G.T. Harsha, Mr. R. Manjunath, Mr. S.K. Suresh Babu and Mr. Jagadeesh of the Advanced Composites Division for their help. The help rendered by Mr. K. Venkataramiah in the DSC measurements and Mr. M.A. Venkataswamy in the fractography from the Materials Science Division of NAL is gratefully acknowledged. The interaction with Mr. V. Shankar of structures division on various aspects of smart technologies is gratefully acknowledged. I thank Dr. S. Selvarajan for the useful discussions regarding the airship project. I thank Mr. S. R. Dey and the Head of ICAST, NAL for promptly responding to my request for a large number of research papers. My sincere thanks to Head, Joint Head and staff of KTMD for their support in this endeavor. I thank Dr. U.N.Sinha, Head, Flosolver Division at NAL who has constantly supported my research activities. Finally, I wish to thank my father, mother, wife, sister, niece, nephew and daughter who have constantly supported me in this effort.

List of Contents

Declaration ii

Acknowledgements iii

List of Acronyms viii

Preface x

List of Journal Publications/Patents/Invited Conference Papers xvi

1. General Introduction

1.1 Background 1

1.2 Polymeric Carbon Composites 2

1.3 Principles of Shape Memory 3

1.4 Thermal SMA and Applications 7

1.5 Heat treatment of SE SMAs 14

1.6 Sensory behavior of SE SMAs 16

1.7 Super elastic SMA and Other Energy Dissipating Materials 17

1.8 Modeling Fatigue Behaviour 23

1.9 Design & Development of Smart Landing Gear 27

1.10 Motivation and Objective 30

1.11 Brief Description of the Blimp (semi-rigid airship) & Structural Framework 32

1.12. Problem Definition 35

2. Material and Experimental Details:

2.1 Introduction 37

2.2 Materials used 38

2.3 Experimental details 41

2.4 Testing of Polymeric Composites 48

2.5 Testing of Landing gear sub unit containing SE SMA and Polymer composites 49

2.6 Testing of Dog ears 53

2.7 Rationale for the use of materials 55

3. Effect of Heat Treatment on Energy Dissipation:

3.1 Introduction 57

3.2 Optimized Energy Dissipating Characteristics 57

4. Sensory Behavior of NiTi SE SMA

4.1 Introduction 68

4.2 Sensory Characteristics of SE SMA 68

5. Strain Rate Effects:

5.1 Introduction 77

5.2 Issues in displacement measurements 78

5.3 Comparison of Energy Storage 79

5.4 Ductile Behavior of SE SMAs 80

5.5 Tensile behavior, fractography & cyclic testing for the 30 mm length wire 87

6. Cyclic and Fatigue behavior

6.1 Introduction 96

6.2 Cyclic Loading 98

6.3 Fatigue Behavior 103

7. Design, Fabrication, Testing and Analysis of the smart Landing Gear

7.1 Introduction 110

7.2 Design philosophy for the landing gear 112

7.3 Tensile Testing of Polymeric Composite Materials 119

7.4 Design and Testing of Dog Ears 125

7.5 Fabrication 127

7.6 Energy Dissipation process in Landing Gear 132

7.7 Design and Analysis 135

7.8 Testing of the smart landing gear 141

7.9 Comparison of analysis and testing 147

8. Conclusions 154

References 160

List of Acronyms

ADC : Analog to Digital Converter

A_f : Austenite finish temperature

A_s : Austenite start temperature

BD : Bidirectional

CFRP : Carbon fibre reinforced plastic

E : Young’s modulus

E_{SIM} : Young’s modulus of the elastic deformation of SIM

E_d : Dissipated strain energy per unit volume

E_r : Recoverable strain energy per unit volume

FEM : Finite Element Method

GFRP : Glass fibre reinforced plastic

HT : Heat treatment

i : Current

J : Joule

m : mèter

mA : milli amps

M_d : Maximum temperature at which martensite occurs with the assistance of an external stress

M_f : Martensite finish temperature

M_s : Martensite start temperature

MP : Mean point

N : Newton

N_f : Number of cycles to failure

NLA : Non Linear Analysis

R : Resistance

SIM : Stress induced martensite

SE : Super elastic

SMA : Shape memory alloy

SR : Strain Rate

t : time

UD : Unidirectional.

V : Voltage.

V_{SMA} : Voltage across SMA.

$\underline{V}$: Volume.

β : Slope of plastic strain per cycle vs. N_f curve.

ρ : Electrical Resistivity.

δ_h : Horizontal deflection.

δ_v : Vertical deflection.

σ : Stress.

σ_I : SIM plateau initiation stress.

σ_U : Unloading plateau stress

σ_{es} : Elastic region start stress (after end of SIM region).

σ_{Ult} : Ultimate stress.

σ_{lms} : Stress in the middle of the plateau.

ε_r : Residual strain

ε_p : Plastic Strain.

ε_t : Total strain.

ξ : SIM fraction.

.

Preface

Shape Memory Alloys (SMAs) have attracted the attention of a wide range of researchers from several disciplines. This is because they possess very special and unusual properties and have potential for use in numerous applications. The nuances and subtleties associated with these unusual properties indeed pose challenges for the discerning researcher and designer. Even more exciting and demanding is to conceive, build and test a device exploiting the intrinsic property of these materials for aerospace applications where the weight and volume budgets are most stringent. Such an effort would involve material characterization, arriving at the design envelope of the material and effectively integrating it into the device. The SMAs exhibit complex non-linear thermo–mechanical behavior. They exhibit hysteresis both in the thermal and stress loading domains. SMAs can undergo large pseudo elastic deformations (typically 4 – 6%) in the low temperature martensite phase at low stresses. These deformations are completely recovered on heating to the high temperature austenite phase. This effect which is thermally induced is known as the thermal Shape Memory Effect. There is also a large pseudo elastic deformation which results from the application of stress in SMAs. This is obtained by stressing the SMA (loading) in the austenite phase and inducing stress induced martensite (SIM). During the process of inducing the SIM, pseudo elastic deformations of the order of 6 – 8% accrue. These 'large pseudo elastic' deformations are completely recovered when the stress is removed from the material. The removal of stress (unloading) takes the material back to the austenite phase. The path taken during unloading is different from the path taken during loading resulting in a stress hysteresis. Associated with the stress hysteresis is the dissipation of energy in these materials which is several orders higher compared to conventional materials such as steels, aluminium or other metal systems. The objective here is to develop an alternate method to build an efficient smart landing gear device with superior energy dissipating features exploiting the large energy dissipating characteristics of Super Elastic (SE) SMAs applicable to a wide variety of vehicles. It is pertinent here to mention that polymeric carbon composites are gaining increased acceptance for airframes and other structural subsystems due to their superior stiffness and strength properties. The focus of this study is to systematically investigate the energy dissipation capability of NiTi SMA Systems and effectively blend them with carbon composites to realize efficient landing gear systems. The heat treatment given to the SE SMA materials hold the key to the control of their mechanical properties. Like other smart materials SE SMAs possess bi-functional properties. Associated with the energy dissipation characteristics is the sensory function of SE SMA. The study covers the effect of heat treatment on the energy dissipation characteristics, evaluation of the sensory behavior, effects of strain rate on energy dissipation and other related mechanical properties. It also details the design, fabrication, analysis and testing aspects associated with integrating the NiTi SMA with the polymeric carbon composite based smart landing gear system that is applicable to a large category of ground and air vehicles.

Chapter 1 deals with the mechanical properties of the advanced materials such as carbon and glass fiber reinforced plastics and SMAs. The comparison of the energy dissipation capability of SMAs in relation to other conventional materials is outlined. The principles of super elasticity are explained. The super elastic behavior of NiTi SMA is compared with a conventional helical steel spring.

Chapter 2 deals with the experiments to determine the optimum heat treatments, sensory characteristics, effect of a wide range of strain rates and temperatures on the energy dissipation and related parameters. These include the tensile tests upto failure, limited fractography studies on cold worked and heat treated samples. It also covers cyclic and fatigue tests for large fixed strain amplitudes. The testing details of the smart carbon composite landing gear incorporating SE SMA is presented. The three configurations of the smart landing gear testing with SE SMA, without SE SMA and with steel wire are discussed.

Chapter 3 deals with the heat treatment procedures in order to obtain the optimum energy dissipation characteristics. The comparison of the mechanical behavior of the cold worked and heat treated wire is covered. The maximum energy dissipation with the minimum remnant strain is identified.

Chapter 4 evaluates the sensory characteristics of the SE SMA. The sensory characteristics serve as a useful feedback to validate the design of the landing gear. This involves passing a small constant current in the SE SMA and measuring the voltage across the SE SMA. The changes in voltage are a measure of the strain in the landing gear SE SMA element.

Chapter 5 discusses the results relating to the strain rate, energy dissipation and ductility. In order to bring out the interplay of the ductile behavior, temperature, strain rate effects, energy storage/dissipation and cycling, the study focuses on 4 important topics: a) Comparison of the large energy storage capacity of NiTi SMAs with a conventional helical steel spring and aluminium strip. b) The quasi-static tensile behavior at different temperatures and strain rates backed by (limited) fractography studies. c) Effect of strain rate on the SIM (Stress Induced Martensite) and elastically deformed SIM segments. d) Effect of strain rate on cyclic properties.

Chapter 6 dwells on the cyclic and fatigue behavior and prediction of fatigue. The results of the cyclic testing relating to the experiments for a given strain rate for a range of cyclic strain amplitudes from 2-10% are presented. The stabilization of residual strain and energy dissipation is brought out. It also deals with the experimentation and prediction of fatigue using the Coffin-Manson relationship. The importance of the plastic strain evolution for the fatigue of the material is brought out.

Chapter 7 deals with the design, fabrication, analysis and testing of the SE SMA integrated polymer composite smart landing gear. The process of energy dissipation in the material when the landing gear impacts the ground is illustrated. It also discusses the following aspects of the landing gear for the three configurations: a) The combined benefit of CFRP beam, natural cane reinforced CFRP arch and SMA. b) The role of the SMA element as an energy-dissipating member. c) The comparison of SMA wire with a steel wire for energy dissipation.

Chapter 8 summarizes the work and lists the conclusions in relation to the energy dissipation characteristics over the wide range of strain rates and temperatures. It also brings out the bifunctionality of the SMA element. The superior energy dissipating characteristics of the SE SMA polymeric composite smart landing gear are brought out.

This work has benefitted from the extensive interactions the author has had over the last decade with the following eminent persons in the field.

1) Dr. Manjunatha Pattabi, Professor and Chairman, Department of Materials Science, Mangalore University.

2) Dr.R.V.Krishnan, Former Head, Materials Science Division, NAL, Bangalore.
3) Mr.M.Subba Rao, Former Head, Advanced Composites Division, NAL, Bangalore.
4) Dr.T.G.Ramesh, Former Head, Materials Science Division, NAL, Bangalore.
5) Prof. Jan Van Humbeeck of Catholic University, Belgium.
6) Dr. Petr Sittner of Institute of Physics, Czech Republic
7) Dr. A.R. Upadhya, Director, NAL, Bangalore.

I was fortunate to work with Prof. Jan Van Humbeeck, a renowned expert in the area of SMA research during my tenure as a Research Fellow at Catholic University, Belgium in 1999. Subsequently, I have led the efforts to set up a state-of-the-art SMA research laboratory at NAL. In recognition of these efforts, recently I was elected a fellow of “The Institution of Engineers (India)”. The SMA group at NAL has been awarded several nationally important projects in this area over the last decade. The projects span over a wide range of SMA research and development. Many of them have led to the successful building of SMA based devices for aerospace structural applications. I have been the principal investigator in these projects. These are listed below:

LIST OF PROJECTS

Sl.No.	ACTIVITY	SPONSOR
1	Development of Smart Control surface	AR & DB*
2	Development of Air Frame for RC blimp & development of smart landing gear	CSIR**
3	Deployment of Mousche using SMA	ADA ***
4	Development of SMA embedded composite beam	AR & DB
5	Development of smart SMA repair device	ADA
6	Development of smart material based adaptive wing concepts	CSIR
7	Investigation of thermo-mechanical characteristics of SMAs	General Motors

* Aeronautical Research & Development Board

** Council of Scientific & Industrial Research

***Aeronautical Development Agency

List Of Journal Publications / Patents/ Invited/ Conference Papers related to this work

A. Journal publications:

1. P. Sittner, D. Vokoun, G.N. Dayananda, and R. Stalmans, “Recovery Stress generation in shape memory Ti50i, Ni45, Cu5 thin wires,” Mater. Sci. Eng. A 286 (2000), Pg.298-311.
2. G.N. Dayananda and V. Shankar, “The Design of a NiTi based Shape Memory Alloy Actuator,” J. Aerospace Sci. Tech. 55 (2003), Pg.268-274.
3. G.N. Dayananda, B. Varughese and M. Subba Rao, “A Shape Memory Alloy based Smart Landing Gear for an Air Ship”, J. Aircraft, 44 (2007) Pg.1469-1477.
4. G.N. Dayananda and M. Subba Rao, “Effect of strain rate on properties of Superelastic NiTi thin wires,” Mater. Sci. Eng. A 486 (2008), Pg.96-103.

B. Patents:

1. “A Hingeless control surface” No: 194305 (Granted on 03.02.2006).

2. “A Novel Device using Shape Memory and Superelastic Alloys for Effecting and Controlling Swiveling Movement” No: 212059 (Granted on 11.03.2005).

C. Invited papers for Monograph:

1. G.N. Dayananda, R. Sundaram., G.M. Kamath and M. Subba Rao, “Smart Materials for Aerospace Applications” monograph published by UGC-Centre for Advanced Studies in Fluid Mechanics, Dept. Math., Bangalore University (2003), Pg.47-71.
2. G.M. Kamath and G.N. Dayananda, “Thermo-mechanical modeling of Shape Memory Alloys” for a monograph titled “Modeling of Nano and Smart Materials” published by UGC-Centre for Advanced Studies in Fluid Mechanics, Dept. of Math., Bangalore University (2003), Pg.113-120.

D. Papers Presented In Conferences/Seminars:

1. G.N. Dayananda and V. Shankar, M. Subba Rao and M.A. Farook, " Active Shape Control of an Airfoil using Shape Memory Alloys " Proceedings of Third International conference on "Advances in Composites" ADCOMP-2000,Bangalore, India (2000), Pg.392-399.

2. G.M. Kamath, G.N. Dayananda and R. Senthilpriya, "A Modified Thermo mechanical Modeling Approach for Shape Memory Alloy Behaviour", Proceedings of the SPIE-ISSS International Conference on Smart Materials, Structures and Systems, Bangalore, India (2002), Paper No.SM-236, Pg.874-881.

3. V. Shankar, G.N. Dayananda, P. Senthil Kumar, M. Subba Rao, R. Balasubramaniam, "Development of Electronic Actuation System for Shape Memory Alloy Based Aerospace Structures," Proceedings of the SPIE-ISSS International Conference on Smart Materials, Structures and Systems, Bangalore, India (2002), Paper No. SA-458, Pg. 860 – 867.

4. G.N. Dayananda, B. Varughese, T. Harish Kumar and M. Subba Rao, "Development of an SMA based smart landing gear for rotorcraft and other similar applications" Proceedings of Fourth International conference on Smart Materials, Structures and Systems, Bangalore, India (2005), Paper No. SB-06, Pg.SB-36 to 44.

5. G.N. Dayananda, P. Senthil Kumar and M. Subba Rao "Development of an SMA based actuator mechanisms for deployment of control surfaces" Proceedings of Fourth International conference on Smart Materials, Structures and Systems, Bangalore, India (2005), Paper No. SB-19, Pg.SB-131 to 138.

6. P. Sittner, P. Lukas, P. Sedlak, M. Landa and G.N. Dayananda "On the exploitation of unique properties of Ni-Ti associated with R-phase transformation

in smart structure applications" Proceedings of Fourth International conference on Smart Materials, Structures and Systems, Bangalore, India (2005), Paper No. SC-01, Pg.SC-1 to 8.

7. G.N. Dayananda, R.V. Krishnan, M. Subba Rao and M. Pattabi "Fatigue behavior of Ni-Ti shape memory alloy thin wires: Modeling and Experimental issues" Proceedings of the International conference on Frontiers in fluid mechanics (ICFFM-06) (2006), Pg.274-294.

8. G.N. Dayananda, "Shape Memory Alloys for Aerospace Applications" Proceedings of 21st National Convention of Metallurgical and Materials Engineers, Bangalore, India (2008), Pg.47-62.

9. B. Varughese, G.N. Dayananda and M. Subba Rao, " Modeling the Behavior of an Advanced Material Based Smart Landing Gear System for Aerospace Vehicles" American Institute of Physics proceedings of the International workshop on Smart Devices: *Modeling of Material Systems,* IIT, Chennai (2008),Pg 92-103.

Chapter 1: General Introduction

1.1. Background:

Amongst the several available materials, the commonly used materials for energy dissipation in landing gears and other related structural sub-systems in aerospace and other vehicles are carbon spring steels, polymeric composites, aluminum alloys, rubber, honeycomb core and some types of foams. Different types of energy dissipating/absorbing mechanisms (for use during landing) have been conceived and built using these materials. The proper dissipation of the impact energy during landing is necessary to ensure the 'soft' landing for these vehicles. The soft landing is required to protect the sensitive payloads in the vehicle. The Super Elastic (SE) Nickel Titanium (NiTi) Shape Memory Alloys (SMAs) are a new class of materials which are strong candidates for repeated use in energy dissipating devices (for instance in the smart landing gear systems) particularly when they are made to undergo 'large elastic' deformation in the tensile mode. The term "large elastic" strain in this thesis refers to the stress induced large super elastic strain which is completely recoverable (when the stress is removed). Also, the elastic recoil in these materials takes place at a relatively much lower value of stress (owing to the hysteresis), which ensures better structural stability of the vehicle during the recoil period after the landing impact. The NiTi SMAs can be joined to other metals, have good thermomechanical stability, possess superior structural properties and exhibit easier control of transformation temperatures through heat treatment compared to previously discovered shape memory alloy systems such as Cu-Zn-Al or Au-Cd systems. They offer the possibility of wide use in many structural, mechanical and other engineering applications

1.2. Polymeric Carbon Composites:

Polymer carbon composites which have high specific stiffness and high specific strength (and therefore weigh less) but low ductility are effectively integrated with SE SMAs (possessing large pseudo or super elastic strain) to realize the efficient smart landing gear. The landing gear/shock absorption system is one of the most important sub-systems of a vehicle.

The polymeric composites technology has now matured sufficiently for use in a variety of applications. Structural weight reduction is the key advantage in using these materials. In particular, advanced polymer carbon composites are now gaining increased acceptance in the aerospace industry. This is because of their high strength and stiffness characteristics compared with other traditional structural materials such as aluminum and steel. These composites have high performance reinforcements, which are of a very thin diameter (typically in the range of 0.005-0.010mm) in a matrix material such as epoxy. Examples of advanced polymer composites are graphite/epoxy, carbon/epoxy & Kevlar/epoxy. These materials have now found applications in commercial industries as well.

A representation of the strength and stiffness of many materials including carbon is given in [2]. When placed in unidirectional orientation the strength of carbon fiber is more than that of most other materials. Even in the biaxial isotropic configurations, the stiffness of carbon-epoxy composite is comparable to that of steel. The smart landing gear is predominantly made of carbon composites. In some zones where the SE SMA is connected to the landing gear glass composites have been used. This is because of the simultaneous use of the SE SMA as a sensor apart from its primary role as an energy dissipating element. The exploitation of the sensory characteristic requires a small amount of constant current to be flowing in the SE SMA element. Since carbon composites are electrical conductors, glass composites are used only in those places where the SE SMA joins the structure. The mechanical behavior of carbon and polymeric composites has been extensively studied. References [3] – [6] report on the static and dynamic mechanical behaviour of polymeric composites. References [7] & [8] investigate the damage mechanisms in polymeric composites and [9] deals with the effect of temperature on the inter phase. The evaluation of tensile properties of natural bamboo fibers in a polymeric matrix is covered in [10]. In this work some limited quasi static test results relating to the mechanical behavior of carbon and glass composites is presented.

1.3. Principles of shape memory:

Like other shape memory materials, NiTi SMAs have the unique ability to recover their original shape after undergoing large deformations at a given temperature either through heating (referred to as the shape memory effect) or by the removal of the external load (referred to as the super-elastic effect). Fig. 1.1 illustrates the summary of the mechanical behavior as a function of strain, stress and temperature. The shape memory properties are the manifestations of a reversible martensitic phase

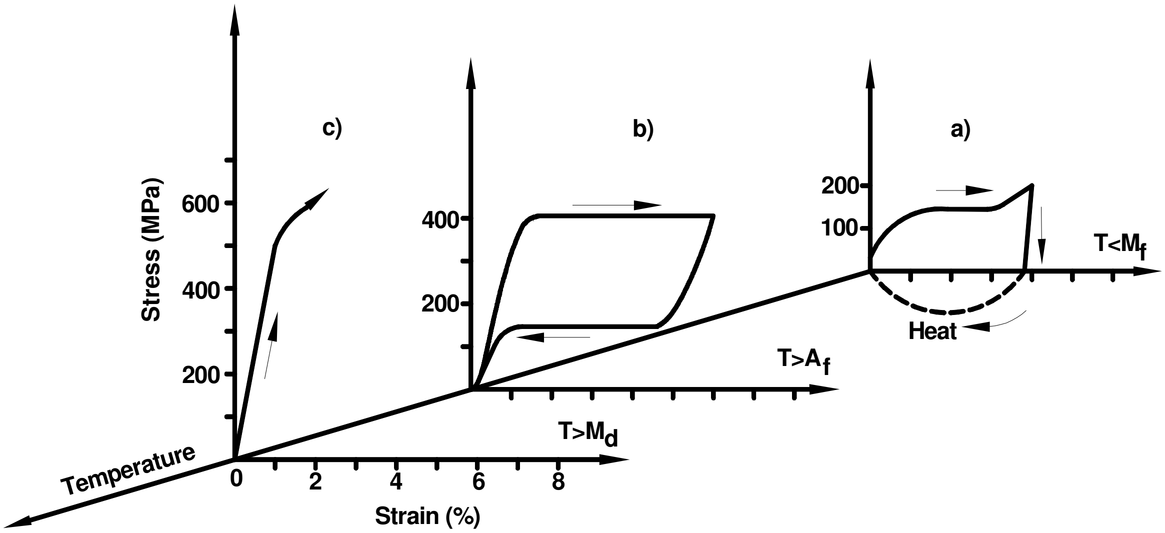

Fig.1.1: Schematic representation of stress-strain-temperature showing: (a) shape memory, (b) superelasticity; and (c) ordinary plastic deformation.

transformation occurring in the system between a crystallographically high-symmetry (cubic crystal structure) austenite phase to low symmetry (monoclinic crystal structure) martensite phase. The SMA exhibits the shape memory effect when deformed below the martensite finish temperature, $M_{f.}$ These deformations (below M_f) are recovered by heating the material above the austenite finish temperature, $A_{f.}$ The SMA is in its parent austenite phase above A_f. Stress-induced martensite (SIM) is formed when the austenite is stressed to a certain level (above A_f). On removal of load, the stress induced martensite reverts to austenite at a lower stress, thereby resulting in the super elastic behavior. The resulting non-linear stress-strain relationship results in a hysteresis. As the test temperature is increased, the stress at which the SIM forms also increases. Beyond a temperature designated as $M_{d,}$ true plastic deformation occurs in place of SIM formation. It is important to point out that the same material, which exhibits the thermal shape memory effect in one temperature regime; also exhibits the SIM based pseudo elasticity in another temperature regime.

Therefore, it is clear that the martensitic transformation is driven by the change of an external field; temperature or stress. Both the thermal and stress driven martensitic transformations have several engineering applications and are dealt with in [11]. References [12], [13] present a review of the thermoelasticity, pseudoelasticity and the memory effects associated with martensitic transformations. The impact damage behaviour of shape memory alloy composites has been covered in [14]. The use of thermal SMA is centered on the generation of recovery force and strain, while the use of super elastic SMA is centered on the energy dissipation capability. The thermal SMA is used as a work producing device, whereas the superelastic SMA is used in energy storage/dissipation/damping applications. The dissipation of energy in these materials is due to the stress hysteresis as already mentioned and is typically of the order of 150 to 300 MPa. The NiTi SMA has very high specific energy storage capacity in the elastic region compared to both helical steel spring and aluminum flat specimen. This is shown in Table 1.1

Table 1.1: Specific energy stored in elastic region based on 100 mm sample lengths

SPECIMEN	Length (mm)	Mass (N)	Energy stored in elastic region (J)	Specific energy stored in elastic region (J/N)
NiTi SMA	100	0.00182	1.7	934
Steel helical spring	100	0.4	2	5
Aluminum strip	100	0.03	4	133

Fig.1.4 shows the comparison of the NiTi super elastic SMA behavior with that of a helical tensile spring (wire dia=2.5 mm, coil dia=12 mm and length=100mm) whose overall stiffness is comparable with that of a NiTi super elastic SMA wire.

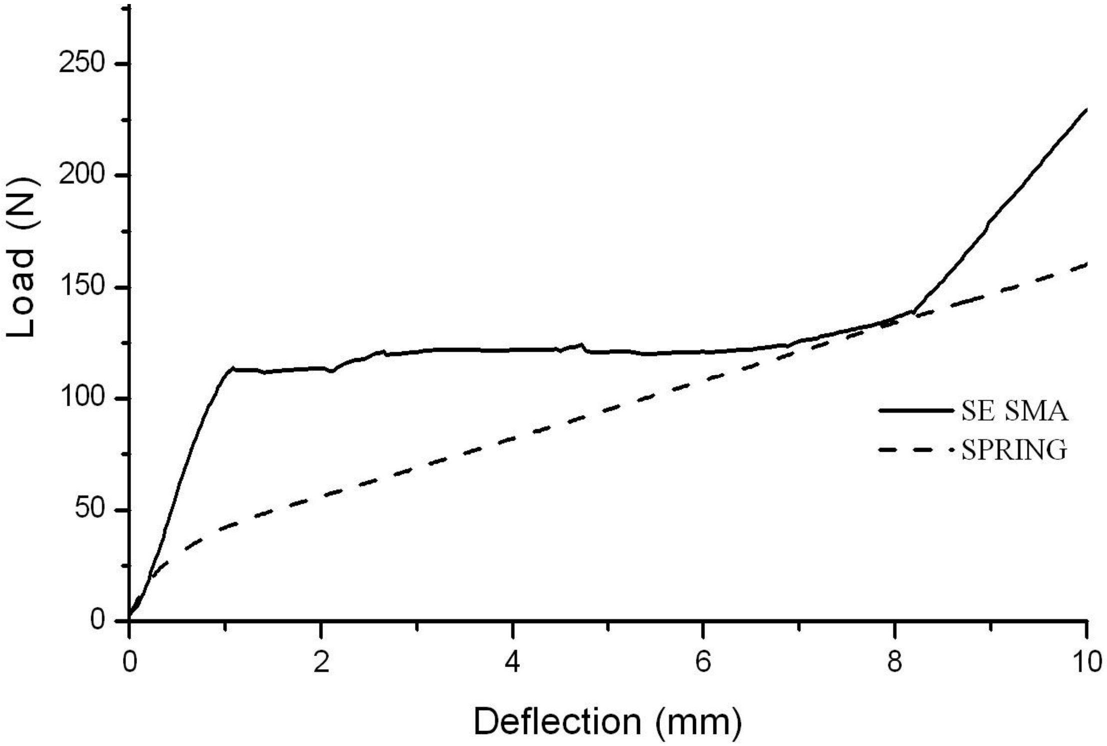

Fig.1.2: Comparison of NiTi SE SMA with a helical spring of comparable stiffness.

It is clear that the NiTi SMA has a far higher energy storage characteristic up to about 6% strain. Extending the comparison up to say, 10% strain (i.e., deformation up to 10 mm for 100 mm length of spring) the NiTi SMA stiffness (deflection for a unit load) increases with increasing deformation beyond the 6%. This stiffness increase enhances the stiffness of the device in which it is used similar to the steel springs. The stiffness of NiTi SMA varies as a function of the strain rate and is discussed in more detail in subsequent chapters.

Before going into the details of the study on superelastic SMAs a brief account of the principles and modes of usage of the thermal SMA in engineering applications is discussed.

1.4. Thermal SMA and applications:

Once the thermal SMA is deformed in the martensite condition, if it is completely constrained (without allowing strain recovery) and heated, then, it generates a recovery force, which is also referred to as the block force. As illustrated in Fig.1.3 the block force is maximum when the pseudo elastic recovery strain is zero (A). At the other extreme when complete pseudo elastic recovery is allowed (typically 4-6% in NiTi alloys) the block force is zero (B).

Many researchers have attempted to embed thermal SMAs (in the pre strained condition) in polymeric composites.

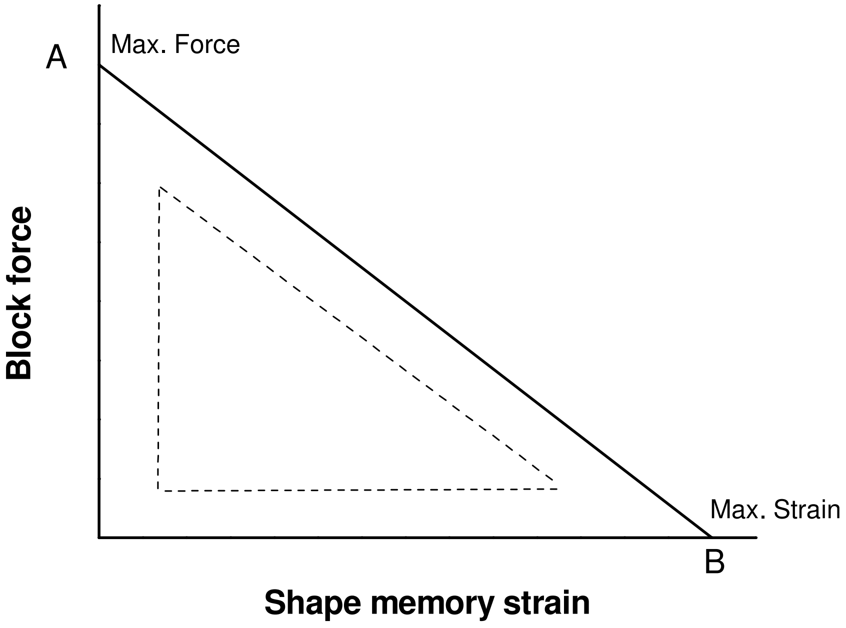

Fig.1.3: The design envelope for a thermal SMA actuator

The modeling and material design aspects are covered in [15]. The generation of the block force (or recovery stress) in the completely constrained condition is due to heating and follows the familiar Clausius Clapeyron equation represented by $d\sigma/dT \approx$ 6-8 MPa/ °C for NiTi base alloys [16]. The generation of recovery stress starts at the onset of A_s and peaks around the A_f temperature. The recovery stress varies with pre-strain in the SMA element and reaches a maximum around an initial pre-strain of 3% in NiTi alloys.

Fig.1.3. shows the design envelope for a thermal SMA actuator that will be within the representative dotted triangle in most engineering applications. Despite the fact that the efficiencies of thermal SMA actuators are very low compared to other actuators their research is still being actively pursued. This is because of the several other advantages that the SMA actuation provides. Notable among them are silent and clean operation environments and minimum number of moving parts. Invariably the SMA has to work against a bias force. The different methods of biasing the thermal SMA are:

a) From the host structure itself [17] (Ref. Fig.1.4)

b) From another thermal SMA (antagonistic method of actuation) [18, 19] (Refer Fig.1.5 (a), (b) and (c)).

c) From a conventional spring (tension or compression) [20] (Ref. Fig.1.6).

d) From a super elastic SMA [21].

e) Using a constant weight [22].

.

Fig.1.4 shows the example of the host structure (SMA embedded FRP beam) being used as a bias. The SMA is embedded away from the neutral axis which induces an initial bending pre-strain in the structure. This enables the host structure to act as a bias and obviates the need for a conventional spring.

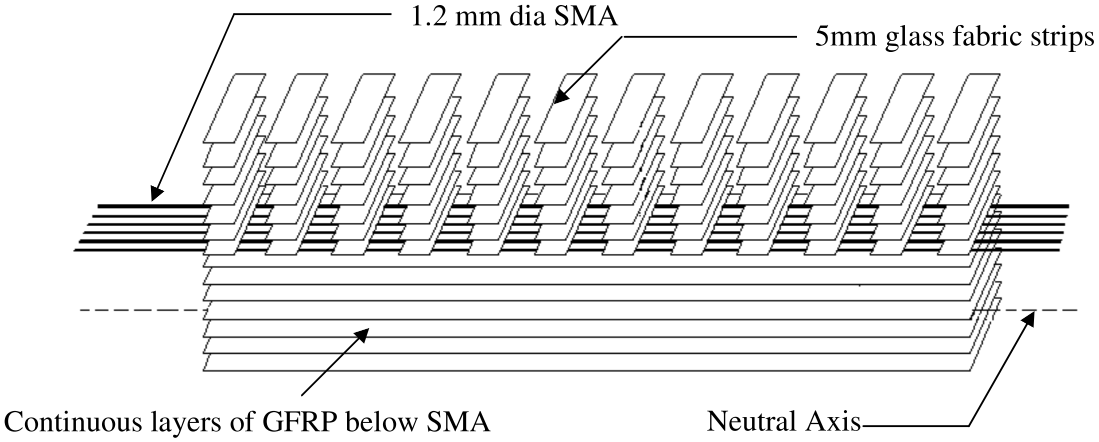

Fig.1.4: Biasing from the host structure (typical FRP beam).

The antagonistic method of actuation is a novel method of energizing the SMA and was successfully employed in the development of a smart control surface model of a typical military aircraft with SMA elements on either side of the neutral axis. Figs.1.5 (a) & (b) show the orthographic views. The smart control surface was subjected to simulated aerodynamic loading and this work is detailed in reference [18].

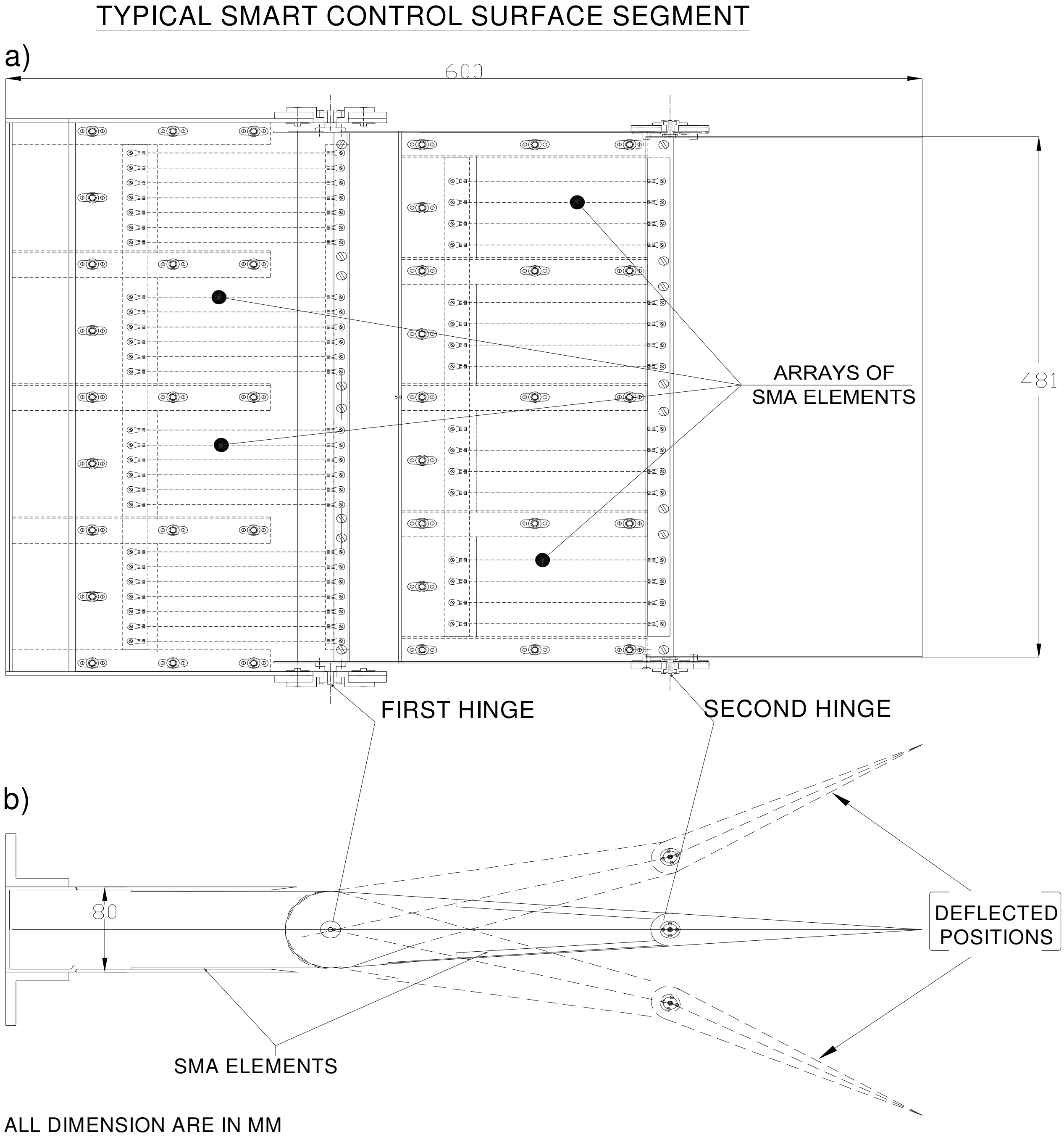

Fig.1.5 (a) & (b): Antagonistic method of SMA actuation for rudder model of a typical military aircraft.

Later it was also tested in the wind tunnel. The speed in the wind tunnel was varied from 60 to 160 km/hr. The SMA elements were observed to be very steady when subject to the wind loads. Fig.1.5(c) shows the photograph of the smart control surface model. The antagonistic method of actuation is done about both the hinge axis 1 and 2. There are 4 SMA arrays in total about the 2 hinge axis. The swiveling movement can be obtained about each of the hinge axis.

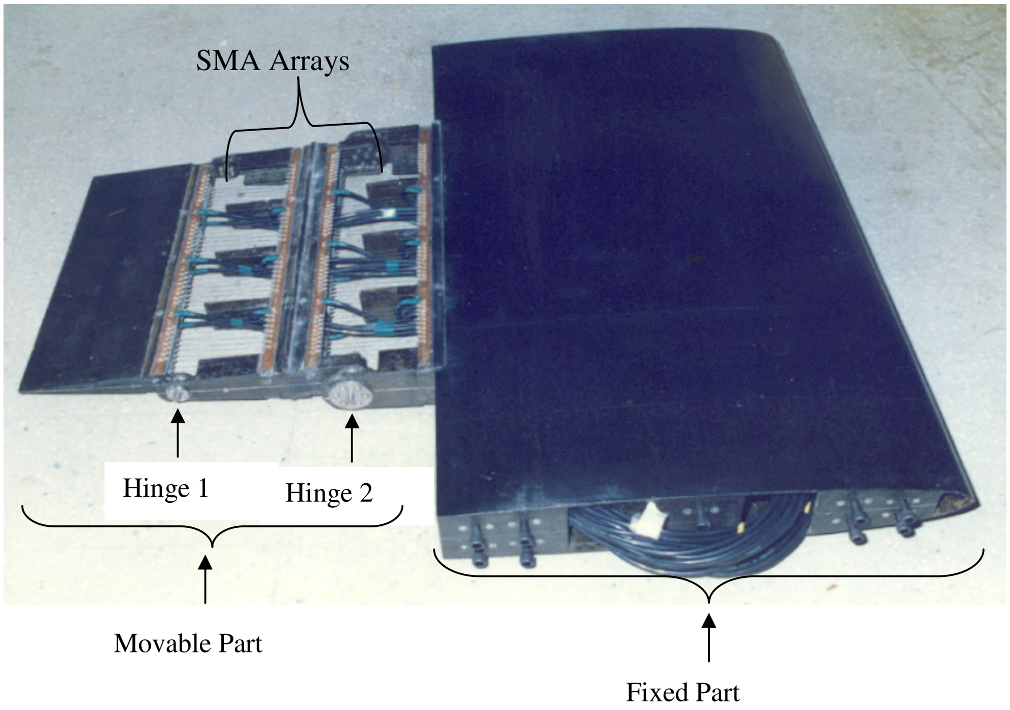

Fig.1.5(c): Photograph of SMA actuated rudder model of a typical military aircraft

Fig.1.6 (a) shows the additional aerodynamic control surface (mousche) which is deployed only during landing and retracted at all other times. The actuation for deployment is done using SMA banks. The retraction is done using a bias spring.

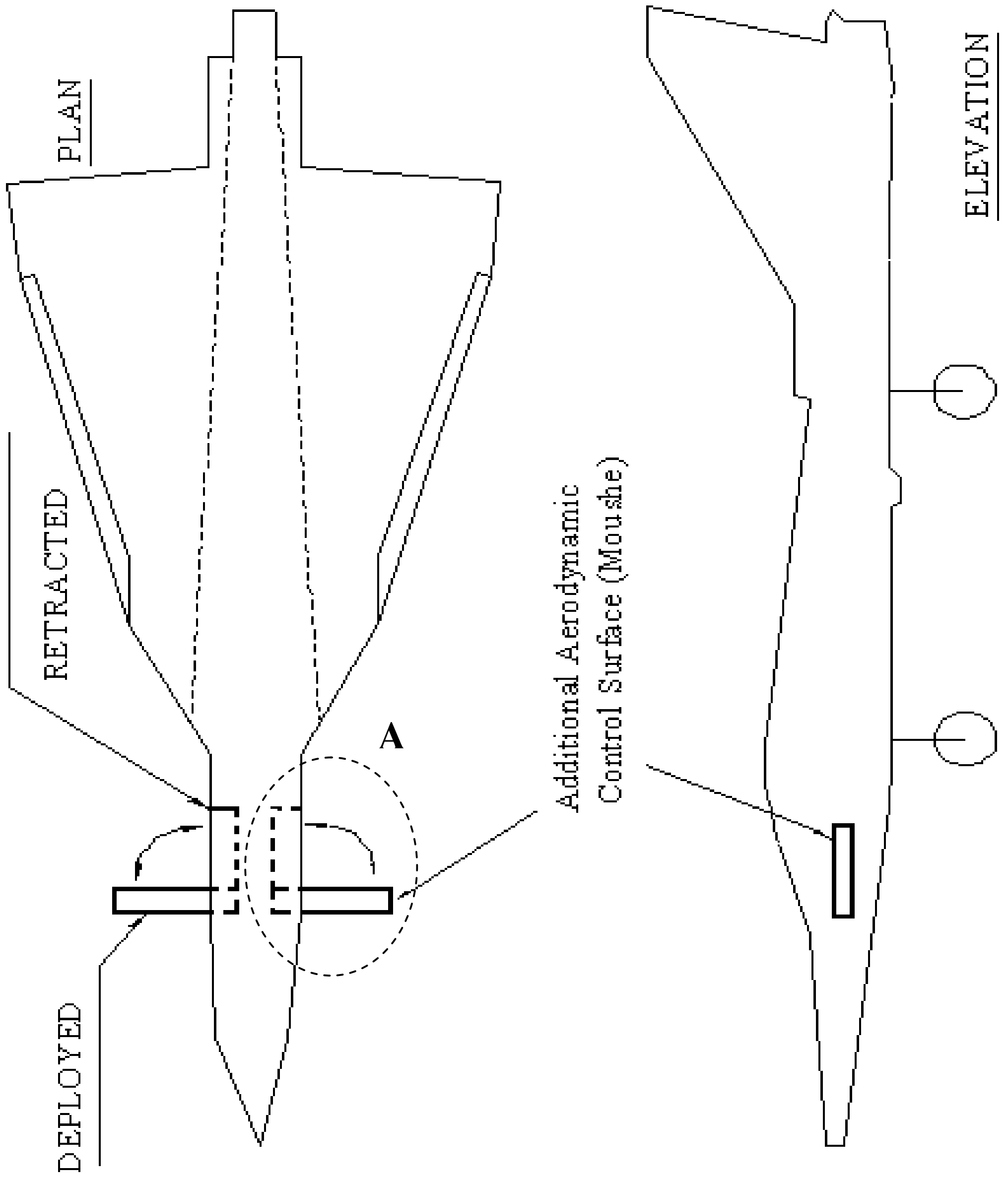

Fig.1.6 (a): SMA actuated mechanism for deployment of the additional aerodynamic control surface for a typical military aircraft.

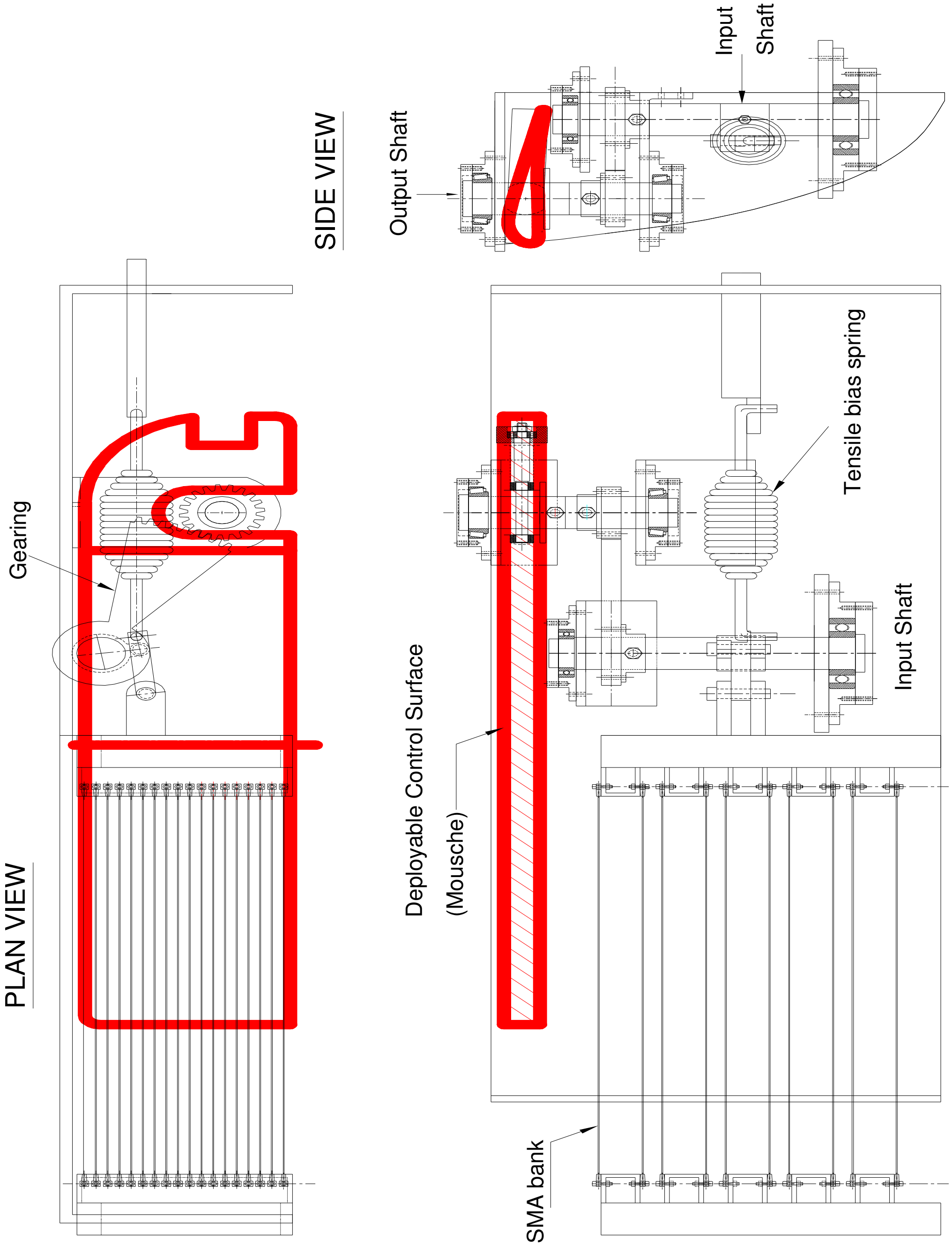

Fig.1.6 (b): Model of SMA based mechanism for deploying an aircraft control surface (Detail ‘A’ in Fig. 1.8 (a) enlarged).

Fig 1.6 (b) is the detail of ‘A’ shown in the dotted circle in Fig. 1.6 (a).This shows the use of a conventional tensile spring as a bias element that has been effectively demonstrated in the development of an SMA based actuator mechanism for deployment of control surfaces [20] for typical military aircraft applications. Whether the SMA is used in the antagonistic configuration or completely constrained or with a bias spring it needs to be trained before use. The training is done to obtain stable and consistent behavior.

The electrical heating is usually the preferred mode of heating the SMA. When the SMA is electrically energized it transforms due to the resistance heating from martensite to austenite as it undergoes the contraction and in the process, does mechanical work. The electrical input based on the resistive heating = i^2Rt ------ (1.1) where ‘i’ is the current, ‘R’ is the resistance and‘t’ is the time. The efficiency of the SMA actuator is evaluated as the ratio of the mechanical work output to the electrical input. Both the time of heating and the magnitude of the current affect the SMA actuator performance. The inter-relationships between the mechanical properties and the related electrical properties (when the SMA element is under a constant stress) as well the current-time equivalence for the joule heating have been studied [22]. The fundamental characteristics of SMA and a complete design model for a linear SMA actuator based on the thermal, mechanical and continuum mechanical aspects have been brought out by Mihalcz [23].

1.5. Heat treatment of SE SMAs:

The mechanical properties including the energy dissipation capability of the SE SMA is dependent on the heat treatment procedures. It is necessary to arrive at the optimum heat treatment which will impart the maximum energy dissipation capability. At the same time one has to ensure that the material has the required level of the plateau stress and the stiffening effect (the elastic behavior beyond the SIM plateau) desirable for the landing gear device. The details of the heat treatment that has been carried in order to realize the desired properties are presented in chapter 3. Duerig et al [24] reports that the combination of cold work in the martensite together with subsequent anneals is a standard procedure adopted to improve the SMA characteristics. Otsuka et al [25] observed that the most widely used treatment for both the thermal and super elastic SMA is the so called ‘medium temperature treatment’ in which the heat treatment temperatures are in the range of 623-723 °K and the holding times range from 10-100 min. Yeung et al [26] observed that the austenitic transition temperature of the NiTi alloy can be adjusted to the required value by altering the time and temperature of heat treatment for a SE SMA NiTi alloys for medical use. Their results showed that the heat treatment temperature should be set between 400-500 °C and the heat treatment time should be less than 60 min. Faviera et al [27] observed that the aging of NiTi SMAs at 773 °K for short times of the order of few minutes led to an increase of the critical temperatures for both R-phase to martensite and austenite to martensite transformations. It also led to a decrease of critical stress for inducing martensitic transformation at a given temperature. Yan et al [28] studied the influence of heat treatment on the fatigue life of a laser-welded NiTi alloy wire. They arrived at the optimum anneal for best fatigue resistance. Zinelis et al [29] investigated the effect of thermal treatment on the resistance of nickel-titanium rotary files in cyclic fatigue and also inferred that the appropriate HT can significantly increase the fatigue resistance. Frenzel et al [30] reported on the microstructure and phase transformation response to different thermomechanical treatments for Ni-Ti-Fe SMAs. Liua et al [31] studied the structure and damping properties of NiTi SMAs using different heat treatments. The result shows that the structure of the alloy with slow cooling contains large amount of M and R- phases and the Ni richer Ti_3Ni_4, so that the damping level of the alloy is higher.

In this work the heat treatments have been done to obtain the optimum energy dissipation properties.

1.6. Sensory behavior of SE SMAs:

The smart materials are normally associated with more than one function. Here in this work, the Ni Ti SMA is proposed to be used simultaneously both as a strain sensor and as an energy dissipating device. In this situation it is necessary to examine the sensory characteristics of SE SMA.

The principle of the sensory function lies in electrically energizing the SE SMA by a small constant current. The change in strain of the SE SMA element is manifest as a change in output voltage. While undergoing straining during the energy dissipation process the material is transforming from the parent austenite phase to the martensite phase and back. These changes in phase while the material undergoes the length change cause substantial changes in the output voltages. The changes in voltage output can be computed as a resistivity change, which is in turn interpreted as a change of length. In this way the SE SMA material is used as a strain sensor. In the literature the strain sensing property of SE SMA has been investigated.

Hui et al [32] investigated the strain self-sensing property and the strain rate dependence of SE SMA and concluded that the electric resistance of the SE SMA varies linearly with the applied strain. They also observed that the pseudo elastic behavior is influenced by both ambient temperature and loading frequency. Novak et al [33] investigated the evolution of electrical resistivity during thermal and mechanical tests of NiTi wires and inferred that the electrical resistivity of all investigated phases (austenite, R-phase and martensite) increases linearly with increase in temperature though the slopes are quite different. Antonucci, et al [34] conducted electrical resistivity study and characterization during NiTi phase transformations and demonstrated that the resistivity method is a very useful technique for the identification of transition phases that are not detectable from calorimetric analysis. Pozzi et al [35] studied the electrical transport properties of TiNiCu SMA ribbons and inferred that they have promising sensing/actuating characteristics. Uchil et al [36] conducted electrical resistivity and strain recovery studies on the effect of thermal cycling under constant stress on R-Phase in NiTi SMAs. Sittner et al [16] investigated the recovery stresses generated by TiNiCu thin SMA wires with simultaneous measurement of electrical resistance. Airoldi et al [37] and Jin et al [38] studied the electric resistance of NiTi SMAs in the pseudo elastic region. They inferred that the electric resistance variation shows a linear behavior reversible with the transformation direction. The measurement of electrical parameters along with energy dissipation characteristics is focused in this work.

1.7. Super elastic SMA and Other Energy Dissipating Materials:

The use of super elastic SMA in energy dissipating applications is based on the principle wherein the SMA element undergoes a stress induced large pseudo elastic strain. This pseudo elastic or super elastic strain is completely recoverable when the load (stress) is removed. Like the thermal hysteresis in the thermal SMA, there is also a stress hysteresis associated with the stress induced SMA. Due to stress hysteresis the superelastic SMA can dissipate large amounts of energy compared to other conventional materials.

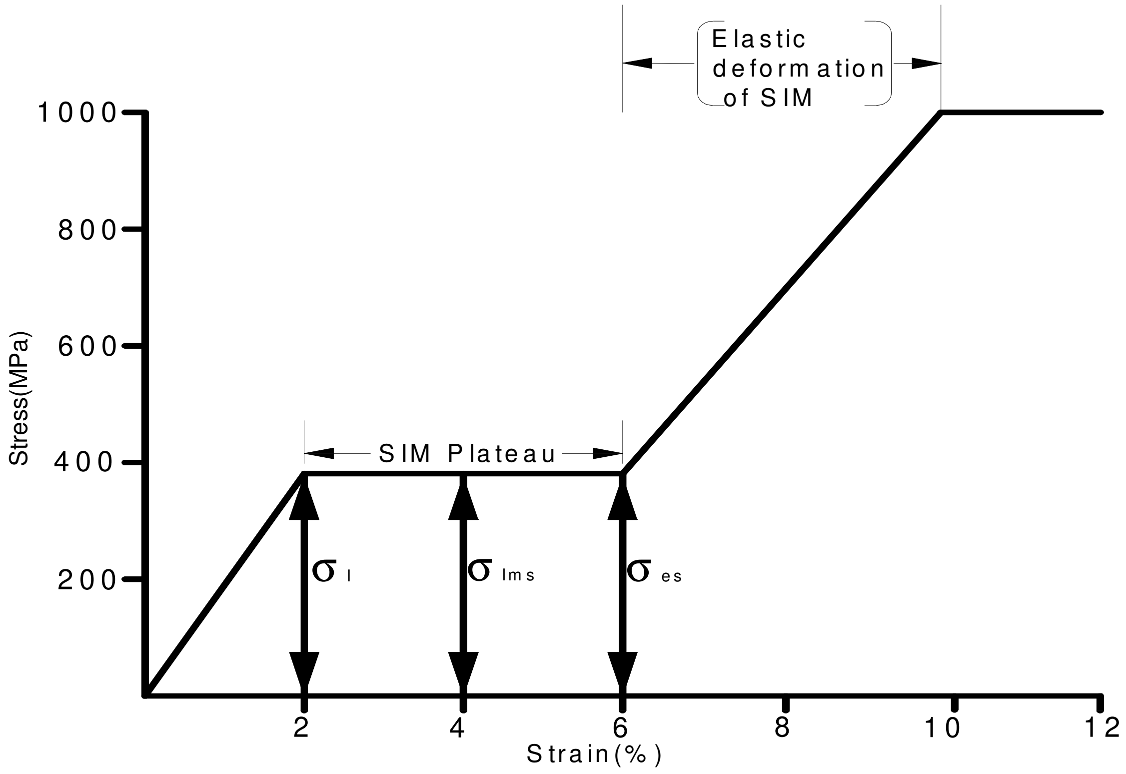

Fig.1.7: Idealized stress-strain behavior of SE SMA during tensile test.

Fig.1.7 shows the idealized stress-strain diagram indicating the plateau stresses and the stresses in the elastically deformed SIM segment that are studied to analyze the behavior of these materials.

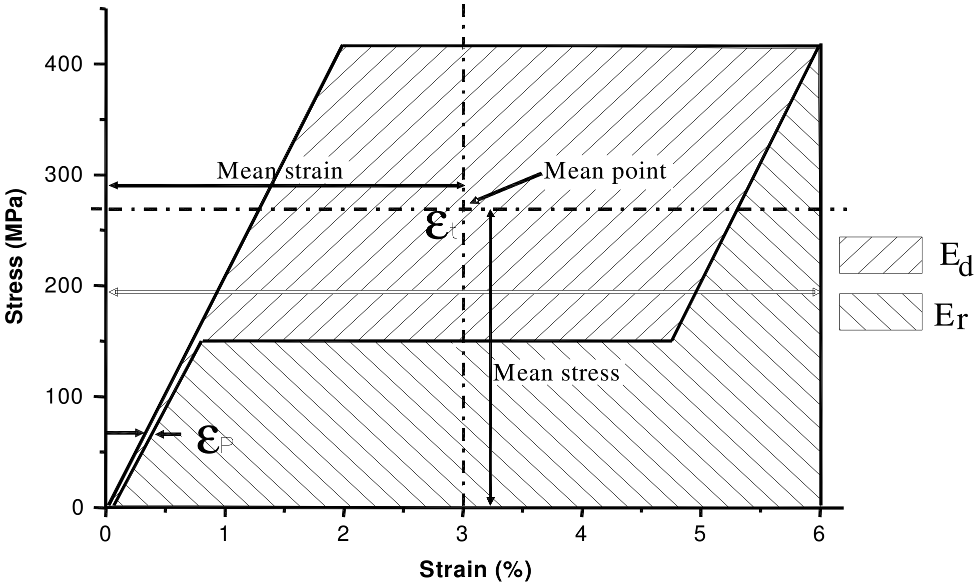

Fig.1.8: Representation of energy dissipated 'E_d' and recoverable strain energy 'E_r'.

In Fig.1.8 the area enclosed by loading curve and unloading curve represents the dissipated strain energy (E_d) and the area below the unloading curve represents the recoverable strain energy (E_r) respectively. Among the several energy dissipating materials, the commonly used materials for aerospace structural applications are carbon spring steels, rubber, honeycomb core and some types of foams. Different types of energy absorbing/dissipating mechanisms have been conceived and built using these materials. As already stated, the super elastic SMAs are a new class of materials which are strong candidates for repeated use as energy absorbing devices, particularly when they are made to undergo 'large elastic' deformation in tensile mode.

The Figs.1.9(a) – 1.9(d) bring out the superior energy absorbing/dissipating capabilities of the NiTi SE SMA material that has been used in this development in relation to the other conventional materials such as carbon spring steel, structural steel and aluminum alloy. The elastic strain limit in the carbon steels, other structural steels and aluminum is about 2 %. The comparable elastic strain limit in the SE SMA is as high as 12 %. As shown in Table 1.2 due to the high super elastic strain capability the Ni Ti SE SMA can store/absorb a far higher amount of energy compared to the conventional metals referred above.

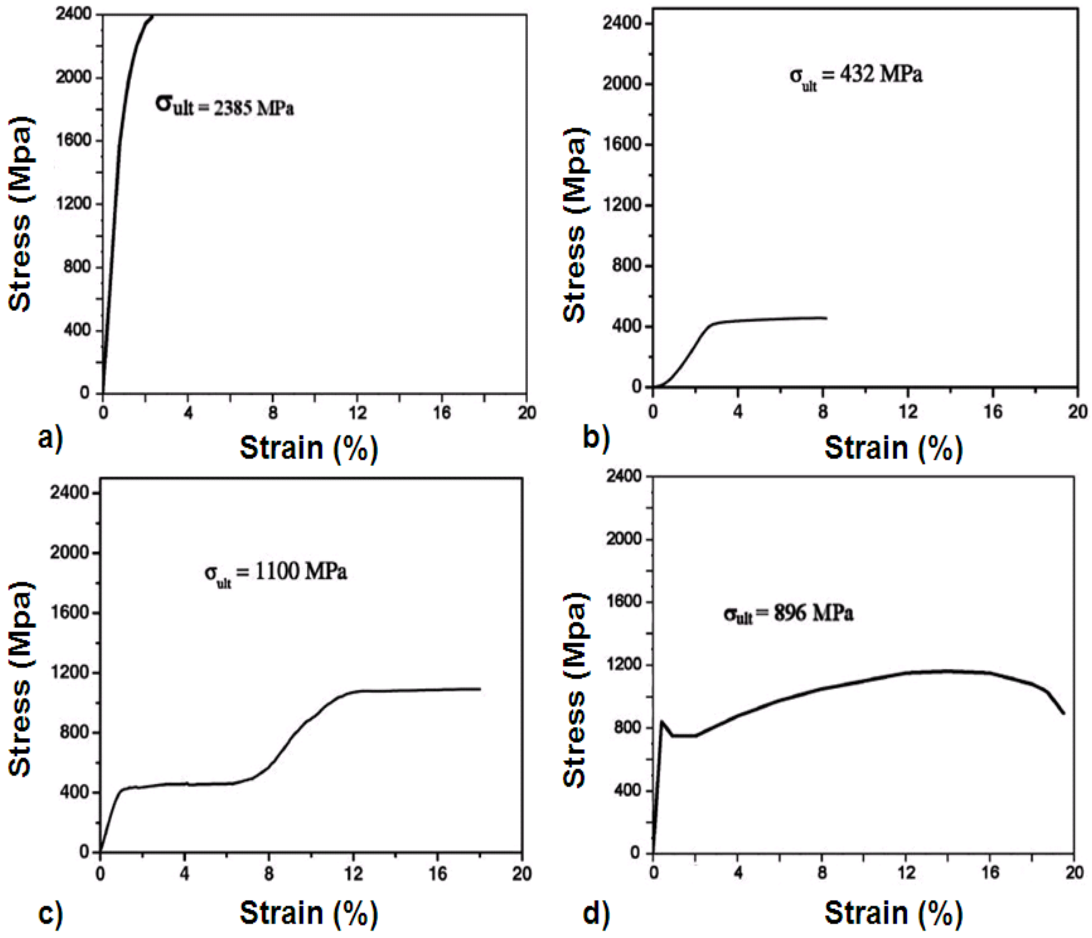

Fig.1.9: Stress–strain curve for: (a) high carbon spring steel wire; (b) aluminum wire; (c) super elastic SMA; and (d) structural steel wire.

Likewise the SE SMA can dissipate large amounts of energy within the pseudo elastic regime compared to other materials. Also as is evident from Figs. 1.1, 1.2, 1.8 and 1.9 the super elastic material is not only far superior in terms of the energy absorption but also has a lower level of recoil stress (i.e. stress during recovery) due to the stress hysteresis which imparts better stability characteristics to the aerospace vehicle.

Table.1.2: Comparison of energy absorption of four different materials.

Material	Energy absorption in elastic region (J/cc)	Elastic recoil stress (MPa)
High carbon Spring Steel	6.42	1590
High strength Structural Steel	1.8	800
Super elastic NiTi SMA	60	100
Aluminum	4.1	414

The high-energy dissipation capability of SE SMA makes it an ideal candidate for use in the development of an efficient carbon composite based landing gear for a certain class of aerospace vehicles.

The energy dissipation capability has to be retained over a wide range of strain rates in many devices that the NiTi SMA is likely to be proposed for use. Therefore the study of energy dissipation and related properties over a wide range of strain rates has been undertaken. It is pertinent here to assess the current research in the area of the study of the effect of strain rate on energy dissipation and related properties of NiTi SE alloys.

Kafka et al [39] developed a model with tensorial internal variables to depict the linear relation between temperature and threshold stress level necessary for SIM. Des Roches et al [40] investigated the strain rate effects by subjecting the NiTi SMA wires and bars to loading frequencies of 0.025, 0.5 and 1.0 Hz at superelastic strain amplitude of 6%. Their results showed that as the test frequency increases the loading and unloading plateau stresses increase whereas the hysteresis and the hysteretic damping markedly decrease. Dolce et al [41] studied the effect of loading frequency on the behavior of NiTi SMA wires in the austenite condition. They inferred that the mechanical behavior is affected when passing from very low frequency (less than or equal to 0.01Hz) to the frequency range of 0.2 to 4 Hz. They recorded that when the strain rate is increased the hysteresis loops narrow and translate upwards, while the segments of the curve relevant to the phase transformation harden, thus yielding an increase in the stress levels. The strain amplitude considered was again 6%. Brinson et al [42] conducted in-situ optical microscopy observations of NiTi SMA tensile behavior. During the loading sequences containing constant displacement holds they observed stress relaxation. The magnitude of the stress relaxation decreased with decreasing strain rates. The stress relaxation was attributed to the latent heat released in the specimen during the transformation. Nasser et al [43] found that that the super elastic behaviour of these materials have stronger sensitivity to temperature than to strain rate. Humbeeck et al [44] inferred that for Cu-Zn-Al crystal the change in hysteresis as a function of strain rate can be attributed to heating and cooling of the sample due to exothermic character of the beta-martensite transformation and the reverse endothermic transformation. The observations of Raghavendra et al [45] illustrate a complex interplay of test temperature, stress state and martensite type that lead to asymmetry in compression vs tension response of NiTi SMA in quasi- static and dynamic loading conditions. Aaltio et al [46] investigated the temperature dependence of the damping properties of Ni-Mn-Ga alloys and inferred that enhanced damping in the martensite phase can be attributed to the mobility of twin boundaries. Ahluwalia et al [47] studied the influence of microstructure on the dynamic strain loading of cubic to tetragonal martensites. Lin et al [48] studied the influence of strain rate on deformation property of NiTi SMAs. They concluded that the martensitic transformation stress and recoverable strain energy density is dependent on the strain rate in a certain range. In a similar work Tobushi et al [49] inferred that for the case of strain rate higher than 10% per min the martensitic transformation stress and dissipated work increase with increase in strain rate. But the reverse transformation stress and strain energy decreased. They also observed that for the case of strain rate lower than 2% per min the characteristic values associated with the martensitic transformation did not depend on strain rate.

There is certainly a strong interdependence of the ductility, temperature and strain rate that affect the tensile and energy absorbing (cyclic properties) behavior of NiTi SMAs. The interplay of the ductile behavior, temperature, energy storage and strain rate effects and cycling needs a much better understanding.

1.8. Modeling Fatigue Behaviour:

NiTi SE SMA used as energy dissipating devices is subjected to stress-strain cycling and therefore, it is important to consider the fatigue life of such actuators. But such studies on NiTi thin wires are rendered difficult by the fact that it is not possible to introduce a fatigue crack and monitor its growth as is done in the case of a conventional rectangular cross-section metal specimen. It is further complicated by the need to have accurate non-contact displacement measurements and other in-situ measurements, which can in turn be used in the calculations to theoretically predict the fatigue behavior.

Not much literature is available that comprehensively covers the prediction/modeling of the fatigue behavior and in-situ measurement of parameters indicating the degradation/ fatigue of the material during cycling for NiTi based thin wires. This study covers some of the issues related to the modeling and experimental aspects involved in predicting the fatigue life of the NiTi SMA thin wire actuators subjected to stress-strain cycling. Melton et al [50] used the Coffin-Manson Law [51] to study the fatigue crack in rectangular cross section NiTi specimens subjected to stress-strain cycling (tension-compression loading) and found that this law was obeyed in low cycle fatigue regime.

Young et al [52] also used the Coffin-Manson relationship for predicting *In Vivo* failure of pseudoelastic NiTi devices under low cycle, high amplitude (range of 2.5 to 18.2%) fatigue. Matsui et al [53] investigated the tensile deformation and rotating-bending fatigue properties of a high elastic thin wire, a superelastic thin wire, and a superelastic thin tube of NiTi alloy. Aroujo et al [54] studied the fatigue behavior of NiTi thin wires subjected to thermo mechanical cycling and arrived at an empirical relationship based on the Wohler (stress vs. number of cycles) curves for predicting the fatigue life.

Holtz et al [55] have arrived at the fatigue thresholds of NiTi alloy near the shape memory transition temperature. Tabanli [56] et al showed that at fixed strain amplitude for NiTi, the cycle to failure values change in a non-monotonic manner with increase in mean strain. Lahoz et al [57] have reported on the influence of thermal parameters on the training and two-way shape memory in NiTi alloys. Young Liu et al [58] have shown from microstructure studies that a high density of dislocations are generated in the martensite twins, during the tension compression cycling of NiTi shape memory alloys. Yawny et al [59] studied the pseudo elastic cycling and ageing effects at ambient temperature in nanocrystalline Ni-rich NiTi wire and showed that hold times show significant effects. Yan et al [60] reported on the theoretical modeling of effects of plasticity on reverse transformation in superelastic SMAs. The constitutive model was employed to numerically study the transformation field and plastic deformation near a crack tip. Sulpice et al [61] discusses the ratcheting in relation to the super-elastic behavior of shape memory alloys under proportional cyclic loadings. Wang et al [62] investigated the phase transformation behaviour of pseudo elastic NiTi shape memory alloys under large strain and inferred that a small amount of plastic strain at the first loading cycle is helpful to get good stable mechanical properties. Zhang et al [63] showed that the fatigue of NiTi porous SE SMA occurs at a relatively lower strain level compared to the dense one. Roy et al [64] studied the influence of cold work on fatigue behavior of NiTi SMA wires using a dynamic mechanical analyzer. They inferred that the high concentration of austenite-martensite interfaces act as potential sites for stress concentration and are the main source of the drastic decrease of the fatigue life in the two-phase region. Nayan et al [65] evaluated the constant stress amplitude fatigue life of an austenitic Ni (55.88 wt. %)–Ti shape memory alloy (SMA) within the stress amplitude range of 180–450MPa. The stress–strain hysteresis loops were monitored throughout the fatigue loading. They reported that with the increasing number of fatigue cycles, the critical stress required for the stress-induced martensitic transformation, width of the hysteresis loop, recoverable and frictional energies of each cycle all decrease while accumulated plastic strain increases.

Siredey et al [66] conducted studies on the lifetime of superelastic Cu-Al-Be single crystal wires under bending fatigue and inferred that in surface striations, micro cracks were observed which are assumed to cause failure. Eggeler et al [67] investigated the structural and functional fatigue of NiTi SMAs.

The basic method of presenting engineering fatigue data for metals is by means of the S-N_f curve, where 'S' represents the stress and 'N_f' represents the number of cycles to failure. The usual procedure for determining the S-N_f curve is to test the first specimen at a high stress where failure is expected in a fairly short number of cycles and then the test stress is gradually decreased for each succeeding specimens until one or two specimens do not fail in the specified number of cycles. The highest stress at which a run out (non-failure) is obtained is taken as the fatigue limit. The fatigue experiments can either be stress controlled or strain controlled. The strain controlled low cycle fatigue (at relatively high stress levels and large strain levels) stress-strain cycling (A to M to A) for NiTi thin wires at constant temperature is part of this study.

In the tension-tension cycling of NiTi thin wires involving very large strains the evolution of plastic strain parameter is important. The Coffin-Manson relationship of the form [50]

$$N_f^{\beta}\Delta\varepsilon_p = K \text{ -------------------} \quad (1.2)$$

where 'N_f' is the number of cycles to failure, '$\Delta\varepsilon_p$' is the plastic strain between consecutive cycles, β is the slope of the plastic strain versus number of cycles curve & K the intercept of this curve with the Y-axis is used to study the fatigue life.

After examining the strain rate and fatigue related effects the design, fabrication, analysis and testing of a SE SMA incorporated carbon composite based smart landing gear system is presented.

1.9. Design & Development of Smart Landing Gear:

Energy absorption and crash worthy features are the primary design criteria that govern the development of landing gears. Del Monte [68] deals with the design and development of a crash worthy landing gear for rotorcraft that dissipates crash landing energy. Airoldi et al [69] deals with the design of the crashworthy landing gear adopting a crash tube as an energy-absorbing device in crash conditions. In this design a light alloy thin walled tube is mounted coaxially to the shock absorber cylinder and during the severe impact condition, this collapses in order to enhance the energy absorption performance of the landing system. Like the landing gear of fixed wing aircraft, the landing gear of helicopters has also evolved over the past few decades. The different variants of helicopter landing gear include the wheeled gear, tricycle, quadricycle arrangements and the skid type landing gear. Amongst these, the skid type of landing gear for the helicopter has gone through extensive design and development and is now used in many helicopters as it meets their requirement. Philips et al [70] deals with the design of a crashworthy landing gear for helicopters which would lessen the magnitude of crash forces. In this design the skid stiffness was idealized as a bilinear curve. The first part of the curve represents the elastic deformation and second part plastic deformation of the skid. Tho et al [71] refers to the design and development of high energy absorbing skid landing gear for helicopters. Stephens et al [72] deal with the development of a dynamic analytical methodology for analyzing the structural behavior of a helicopter skid gear during a high-energy landing. This methodology was used in the correlation of impact loads for level landing at different conditions. Airoldi et al [73] presents a numerical approach to the optimization of skid landing gears. The optimization technique is applied to investigate the trade-off between the landing performances and the gear strength. Sareen et al [74] discusses a non-linear finite element based method of analyzing the structural behavior of helicopter skid gears during a high energy landing.

Another class of energy absorbing devices is skis, which are used for skiing on snow filled surfaces, and their function is similar to that of skids in aircraft. A swiss ski [75] producer has tested composite skis in which laminated Cu-Zn-Al SMA strips are embedded to improve energy absorbing characteristics. Tsoi et al [14] have studied the impact damage behavior of SMA embedded composites.

The summary of the conclusions from the literature in the context of present work can be described as follows: Most of the literature relating to the heat treatments of SE SMA either deal with altering the transition temperature of the alloy [26], [27] or arriving at the optimum fatigue resistance [28],[29]. Very few papers have addressed the effects of heat treatment on energy dissipation properties although Frenzel et al [30] did report on the effect of heat treatment on the damping properties.

The sensory characteristics of SMA have been investigated by quite a few researchers [32] – [37]. Quite a few of them observed that the electrical resistivity shows a linear variation with strain. However the precise measurements of resistivity in relation to the the phase changes as the material is strained is not found in the literature.

References [38]-[42] have investigated the effects of strain rate on the thresholds stress required to form SIM and on the energy dissipation characteristics. A comprehensive study of the effect of a wide range of strain rates on the various parameters of tensile testing up to failure as well as the energy absorbing or damping properties of NiTi super elastic SMAs is not available in the literature.

References [49] – [66] deal with the investigations relating to the fatigue behavior of NiTi elements. These relate to cycling within the elastic range as well as cycling in the elastic –plastic range. The shift of the mean point for the cycling within the elastic range is not found to have been investigated in the literature. Also, for thin wires subject to tensile cyclic loads of very large amplitude i.e. cycling in the elastic-plastic range the feasibility of using the Coffin-Manson equation has not been examined.

References [67] – [73] deal mostly with design and development of metal landing gears with crash worthy features. [74] and [14] deal with embedding SMAs in polymer composites for energy absorption. The serious shortcoming in the designs in which SMA elements are completely embedded in the polymer composites is that the straining of the SMA element is limited by the allowable design strains of the polymer composite (normally around 0.5%). Unless the SMA elements are strained at least in the range of 3-4 % the energy absorption capability remains largely under exploited. Despite all the developments and advances in the skid and ski landing gear design discussed above, there is still substantial scope to reduce the weight of the landing gear further by incorporating new materials and novel designs.

The metallic skids discussed above are generally designed to attenuate the energy generated during normal landings by elastic deformation. Many times they undergo permanent plastic deformation in response to the impact energy of a crash landing. The plastic deformation of metal skids absorbs a significant percentage of the crash landing energy. The drawbacks of such type of metallic skids are the landings are hard (they do not protect the sensitive gadgets) and require frequent replacement because of the hard landings. The metallic replacement of these skids is labor intensive and expensive and further they do substantially add to the weight.

Ideally an efficient skid must have high shock absorption capability (during landing), be affordable, possess low weight, endure sufficient no. of cycles without undergoing permanent plastic deformation (i.e., be crashworthy), have high energy absorption efficiency; facilitate easy maintenance and replacement of worn out parts.

Polymer carbon composites are ideally suited for the design and development of an efficient light weight skid as they have high specific stiffness and high specific strength compared to conventional materials used for landing gear construction. Along with these composites, if SE SMAs having very large energy dissipation capability can be effectively integrated to realize the smart landing gear then it would result in the realization of the efficient smart landing gear system having all the positive features stated in the paragraph above. The SE SMA material investigations have to address the heat treatment, sensory characteristics, strain rate effects and fatigue issues in relation to the energy dissipation characteristics.

1.10: Motivation & Objective:

The landing gear/ shock absorption systems for vehicles in general have evolved substantially over the last few decades. The quest to improve the efficiencies of the various sub-systems using new materials and new design concepts is a continuous process. Polymer carbon composites have high specific stiffness and high specific strength (and therefore weigh less) compared to conventional materials used for landing gear construction. However, they have the limitation of not being able to undergo large elastic deformations. Along with these composites super elastic shape memory alloys have been effectively integrated to realize the smart landing gear which can undergo large elastic (buckling) deformations. The proposed design is of generic nature and provides an alternate method of developing an efficient (high energy dissipation with low system weight) landing gear with satisfactory geometry. It is based on a novel design approach. The design provides two load paths to react the impact loads; the primary and the secondary. The primary load path is stiff and undergoes very little elastic deformation. The secondary load path which is more flexible takes a substantial amount of load, undergoes large elastic deformations. The super elastic SMA is integrated effectively into the secondary load path and forced into a tensile mode of deformation during impact loading and in the process absorbs/dissipates energy. The elements of the primary load path are designed for low strain and large no. of cycles whereas the elements of the secondary load path are expendable after a relatively less number of cycles. This design applies for a “large class of vehicles” including aerospace vehicles (such as airships, rotorcraft and other light unmanned air vehicles). It can also be extended to the automobiles such as motorcycles, cars etc. to serve the purpose of energy dissipation during impact loadings. This design concept can be considered in automobiles as an alternative to the existing shock absorbers. Currently the shock absorber systems in automobiles are part of one single load path. In the place of the single load path design the proposed design consisting of two load paths can be experimentally examined. The effective integration of SE SMA can bring about a substantial benefit in the energy dissipation capability. As stated above this design approach can be extended to a large variety of vehicles.

In this context as a particular example, in order to prove the proposed design concept, the design and development of the Shape Memory Alloy (SMA) based smart landing gear for the RC blimp has been undertaken. The brief description of the RC blimp is given in the next section.

1.11: Brief Description of the Blimp (semi-rigid airship) & Structural Framework: Fig.1.10 shows the schematic of the blimp along with the landing gear unit. The smart landing gear is a sub-system of the blimp which is a semi-rigid airship. Semi-rigid airships are also referred to as blimps [1]. A radio controlled (RC) blimp is referred to as the RC blimp. The blimp is used for weather monitoring, pollution monitoring,

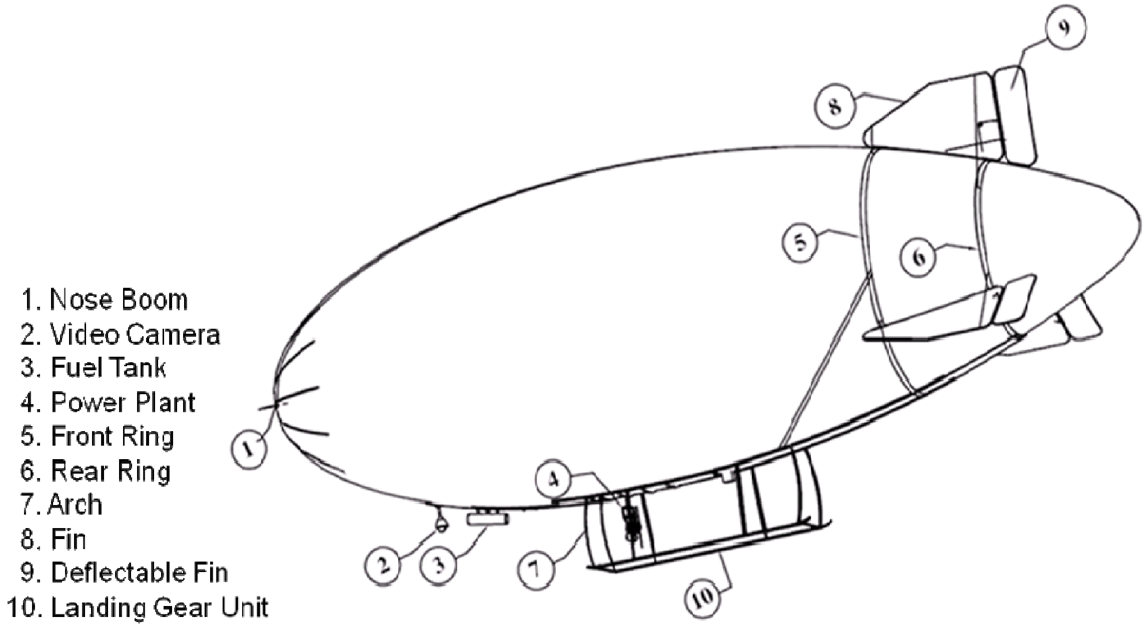

Fig.1.10: Radio controlled blimp.

disaster management, traffic management etc. Helium gas is used to generate the lift for the blimp while a fixed engine provides the thrust. The RC blimp shown in Fig.1.11 has a 320 m^3 volume, measures 18m long and has a maximum diameter of 6m. It is radio controlled from the ground and comprises of various sub-systems such as controls, payload comprising of camera, propulsion, envelope, structural framework (consisting of rings and landing gear) to hold the envelope and the landing gear. The smart landing gear (also referred to as 'skid' at some places) is predominantly carbon composite based. In some select zones for the purpose of insulation glass composites have been used. Mostly wet layup technique with vacuum has been adopted for fabricating the composite landing gear. The SE SMA has been effectively integrated to the carbon composite landing gear. The landing gear is part of the main airframe, which is also predominantly carbon composite. The helium filled nylon fabric envelope of the airship is housed in the airframe. Fig.1.10 also shows the airframe consisting of 2 rings, fins mounted on the airframe for direction control of airship and the smart landing gear. Fig.1.11 shows the schematic of the structural framework including the landing gear secured to the envelope by means of 'dog ears'. In this work the words 'Air Ship' and 'RC Blimp' have been used synonymously.

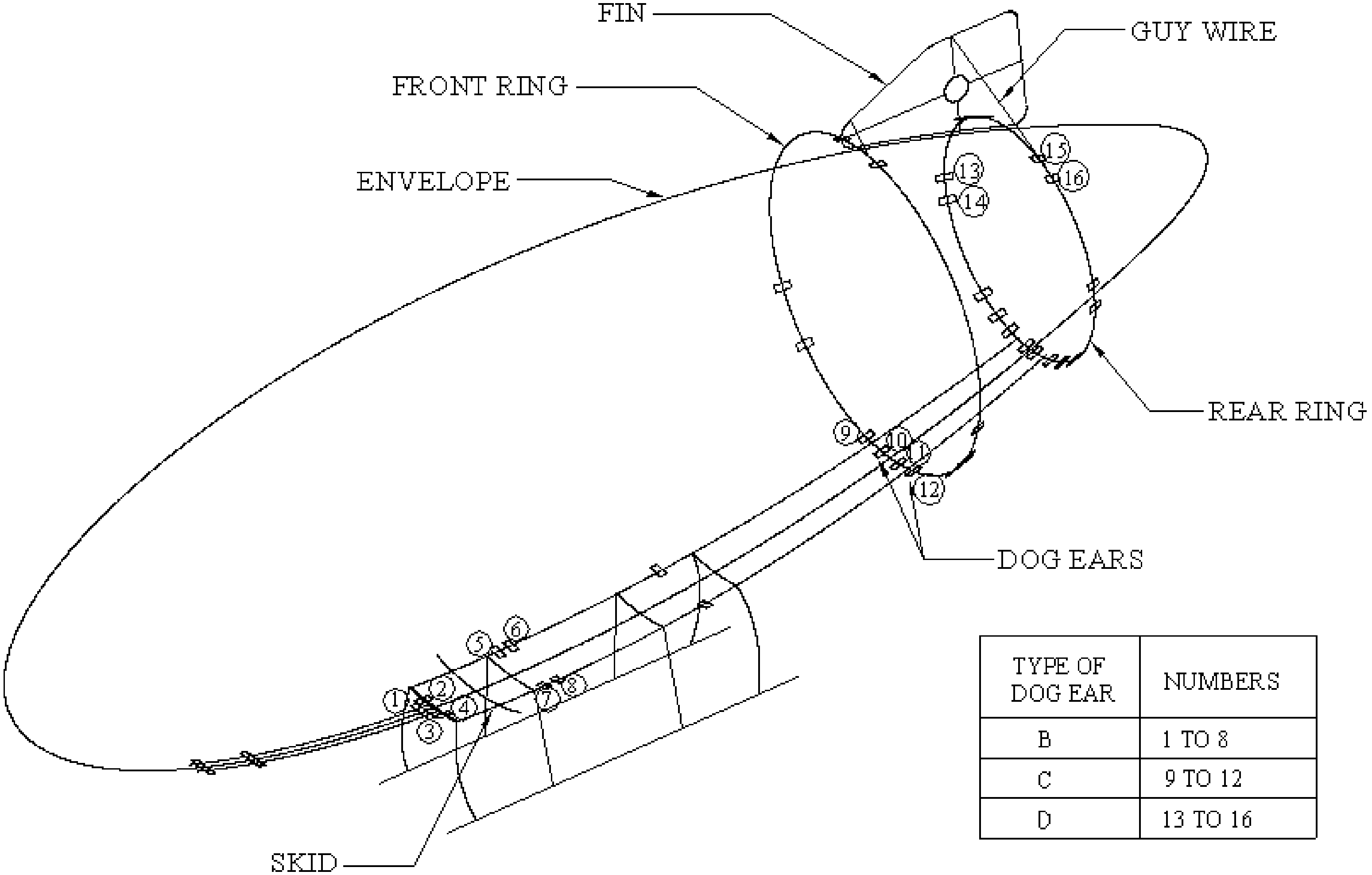

TYPE OF DOG EAR	NUMBERS
B	1 TO 8
C	9 TO 12
D	13 TO 16

Fig.1.11: Schematic of structural framework including landing gear (skid) tied using dog-ear

The smart landing gear comprises of a landing beam, an arch and a super elastic Ni-Ti SMA element. A judicious combination of Carbon Fiber Reinforced Plastic (CFRP) for the landing beam, cane (naturally occurring plant product) wrapped with CFRP for the arch and super elastic SMA is used in the development. The landing gear is secured to the main body (gas filled PVC nylon fabric) of the semi-rigid airship by means of 'dog ears'. An appropriate sizing of the arch, landing beam and SE SMA is arrived at to meet the dual requirement of low weight and high energy dissipation in order to ensure soft landings when the airship impacts the ground. The soft landing is required to ensure that shock and vibration are minimized (to protect the sensitive payload). The inherently large energy dissipating character of the super elastic SMA element in the tensile mode of deformation and the crash worthy features of the landing gear provides the ideal solution. A simple fabrication approach is followed to realize the SE SMA incorporated carbon composite landing gear unit. The required static tests have been conducted on the arch and the arch-SMA combination.

1.12. Problem Definition: a) Investigation of the material characteristics to cover the heat treatments, sensory characteristics evaluation, strain rate and temperature effects, cyclic and fatigue loading that have a bearing on energy dissipation capability of super elastic Ni Ti SMA wires. b) Design, development and testing of the smart landing gear (for the RC blimp incorporating SE SMA into polymer composites) that meets the stringent weight budget of 16 kgs and possesses maximum energy dissipation capability.

Fig.1.12 shows the flow chart of all the experiments that have been carried out in relation to the investigations concerning the SE SMA, polymer composites and the testing of the landing gear sub-unit.

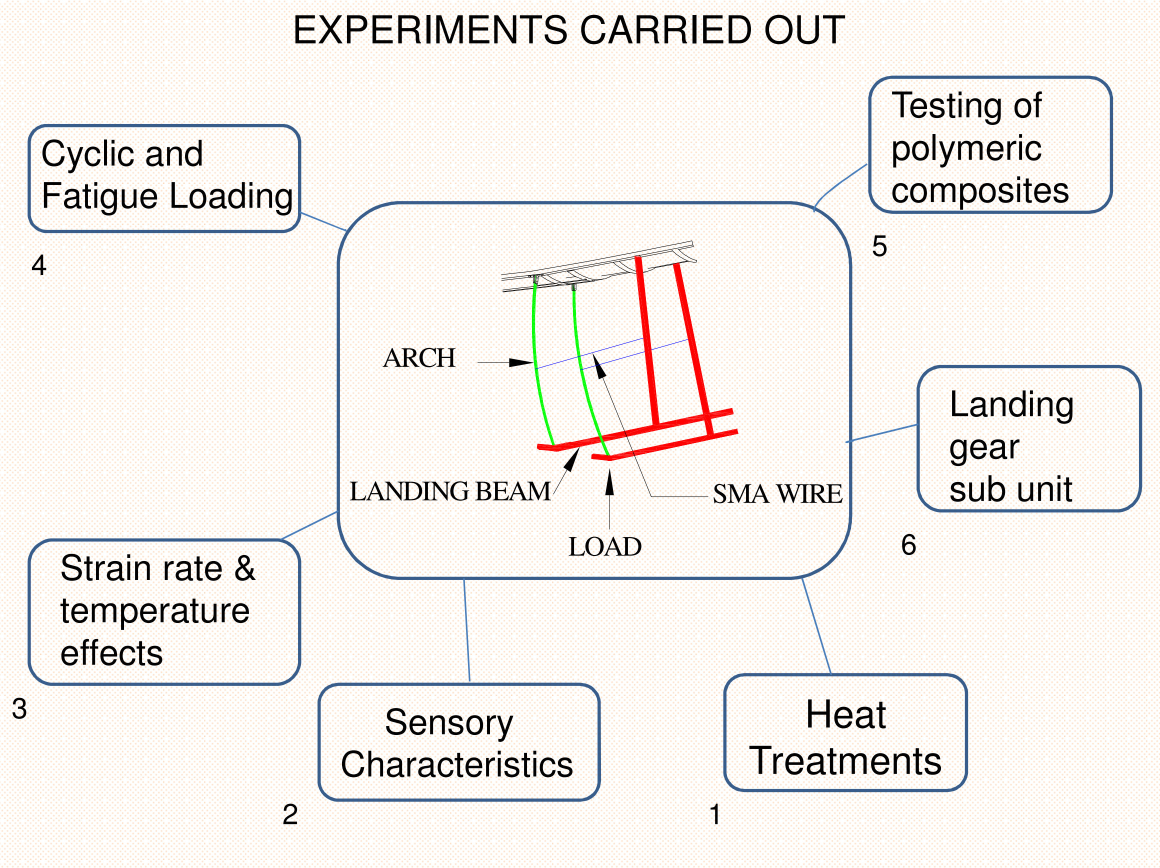

Fig.1.12: Flow chart of different experiments carried out in sequence 1-6.

Chapter 2: Material and Experimental Details

2.1. Introduction:

The development of the smart landing gear for the airship has involved the material characterization and testing of a wide range of materials in relation to a broad range of varying parameters such as temperature, sensory characteristics, heat treatments, strain rate, fatigue property evaluation etc. It has also involved the testing of the landing gear sub-unit. The details of the material testing and the testing of the assembled landing gear sub-unit incorporating the SE SMA element are presented in this chapter. The materials tested include polymeric composites, SE SMA and PU (polyurethane) coated nylon fabric out of which the envelope of the airship is made. The landing gear is secured to the envelope by means of ‘dog ears’ which are also made of PU coated nylon fabric. The landing gear is built primarily using carbon composites. The wet layup fabrication process has been followed. At some zones where the SE SMA is integrated to the landing gear glass composites have been used for electrically insulating the ends of the SE SMA. The polymeric composite technology is based on the polymerization reaction between the resin and the hardener which is exothermic in nature. The exothermic reaction releases toxic products which have to be properly bled out of the component. Further the wet layup requires to be compacted to obtain good quality components. The requirements of compaction and bleeding out the toxic exotherms require that the wet layup component be kept inside a vacuum bag that is continuously evacuated during cure. The vacuum bagging involves the usage of a wide range of tooling and bagging materials apart from the resin systems and fabrics. The prominent are discussed.

2.2. Materials Used:

2.2.1. Carbon Composites

Carbon composites are a mixture of carbon fibers and resin systems such as epoxies. They are very light with a density of 1.6 g/cm^3[1]. The carbon fibers are made from carbonization of organic precursor fibers such as polyacrlonitride (PAN) followed by graphitization at high temperatures. Carbon fibers are ideally suited for applications where the requirements of stiffness and strength are demanding. They are used in aerospace, transportation, sports, machinery, cryogenic & medical sectors. Here, carbon plain weave fabric of thickness 0.23 mm has been used.

2.2.2. Glass Composites:

Glass composites are a mixture of glass fibers and resin systems such as epoxies. The density of glass composites is 1.8 g/cm^3 [1]. Most glass fibers are based on silica (SiO_2). The two types of commonly used glass fibers are 'E glass' and 'S glass'. E glass has good insulation properties and is used for electrical applications whereas S glass has good strength properties and is used for structural applications.

2.2.3. Epoxy Resins:

Epoxy material systems are the most widely used in the manufacture of advanced composites for airframes and other structural applications. They are superior in terms of chemical resistance, adhesion to fibers, dimensional stability, and good hot wet performance. Here, the vacuum assisted wet layup technique with LY5210 resin and HY932 hardener has been used. The resin system is especially suited for use in combination with glass or carbon fabric. The pre-curing of the system is at room temperature. The system is resistant to temperatures upto 180-190 °C. The other features of the epoxy resin system are good wetting out characteristics, variable layup time and possibility of pre-curing at room temperature [2]. The viscosity at 25° C is 2400-3000 for the resin, 1500-3000 for the hardener and 80-180 mPa s for the accelerator (DY 219) respectively. The density at 25° C is 1.15-1.2 for the resin, 1.05-1.1 for the hardener and 1.2-1.3 g/cm^3 for the accelerator respectively. The flash point is 170 °C for the resin, less than 200 °C for the hardener and 108°C for the accelerator respectively.

The matrix (Araldite: Hardener: Accelerator) is mixed in the ratio of 100:56:1 parts by weight. The pot life is 2hrs for 1 kg of mixture and the demoulding time after pre-curing at 40^{0}C is 20-32 hrs.

2.2.4. Uni-Directional (UD) Prepreg:

UD prepregs of CFRP used in the arch are cut from prepreg rolls. These rolls are usually kept in a cold chest maintained at a temperature of -20°C. These rolls are taken out from the cold chest and kept at room temperature for at least 8 hrs before fabrication. The prepreg is cured in the autoclave at a pressure of 7 bar and temperature of 180°C.The prepreg is inside a vacuum bag, which is evacuated from outside the autoclave. The vacuum pressure of about 1 bar is in addition to the autoclave pressure of 7 bar.

2.2.5. NiTi Super Elastic SMA:

The density of NiTi SMA is around 6.45 g/cm^3. The material used for the study is 0.6mm super elastic NiTi SMA in the wire form. The nominal chemical composition of the wire was Ni = 54.3% and Ti = 45% by weight. The cold worked material was heat treated for 15min at 500°C. This heat treatment gives the optimum energy dissipation and was arrived at after several trials. The behavior of the “as received” cold worked, heat treated and completely annealed wire is discussed in the next chapter. The transformation temperatures of the heat-treated material were obtained from the Perkin Elmer Differential Scanning Calorimeter.

2.2.6. Cane:

The cane used in the construction of the arch of the landing gear is a naturally occurring plant material whose density is comparable to that of wood. The modulus can be as low as 4GPa and the failure strains are large compared to polymeric composite materials. The cane has good bending and fatigue properties.

2.2.7. PU Coated nylon fabric [3]:

The envelope of the air ship is made of thermoplastic PU (polyurethane) coated plain woven nylon fabric. The mass of the fabric is 385 g/m^2. The strength to mass ratio of the fabric is in the range of 0.58-0.71 kgf/ (g/m^2). The helium permeability is 2ltrs/m^2/day. The peel strength is 3 kg/ 2.5 cm. The dog ears which are used to secure the landing gear to the envelope are also made of the same material.

2.2.8. Other tooling materials:

The carbon composite technology requires a wide range of tooling and bagging materials. The tooling can be hard or soft tools. Soft tools are also referred to as caul plates and are usually used in conjunction with hard tools to conform to the desired shapes. The soft tools can either be thin glass or aluminium foils or thin FRP or polymeric materials. Here in this development soft male cores made of polystyrene foam (thermocol) have been used for the square tubes of the landing gear sub-unit. The thermocol density is around 40 kg/m^3. The carbon fabric and resin wet layup is wound around the soft thermocol core and the entire assembly is cured using matched die technique. The dies are made of conventional wood.

For the arch a combination of prepreg and wet layup (comprising of plain weave carbon fabric and LY5210 resin and HY932 hardener) has been used. Soft thermocol cores and hard plaster of paris moulds have been used on the outside surface. The assembly has been cured under a vacuum bag at atmospheric pressure. Several bagging materials such as peel ply (woven nylon clothes) for better surface finish and breather materials (non-woven polyester) for absorbing excess resin during curing have been used.

2.3. Experimental Details:

The experiments/testing conducted broadly fall under the following categories:

a) Study of sensory characteristics, heat treatments, strain rate effects, cyclic and fatigue behavior of SE SMA.

b) Tensile testing of Polymeric Composites.

c) Testing of the smart landing gear sub-unit.

d) Testing of PVC nylon 'Dog Ears'.

2.3.1: Experiments relating to testing of SE SMA:

The investigations relating to the study of the behavior of SE SMA is central to this thesis. The studies involve: i) heat treatments to optimize the energy dissipative properties, ii) sensory characteristics evaluation which is simultaneous with the energy dissipation function (thereby exploiting the bi-functional property of SE SMA), iii) determining the effect of strain rate on energy dissipation and related properties and iv) cyclic and fatigue loading evaluation. All the above tests have been done on the 0.6 mm diameter wire. All the samples were straight and of uniform cross section. The lengths of the wire used have been different in different places to suit the testing/heat treatment conditions. The cold worked wire typically of length 1 meter has been loosely wound round the metal spool and the heat treatment has been done for 15 minutes at the desired temperature followed by water quenching. For determining the sensory characteristics in order to minimize the adverse effect of noise on the voltage measurements across SMA a sizeable length of 500 to 650 mm has been used. For the study of strain rate effects the length used is 100 mm in order to minimize the grip deformation effects on the displacement measurements. However for those tests involving cyclic and fatigue studies a much shorter length of 30 mm has been used in order to ensure that the wire does not get into buckling. In the landing gear device the length used was 1000 mm which was dictated by the

Fig.2.1: Tinius Olsen testing unit for tensile and cyclic loading

topology of the landing gear system. The tensile and cyclic testing of the SE SMA elements was done using a Tinius Olsen H 10 KT computer controlled tensile testing machine as shown in Fig. 2.1. The cross head of the machine was calibrated using Non Contact Displacement laser transducer of micro epsilon make. The positional accuracy of the cross head is 0.001 mm. Load cells were calibrated using INSTRON dead weights. The SMA specimens were secured in the wedge type of grips by mechanical fastening. The grips were properly aligned in accordance with the instruction manual [4]. These conditions are the same for all types of tensile, cyclic and fatigue tests mentioned in the subsequent sections. The environmental chamber that comes with the same tensile testing machine was used for high and low temperature tensile tests. The chamber temperature range is variable from -70 ℃ to 300^{o}C. The temperature calibration was done using standard thermocouples. The system has a forced air circulation system which ensures temperature uniformity of ±0.1 ^{o}C in the working zone under steady state conditions. The data acquisition and control software (i.e. QMAT) has been supplied with Tinius Olsen tensile testing machine. The data was stored in *.csv formats and was plotted using Microsoft excel.

2.3.2: Heat treatment on SE SMA:

Heat treatments are done on SMAs to obtain the desired properties. In the present context it is necessary to find the heat treatment at which the energy dissipation characteristics are optimum. The other requirements of austenite finish temperatures being less than room temperature and minimum plastic set in the material after cycling also have to be met. In order to arrive at the optimum point, heat treatments of the cold worked wire have been carried out at 450, 500, 550 and 600 ℃

respectively followed by quenching for 15 minutes. Subsequently both the cold worked and heat treated wires have been tested up to failure. For the heat treatment a refractory furnace whose temperature control accuracy within the working zone is better than +/-1 °C has been used.

2.3.3: Sensory Characteristics of SE SMA:

The objective of these tests is to establish the sensory characteristics of SE SMA which is integrated in the landing gear sub-unit. The determination of sensory characteristics involves the following:

a) Cyclic stress-strain testing for strain amplitude of 6 %.
b) Simultaneously pass a constant current of 100 mA through the SMA wire and measure the change in voltage across the SMA.

The lengths of the wire sample used for testing range from 100 to 650 mm. The specimens were straight with uniform cross section. Fig.2.2 shows the 4 probe method of voltage measurement. This eliminates the adverse effects due to path resistance. Fig.2.3 shows the SMA wire fixed to the tensile testing machine and the mounting of the 4 probes. The strain controlled stress-strain cycling is done while the current is passed simultaneously. A constant current (i) is passed through the SMA through one set of leads while the voltage across SMA is measured through a second set of leads. The resistance (R) is calculated using ohm's law,

$$R = V/i \text{ ------------- } (2.1)$$

Where 'V' is the voltage and 'i' is the current.The electrical resistivity (ρ) at any temperature is obtained by,

$$\rho = R\, a/l. \text{ --------------- } (2.2)$$

where ‘a’ is the area of the cross section of the SMA element and ‘l’ is the length of the SMA element. Since large strains of the order of 6% are measured, the continuous changes in the parameters ‘a’ and ‘l’ are taken into account while computing resistivity. It is assumed that the product of ‘a’ x ’l’ = $\underline{V}$ where $\underline{V}$ is the volume is a constant. During the A to M transformation the increase in length is offset by a decrease in area such that the volume is a constant. Likewise, the decrease in length is compensated by an increase in area during the reverse transformation.

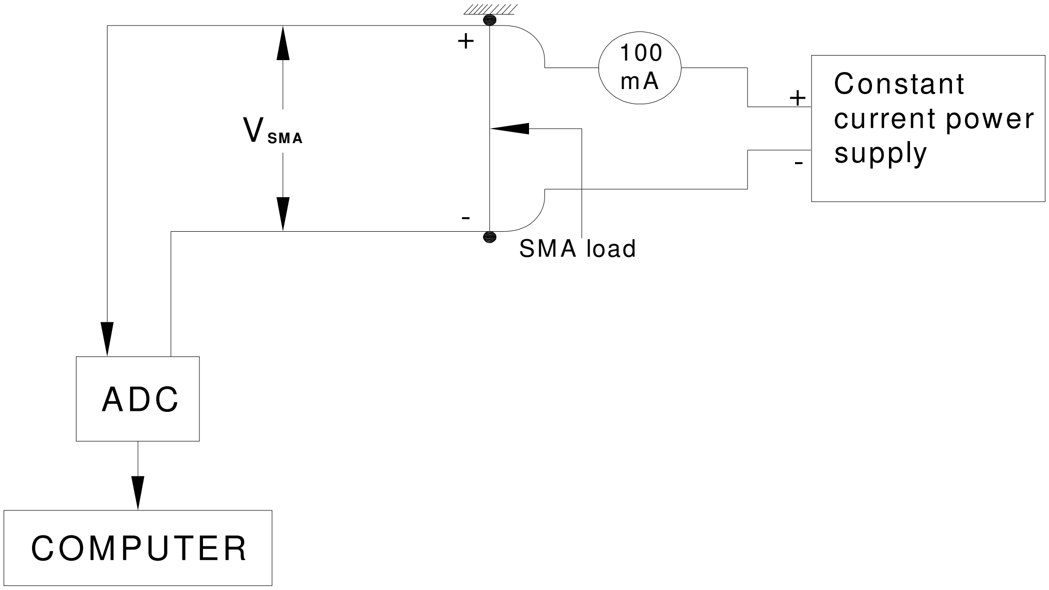

Fig.2.2: Schematic of experimental set up for evaluation of sensory characteristics.

2.3.4: Strain rate studies:

The SE SMA element that is used in the landing gear is subject to a wide range of strain rates. The tensile and cyclic testing at different strain rates was done using a Tinius Olsen H 10 KT computer controlled tensile testing machine as shown in Fig. 2.1. The length of the wire used for the first set of tensile tests was 100 mm and for the second set which involved both tensile and cyclic tests the length used was

30mm. This was because buckling was observed for the 100 mm length samples and therefore they were found not suitable for the cyclic tests. The strain rates of interest range from the 'static' tension tests using hydraulic or screw driven machines (i.e., 10^{-5} to 10^{-1}/s) to the 'dynamic' tests (i.e., 10^{-1} to 10^{2}/s or even higher). In this study taking into the account the type of machine and the end grips available the strain rates that are studied are in the range of 3.3×10^{-5} to 0.13/sec. Section 2.3.5 pertains to samples of 100 mm length and sections 2.3.6, 7 & 8 pertain to samples of 30 mm length.

2.3.5. Tensile testing at different strain rates & temperatures for 100 mm length wire:

The tensile testing was done using a Tinius Olsen H 10 KT computer controlled tensile testing machine. The following 2 types of experiments were conducted on the 100 mm length NiTi wires:

1. Tensile tests up to failure for different strain rates from $3.3X10^{-5}$ to $1.33X10^{-1}$/sec (i.e., 0.2 to 800%/min) at room temperature (27℃).
2. Fractography studies on cold worked and a few selected heat-treated specimens after tensile testing under the following condition:
    a) At different temperatures i.e., -50, 27℃ (Fixed strain rate of $3.3X10^{-4}$/sec (2%/min)).
    b) At low ($3.3X10^{-5}$/sec (0.2%/min)) and high ($1.3X10^{-1}$/sec (800%/min)) strain rates at room temperature.

2.3.6. Tensile testing at different strain rates & temperatures for 30 mm length wire:

The following 2 types of experiments were conducted on the 30 mm length NiTi wires:

1. Tensile tests up to failure for different strain rates from $3.3X10^{-5}$ to $3X10^{-2}$/sec (i.e., 0.2 to 180 %/min) at room temperature (27℃).
2. Fractography studies on cold worked and a few selected heat-treated specimens after tensile testing upto failure:
   a) At different temperatures i.e.,-50, 25 and 100℃ respectively(Fixed strain rate of 2%/min (0.6mm/min)).
   b) At low ($3.3X10^{-5}$/sec (0.2%/min)) and high ($3X10^{-2}$/sec (180%/min)) strain rates at room temperature.

2.3.7. Cyclic Loading:

The cyclic tests presented in this work deal with the cycling of 0.6 mm diameter SE SMA wires of 30 mm length. The machine is set in the strain control mode during these experiments. The cyclic amplitudes of 6 and 8 % respectively are within the elastic regime for the SE SMA. One set of experiments involve determining the strain amplitude at which the energy dissipation is maximum with minimum permanent set in the material after the first cycle. The second set of experiments involves strain controlled cycling up to 100 cycles and studying the evolution of energy dissipation and plastic strain parameters. The cyclic tests for fixed strain amplitude of 6 and 8% have been carried out:

a) At different strain rates in the range of 0.2 to 180 %/min.
b) Up to 100 cycles for a strain rate=30 %/min at strain amplitudes of 6 & 8 %.

2.3.8. Fatigue Loading:

The stress-strain cyclic fatigue loading experiments of the NiTi Super elastic wire of 30 mm length and 0.6 mm diameter were also conducted on the Tinius Olsen H 10 KT computer controlled tensile testing machine. The strain cycling was done at a strain rate of 1mm/sec. The wire was first loaded up to 100 N, which corresponds to a strain of 1.5 %. Then from here it was strain cycled to different strain levels, viz; 1.5, 2, 2.25, 3 and 4 mm which correspond to strains of 5, 6.66, 7.5, 10, and 13.33 % respectively above the initial strain of 1.5%. This results in total strain values of 6.5, 8.16, 9, 11.5 and 14.83% respectively. The evolution of the plastic strain parameter is the key to predicting fatigue life. The plastic strain between consecutive cycles from different failure tests is taken and constants are derived. These constants are fit into the Coffin-Manson relationship for predicting the fatigue life.

2.4. Testing of Polymeric Composites:

Fig.2.3 shows the Zwick 150 Universal Testing Machine that was used for the tensile and in plane shear testing of polymeric composites. The fabrication and testing was done in accordance with the Zwick instruction manual [5] and ASTM standards [6], [7]. The dimensions of the test specimen were as follows: length = 250 mm, width = 15 mm, thickness = 1 mm. the dimensions of the end tabs were as follows: length = 56 mm, thickness = 1.5 mm and tab bevel angle = 90°. The properties which are of interest are; ultimate tensile strength, failure strain, modulus of elasticity and poison's ratio. The geometry of the standard test specimen is as per the ASTM standards. The extensometer gauge length is 50 mm and the maximum measurable elongation is 13.5mm. The loading rate is 1 mm/min. The properties are calculated in accordance with the ASTM standards [6].

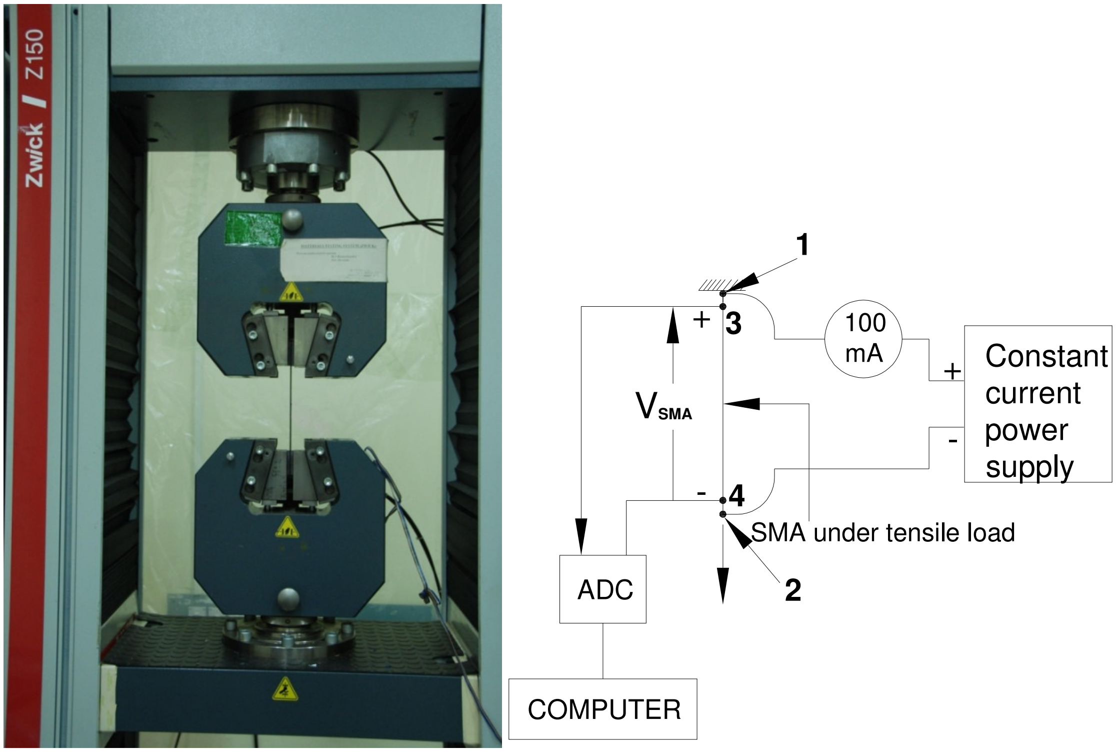

Fig.2.3: Tensile testing of polymeric composites on Zwick UTM.

For the tensile test of the ±45° laminate the dimensions of the test specimen are: length = 250 mm, width = 25 mm, thickness = 2.5 mm. The loading rate is 2 mm/min. The Test Expert software that comes along with the machine generates the data in the required format that can be read by Microsoft Excel programs for the purpose of plotting the results of the test.

2.5. Testing of Landing gear sub unit containing SE SMA and Polymer Composites:

The Radio Controlled blimp (RC blimp) for which the smart landing gear is designed is a non-rigid airship. Fig.1.1 shows the structural framework comprising of two rings and the landing gear built using primarily carbon composites. The structural framework serves as a base to mount the fin and rudder units in addition to holding the envelope.

The landing gear is part of the structural framework. Fig.2.4 shows the dotted envelope ‘A’ comprising of the landing beam, arch and SMA considered for testing. The length of the Ni Ti SMA wire used for the testing in the landing gear sub-unit was 1000mm. The specimens were straight and of uniform cross section.

The modulus of the arch and beam are obtained from test specimens cut from the actual component using a Zwick UTM. The load cells used in the experiment were also calibrated using the same UTM. The displacements were crosschecked using a Micro Epsilon laser sensor. Data acquisition was done using a National Instruments card.

The experiments were conducted for three configurations. Fig.2.5 shows the test set up. For configuration 1, the subunit comprises of a segment of the landing beam, CFRP arch with cane and SMA. Configuration 2 is the same as configuration 1 but without SMA and for configuration 3 the SMA was replaced with the steel wire. In all the three configurations the load was applied in increments through the load cell 1. The length of the landing beam sub segment considered for tests was 1112 mm and the height of the arch was 1240 mm. Load cell 1 monitors the total vertical load. Load cell 2 monitors the load taken by the arch. Load cell 3 monitors the SMA load and steel wire load for the configuration 1 and 3. Fig.2.5 also shows the vertical and horizontal deflections δ_v and δ_h respectively measured using linear scales. Fig.2.6 is the photograph showing the testing of the landing gear sub-unit. Table.2.2 gives the landing gear sub-unit testing summary.

Table.2.2: Landing gear testing summary

Configuration	Loading details
C1- with SE SMA	Max loading upto 1250 N
C2- without SE SMA	Max loading upto 1000 N
C3- replaced SMA with a steel wire	Max loading upto 1200 N

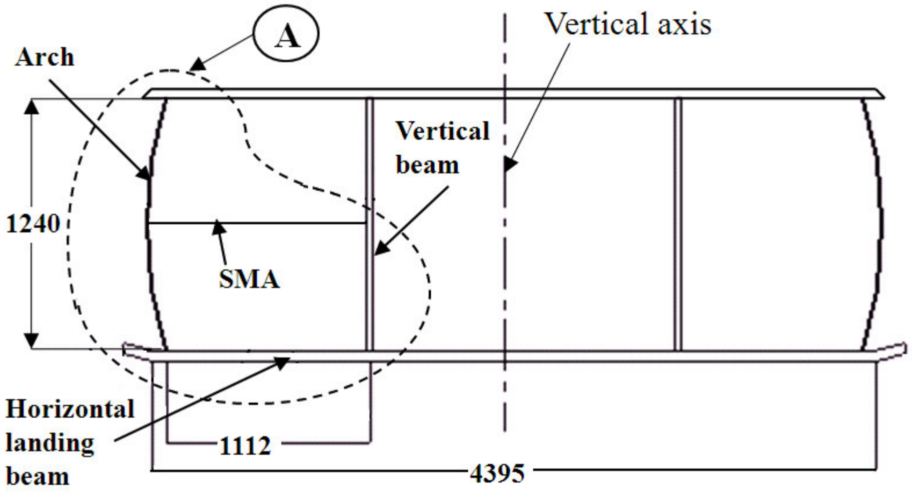

Fig.2.4: The configuration of the landing gear seen from the side.

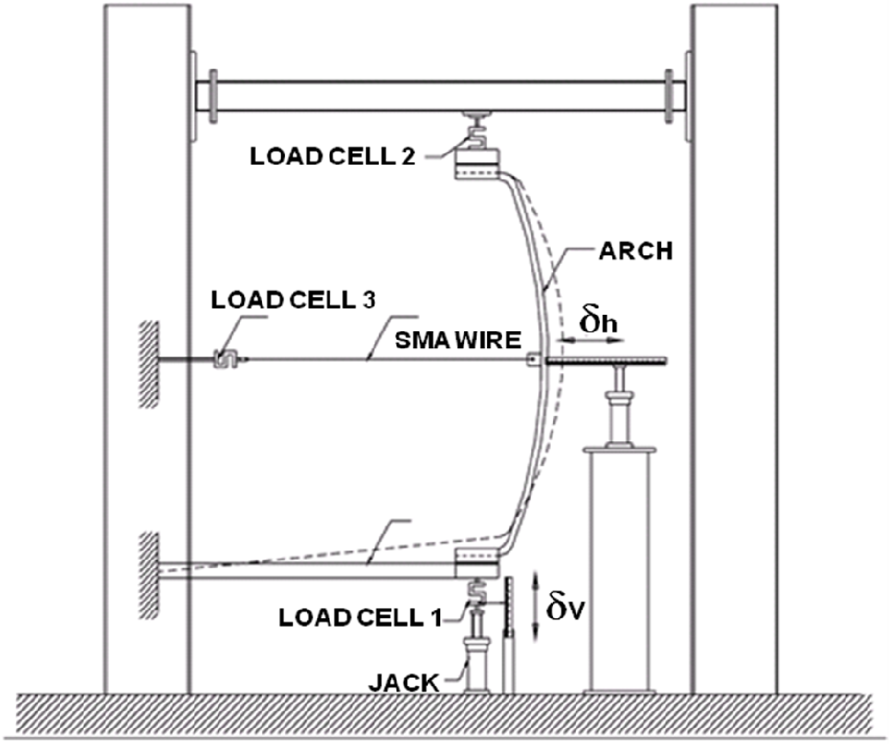

Fig.2.5: Experimental setup for arch and landing beam segment testing using SMA.

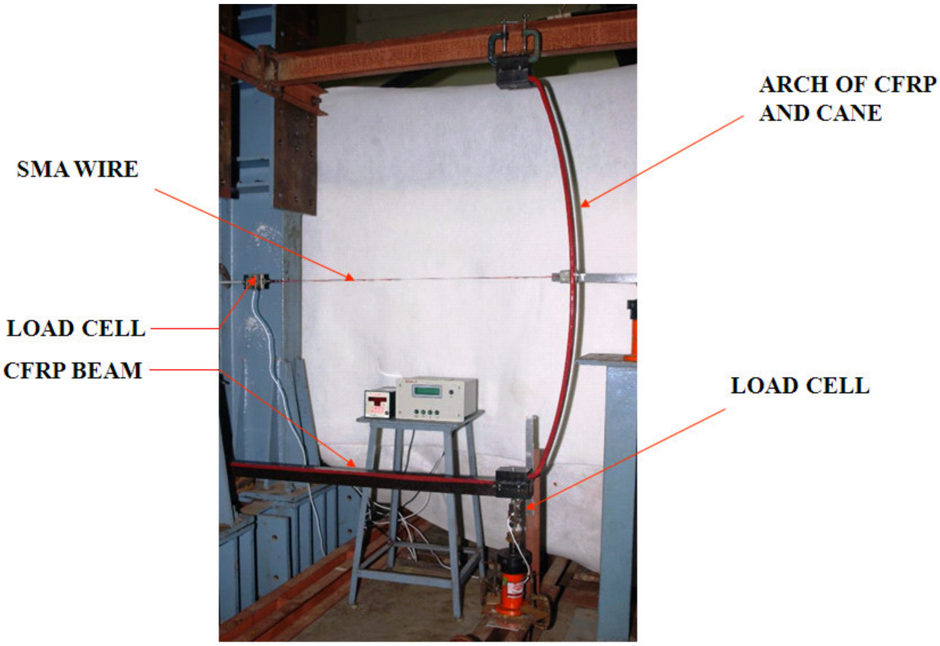

Fig.2.6: Testing of arch using SMA wire.

2.6. Testing of dog ears:

The landing gear is secured to the envelope and to the frame by means of dog ears. Fig.1.2 shows the dog ear arrangement on the landing gear and the structural framework. Three different test schemes [8] were adopted for conducting the static tests of four types of dog ears. Fig.2.7 shows the schematic view of the test scheme 1 dealing with the dog ear having 52 mm flap width (type b) which is used to tie the landing gear to the envelope. This was tested applying the load through mechanical jack using calibrated load cell. Deflections were monitored vertically during the loading. Fig.2.8 shows the different types of dog ears.

The results of the Dog ear testing are discussed in chapter 7.

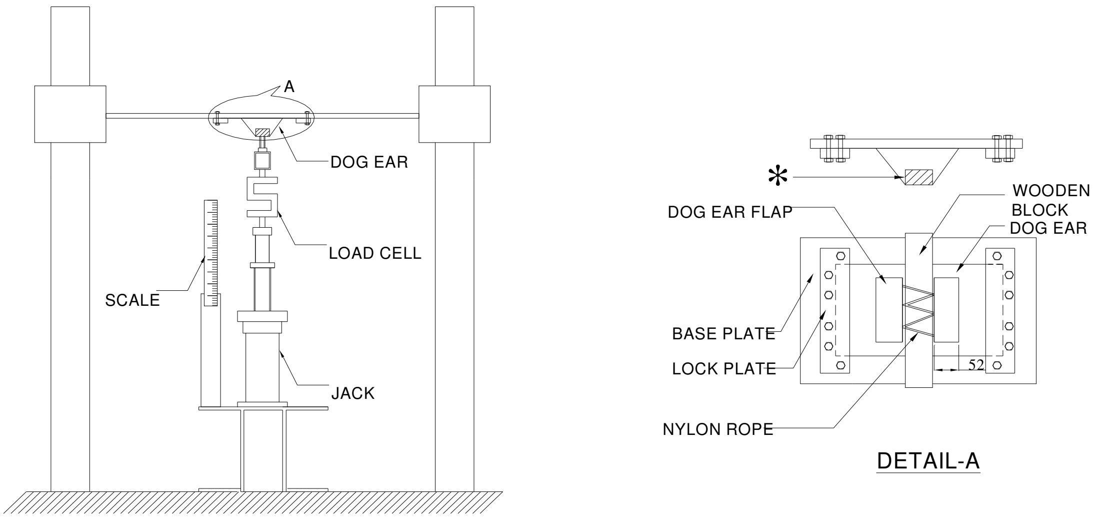

* - Wooden block of identical geometry as the square tube landing gear beam

TEST SCHEME-1 DOG EAR TYPE-b
(FLAP WIDTH-52mm)

Fig.2.7: Schematic view of the test setup for static testing of dog ear of RC blimp

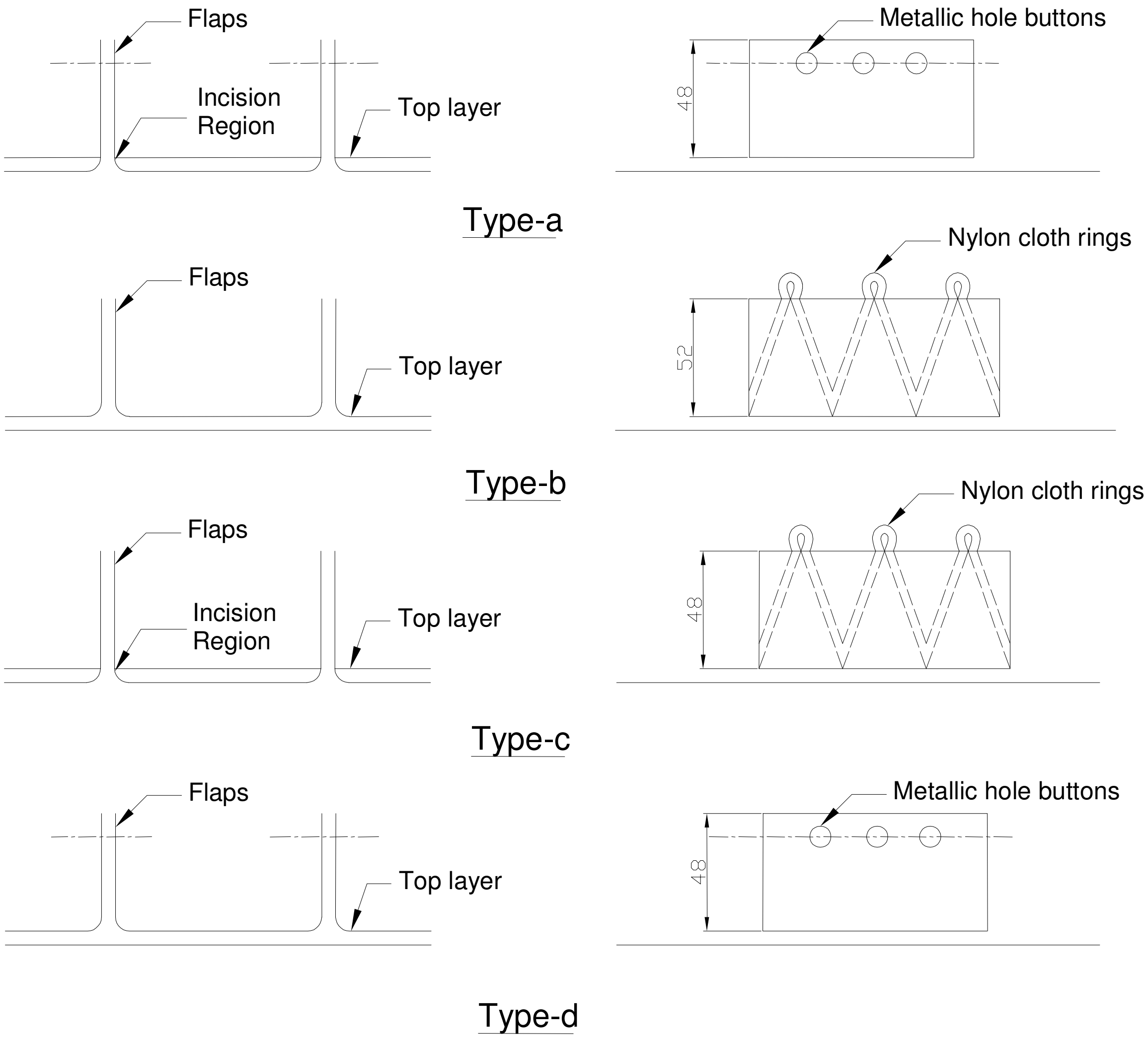

Fig.2.8: Different configurations of dog ears labeled; type 'a' to type'd'

2.7: Rationale for the use of materials:

The key materials used in the fabrication of the landing gear are epoxy polymer based carbon and glass composites, naturally occurring cane and NiTi SE SMA. The rationale behind the use of these materials is explained as follows:

i) Polymer carbon composites: The weight budgets for the landing gear are very stringent. The improved smart landing gear has to be lighter than the conventional aluminium landing gear and still ensure soft landings. Only then the use of advanced materials and fabrication processes for the landing gear is justified. Polymer carbon composites have high specific stiffness and high specific strength compared to other structural materials such as aluminium and hence is being proposed for the landing gear and other structural components of the airship.

ii) Polymer glass composites: The glass composites have been used in a small zone to insulate the SE SMA at the ends where it is joined to the carbon composite arch and the vertical beam. This is because the SE SMA is designed to have a small current flowing in it always to perform the sensory function. Carbon being a electrical conductor, glass composites are used in these segments for the purpose of electrical insulation.

iii) NiTi SE SMAs: Nickel Titanium (NiTi) SE SMA has been chosen for the landing gear as they have high energy dissipation capability compared to other materials such as carbon spring steels, aluminium or structural steels. Also, the NiTi SMAs can be joined to other metals, have good thermomechanical stability, possess superior structural properties and exhibit easier control of transformation temperatures through heat treatment compared to previously discovered shape memory alloy systems such as Cu-Zn-Al or Au-Cd systems. They, in fact, offer the possibility of wide use in many structural, mechanical and other engineering applications.

iv) Naturally occurring cane:

The reinforcement for the arch is naturally occurring cane. The core is generally required to be light in weight and generally only provide the shear stiffness. However, here since the arch has to undergo large elastic deformations the core has to possess both shear and longitudinal bending stiffness. Being a highly fibrous material having low density the cane was chosen here as the reinforcing core. The cane enables the arch to undergo large elastic deformation

Chapter 3: Effect of Heat Treatment on Energy Dissipation

3.1. Introduction:

The heat treatments given to SMA's are the key to control of the mechanical properties. A large variety of heat treatments have been resorted to in order to improve the mechanical properties. In this context it is necessary to understand the differences in the quasi-static mechanical behavior of the cold worked (as received) and heat treated/annealed NiTi SE SMA wires. The combination of cold work in the martensite together with subsequent anneals is adopted to improve various SMA properties. The SE SMA material that is only cold worked has no martensitic plateau on the stress-strain curve, but possesses very high yield strength. Annealing will restore the plateau but decrease the yield strength. The heat treatment studies carried out by Duerig et al , Otsuka et al ,Yeung et al, D. Faviera et al ,Yan et al , Zinelis et al, Frenzel et al , Liua et al ([24] – [31]) and their limitations in relation to the present work has already been discussed in chapter 1. In this study the focus is to select the heat treatment temperature that gives the optimum energy dissipation properties.

3.2. Optimized energy dissipating characteristics:

Fig.3.1 shows the comparison of stress-strain behavior (at 27 °C and strain rate of 2 %/min) of the SE SMA in the cold worked and heat treated conditions. The cold worked wire has relatively less failure strain which is of the order of 8%. The 450 °C heat-treated wire has a high plateau stress which is not desirable from the device point of view. The wire which is heat treated at 500 °C has a plateau stress which is desirable from the requirements point of view of the landing gear. The wires heat treated in the 550-600°C range have very large failure strains as high as 70-80%. The heat-treated material is obviously the candidate for building the energy absorbing devices. The heat treatment at 500°C for 15 minutes gives the optimum energy dissipating characteristics. The discussions pertaining to this is as follows: Fig.3.1 shows the comparison of stress-strain behavior of the SE SMA in the cold worked & heat treated conditions. The heat treatment (HT) has been carried out at 450, 500, 550 & 600°C respectively for 15 minutes followed by quenching in water. It is clear from the Fig.3.1 that the

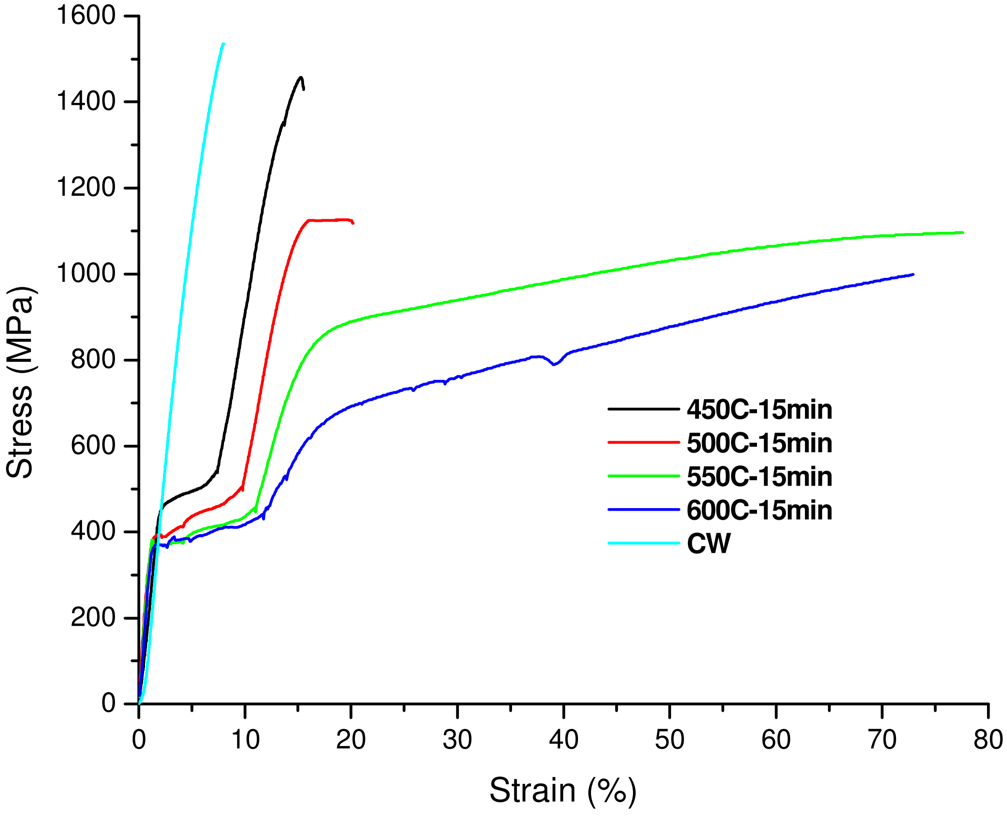

Fig.3.1: Stress vs strain plot for super elastic NiTi SMA.

cold worked wire has relatively less failure strain and exhibits almost linear elastic behaviour until failure. The ultimate stress exceeds 1500 MPa. In fact NiTi SE SMA alloys are known to exhibit hysteresis free linear pseudo elasticity with elastically recoverable strains as high as 4% [1]. This pseudo elasticity is manifest over a wide range of temperatures. However, a further discussion on linear pseudo elasticity in cold worked NiTi alloys is outside the purview of this thesis. From Fig.3.1, the important parameters viz., the loading plateau stress (or the austenitic yield stress) modulus of elastic deformation of SIM (E_{SIM}) and failure strain are studied. These are tabulated in Table.3.1.

Table.3.1: Variation of mechanical properties with HT temperature

Temperature (°C)	Loading plateau stress (σ_L) in MPa	SIM modulus (GPa)	Failure strain (%)
450	440	15	15.6
500	400	13.75	14.4
550	360	8.7	77.6
600	380	4.7	73

The focus in this chapter is on the energy dissipation characteristics. Table.3.2 contains the various parameters related to energy dissipation.

Table.3.2: Variation of dissipated energy and residual strain with HT temperature

Temperature (°C)	E_d (MJ/m^3)	Residual strain ($\in_r$) (%)	Unloading plateau stress (σ_U) in MPa
450	8.53	0.3	290
500	12.58	0.1	120
550	13.22	0.2	125
600	13.68	0.4	72

Fig.3.2 shows the energy dissipated for various heat treatments (test temperature = 27 °C & SR = 2 %/min). It is clear that the dissipated energy is high for the heat treatments in the range of 500-600 °C. However there are other criteria that need to be taken into account before arriving at the optimum heat treatment temperature and the same is discussed.

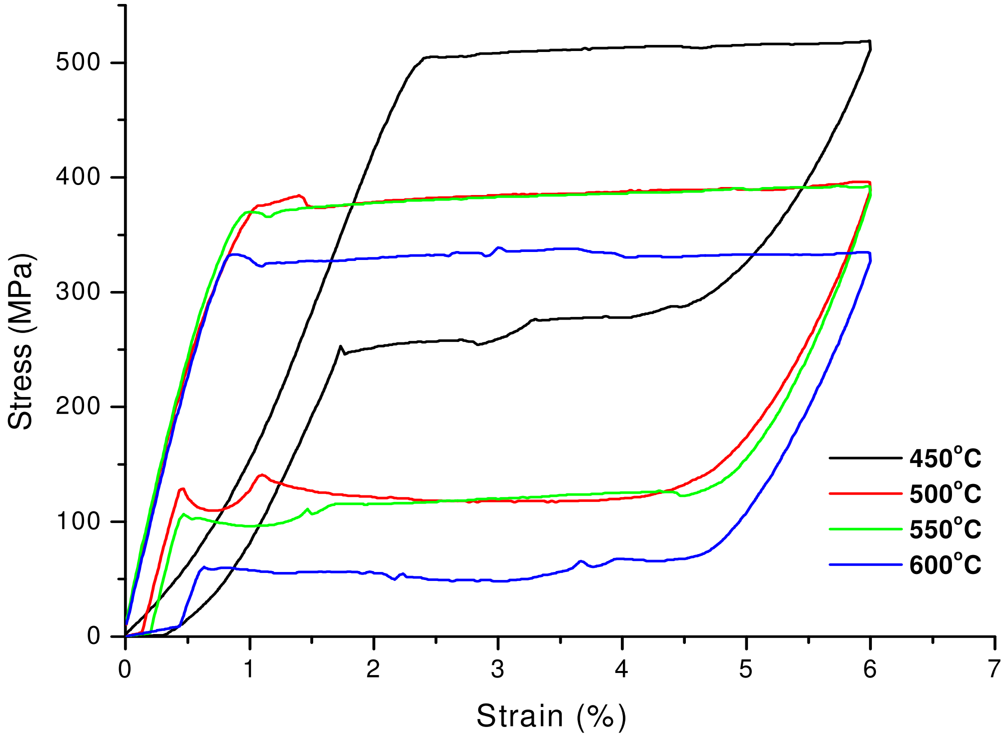

Fig.3.2: Energy dissipation for different heat treatments for 6% cyclic amplitude

Figs.3.3 & 3.4 shows the loading plateau stress and failure strain plotted on the y-axis and the temperature plotted on the x-axis. The loading plateau stress decreases with increase in the heat treatment temperature. This is because higher the heat treatment temperature, the amount of residual cold work that is retained in the material decreases resulting in an increase of ductility. A certain amount of ductility is required in the material so that it has the ability to absorb some amount of plastic

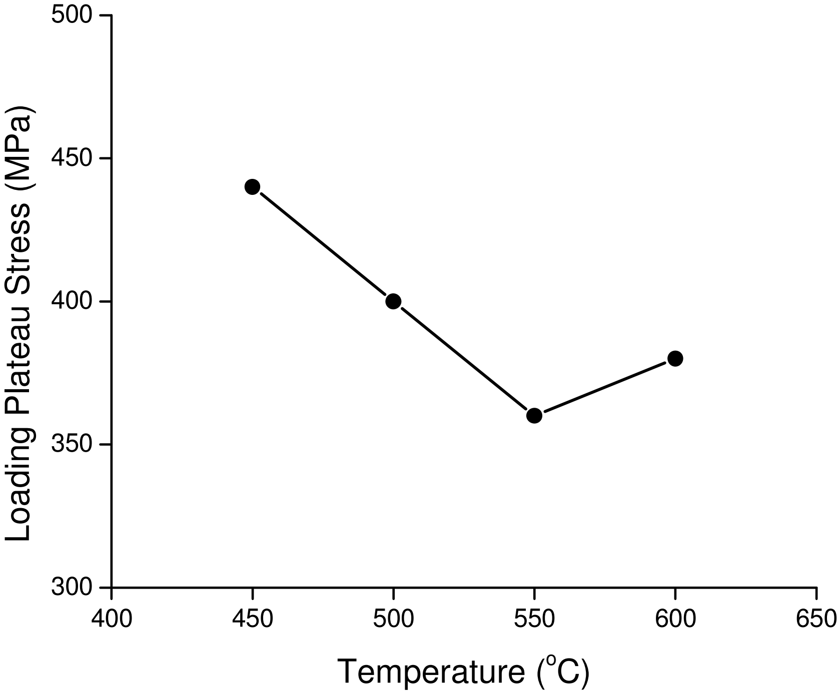

Fig.3.3: Variation of plateau stress with temperature.

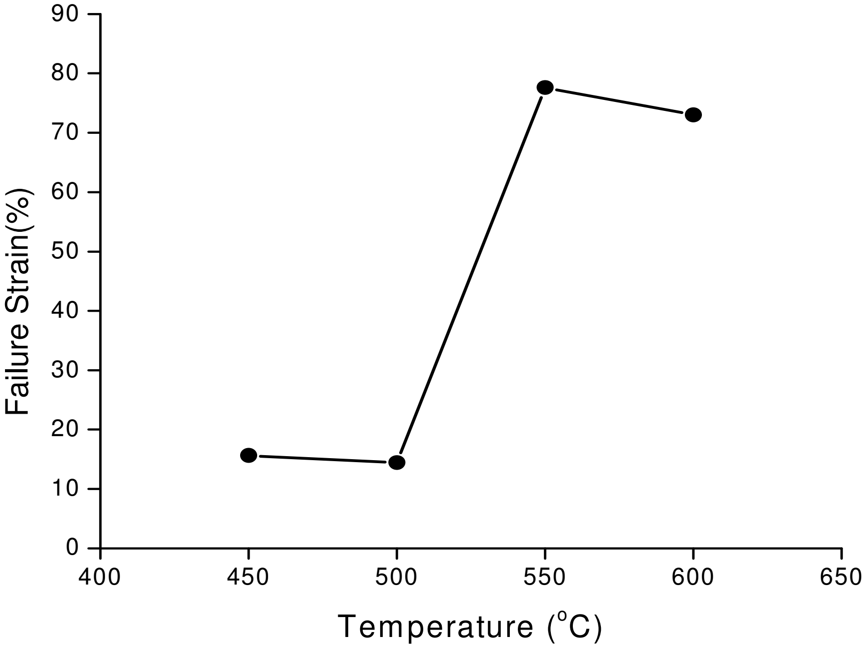

Fig.3.4: Variation of failure strain with temperature.

strain beyond the elastic regime. Fig 3.5 shows the variation of E_{SIM} with temperature. The E_{SIM} is an important parameter in the present context. The higher the elastic modulus of the completely transformed SIM the better is the stiffening effect provided by the SMA element (for the arch and therefore the landing gear sub unit) when the strain levels exceed the SIM plateau which is very likely during the landings. Figs.3.6 and 3.7 deals with the other set of important parameters from the energy dissipation and fatigue considerations.

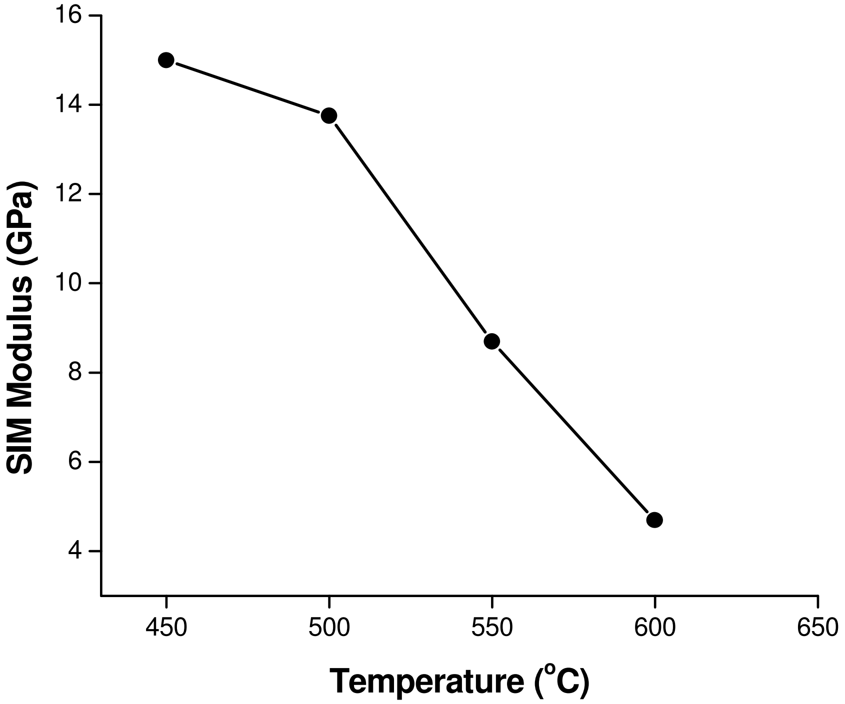

Fig.3.5: Variation of SIM modulus with temperature

These are energy dissipated (E_d) and residual strain ($\in_r$) and the unloading plateau stress. It is clear from the Fig. 3.6 that the E_d increases with increase in heat treatment temperature. In the HT range of 500-600°C the E_d remains more or less constant. The residual strain '$\in_r$' and the unloading plateau stress are the

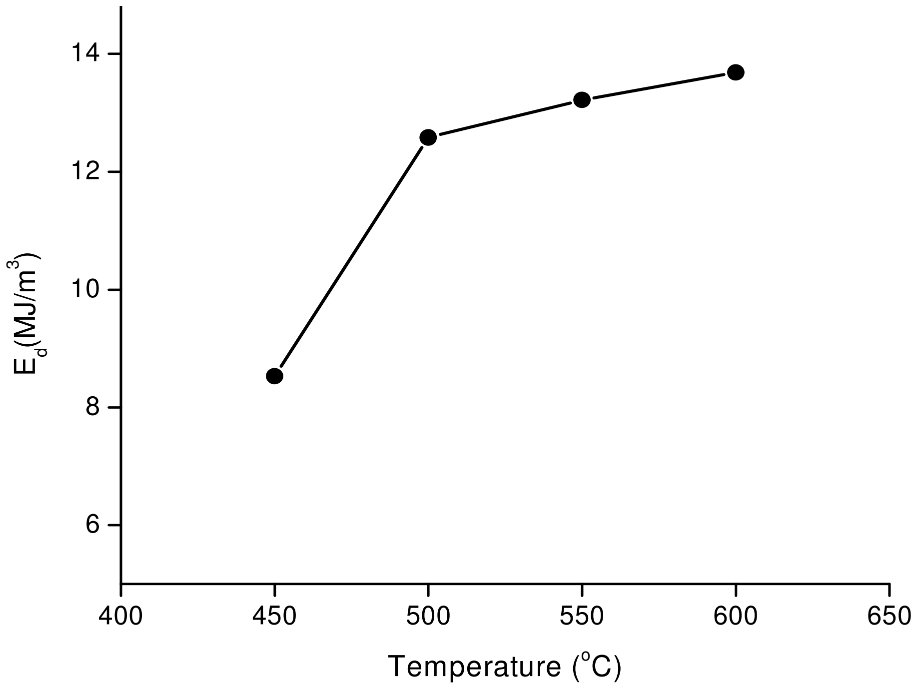

Fig.3.6: Variation of E_d with temperature.

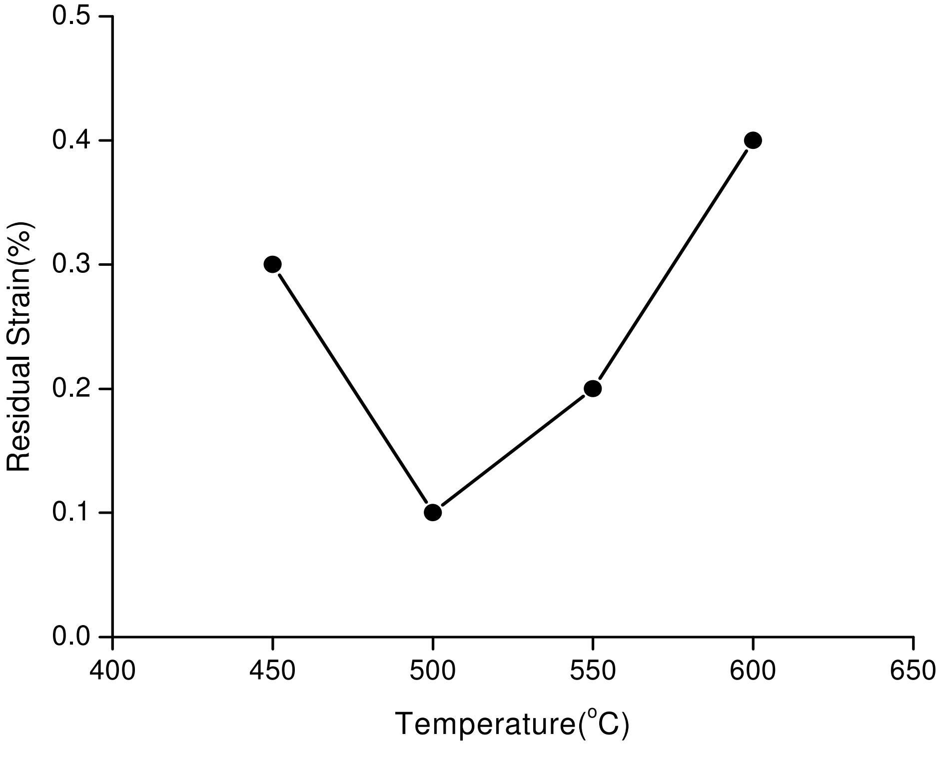

Fig.3.7: Variation of residual strain with temperature.

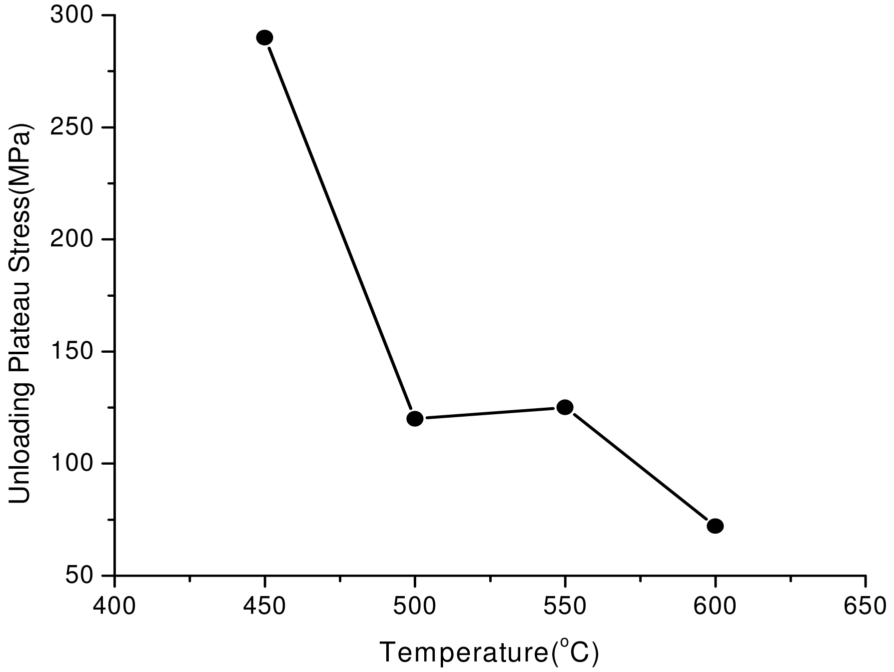

Fig.3.8: Variation of unloading plateau stress with temperature

other parameters to be studied. The residual strain is an indicator of the fatigue life of the SE SMA element, the higher the residual strain, the lower is the fatigue life. Also the higher generation of residual strain during cycling can seriously hamper the functioning of the landing gear which is optimally designed by matching the stiffness of the different elements such as the arch, SE SMA element and the CFRP support structure. The accumulation of residual strain beyond a certain point in the SE SMA will adversely affect the stiffness and energy dissipation characteristics of the landing gear. Fig.3.8 shows the unloading plateau stress variation with temperature which is also important and needs to be above a value of 100 MPa to ensure proper compliance matching with the arch. Therefore it is clear from the foregoing discussion that the energy dissipation has to be high with minimum residual strain and an optimum value of unloading stress. From Fig.3.6 it is clear that for the heat treatment of 500°C the value of E_d is close to the maximum but more importantly the residual strain is minimum for this heat treatment. Taking into account all these factors viz., energy dissipation, loading plateau stress, SIM modulus and residual strain the HT of 500 °C has been chosen. Fig 3.9 shows the results of the DSC tests on the super elastic wire of diameter 0.6 mm which are as follows: M_f = 6.8; M_s = 12.5; A_s = 11.9 and A_f = 17.7 °C. It is clear that the A_f is below the service temperatures which are above 20 °C.

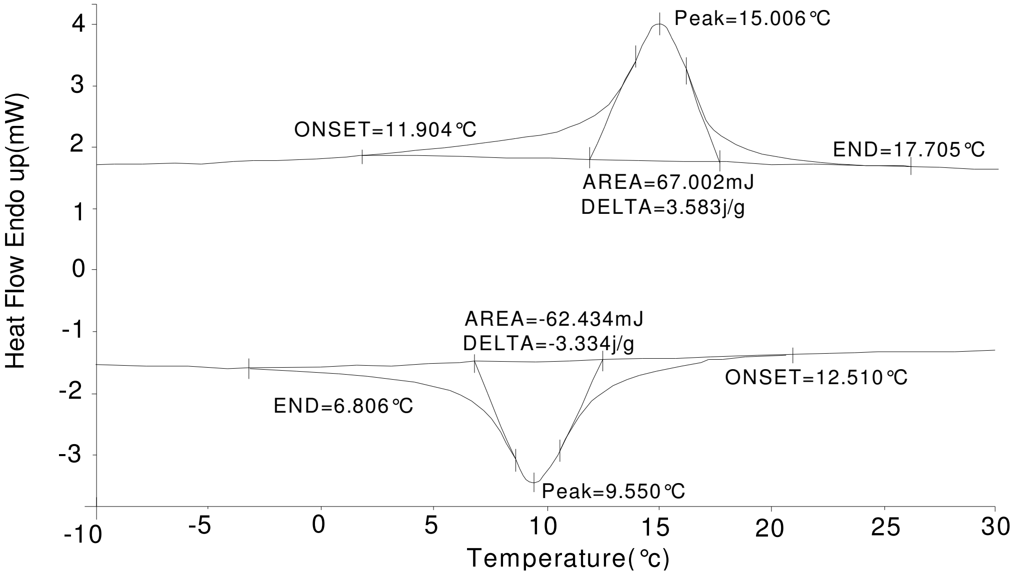

Heating/cooling: 10°C/min

Fig.3.9: DSC Results for the wire heat treated at 500 °C for 15 minutes.

In summary the cold worked wire has been heat treated in the range of 450 - 600 °C. The behavior of the heat treated wire is much different from the cold worked wire. The wires heat treated at different temperatures have been compared in relation to the optimum plateau stresses, energy dissipation and residual strain characteristics.

It is found that the wire heat treated at 500 °C possesses the optimum energy dissipation characteristics for the landing gear application.

The heat treatment imparted to the cold worked wire holds the key to the control of mechanical properties. It is clear that for a given superelastic NiTi SMA wire with a certain degree of cold work the heat treatments in a narrow range of 450 - 600 °C bring about a substantial change in the properties. The increase in ductility of a heat treated wire possessing the energy dissipation character can be as much as eight times compared to a cold worked wire. Similarly in this narrow range of heat treatments the dissipated energy in one complete cycle can vary by as much as 60%. It must be added that the role of grain size on the stress-strain behavior has not been considered in this work.

Chapter 4: Sensory Behavior of NiTi SE SMA

4.1. Introduction:

A ‘smart’ material is defined as one, which mimics or imitates one or more biological functions. These functions can be sensory, actuation or control. The SE SMA is a material system which exhibits not only super elasticity but also possesses sensory characteristics. The manifestation of sensory behavior is simultaneous with the energy dissipation capability (when it undergoes length changes). The sensory behavior is observed when a small electrical signal is passed through the SE SMA element. The change in length is manifest as a change in the electrical quantities by which one can deduce the amount of deformation in the SE SMA. It is necessary to understand the behavior of the sensory characteristics with respect to SIM transformations.

The investigations carried out by Hui Li et al , V. Novak et al, V. Antonucci et al, M. Pozzi et al, J. Uchil et al , G. Airoldi et al and J.L.Jin et al ([32] – [38]) regarding the sensory characteristics have been discussed in chapter 1.

4.2. Sensory Characteristics of SE SMA:

In this work the sensory characteristics i.e. measurement of electrical parameters is evaluated simultaneously with the loading parameters of the wire (with the objective of validating the energy dissipating capability of the smart landing gear). In other words the stress-strain behaviour of the SE SMA element has to be read in conjunction with the resistivity-strain curve. As the SE SMA is loaded a small constant current of about 100mA is simultaneously passed in the SE SMA. It is ensured that this current does not produce any temperature rise in the wire due to resistive heating. This current is far less than the actuating current of about 2000mA, which would be required to actuate a thermal SMA wire of identical diameter. The SE SMA element is placed in such a way that when the landing gear impacts the ground the SE SMA element is forced into a tensile mode of deformation and in the process undergoes substantial change in length.

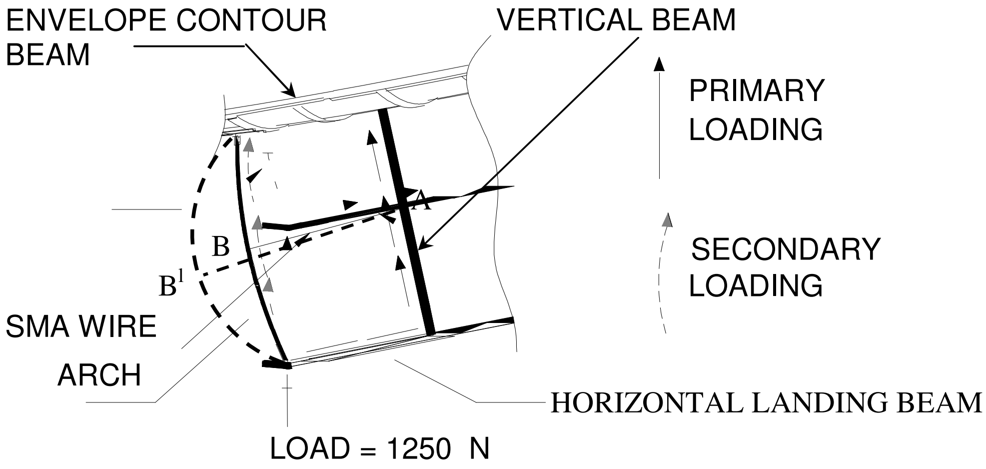

———— Arch shape before impact [SMA length (AB) ≈ 1000 mm]

- - - - - - - Arch at the time of impact [SMA length (AB^{l}) ≈1060 mm]

Fig.4.1: The length of the SMA in the landing gear before and during impact

Fig.4.1 shows the configuration of SE SMA element before and after the landing gear impacts the ground. The length AB ≈ 1000 mm corresponds to the position before impact and the length AB^1 ≈ 1060 mm corresponds to the position after impact. The co-relation between the stress-strain curve and the resistivity –strain curve is proposed to be established by the following hypothesis. Fig.4.2 (a) shows that the stress-strain curve – OABCDEFO and Fig.4.2 (b) shows the resistivity strain curve – PQRSTUVP, which are to be read in conjunction with each other. The test temperature is 27°C and the strain rate is 2 %/min.

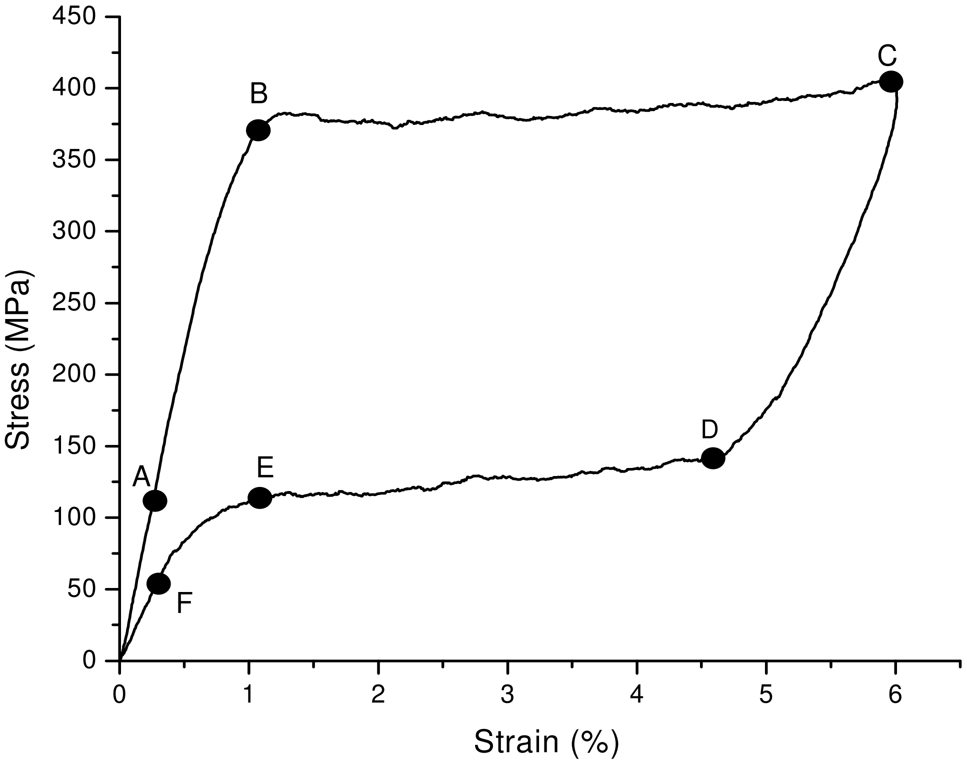

Fig.4.2 (a): Stress-strain curve for loading and unloading at 6% strain amplitude

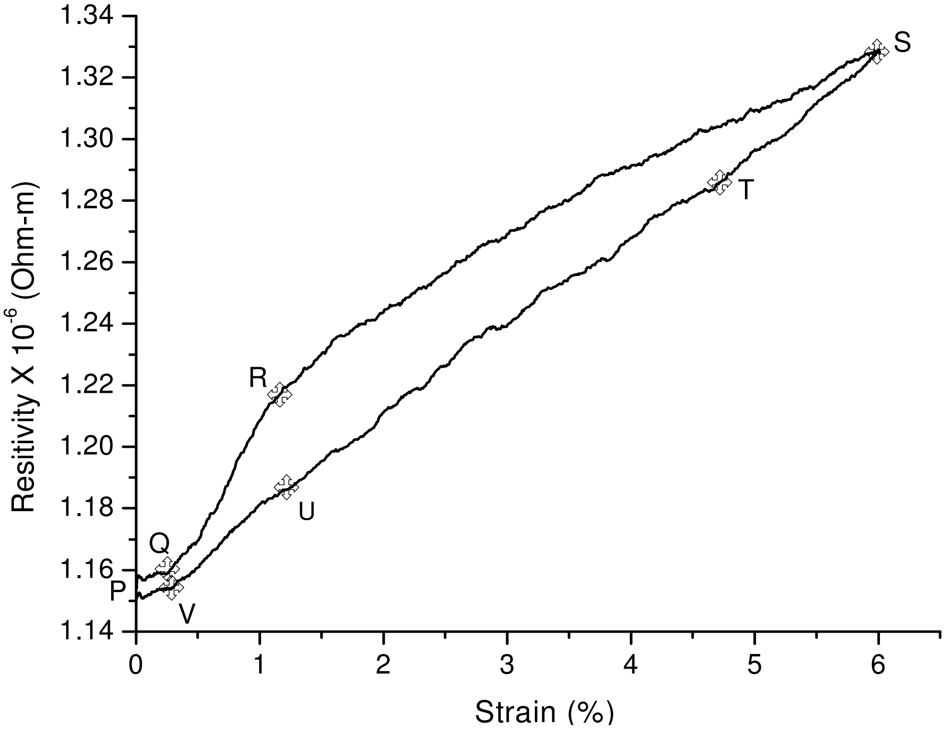

Fig.4.2 (b): Resistivity-strain curve corresponding to loading and unloading in fig.4.2 (a).

The points O, A, B, C, D, E & F on the stress-strain curve Fig.4.2 (a) correspond to the points P, Q, R, S, T, U& V on the resistivity strain curve Fig.4.2 (b). Point 'O' on the stress-strain curve represents the austenite condition at zero stress. The corresponding point 'P' in Fig.4.2 (b) has a unique value of resistivity. Although the resistivity curve in the Fig. 4.2 (b) does not terminate exactly at 'P' in the return path for the purpose of explaining the bi-functionality the difference is ignored. It is important to note that the segment 'PQ' is nearly flat in the Fig.4.2(b) though there is an increase of stress in the corresponding segment 'OA' in the Fig.4.2(a). Novak et al [2] and Sittner et al [3] have reported similar results. This is probably because of the presence of some martensite or other phases being present in the material at low stresses. This matter needs further investigation and is outside the purview of this thesis.

Let us consider the segment 'AB' on the loading part of the stress-strain curve. The corresponding segment 'QR' on the resistivity curve has a constant slope and indicates an increase of the austenite resistivity. The increase in resistivity is purely due to the change in length of the austenite in the segment 'AB'. The plateau region 'BC' on the stress-strain curve corresponds to the region 'RS' on the resistivity strain curve. The segment 'RS' is assumed to have a constant slope whose value is different from the slope of the segment 'QR'. For simplicity it is assumed that the SIM fraction $\xi = 0$ (point 'B' in Fig.4.2 (a) and point 'R' in Fig.4.2 (b)) and $\xi = 1$ at the points C & S respectively.

Figs.4.3 (a) & (b) show the stress-strain (OABC) and the resistivity-strain (PQRS) curves only for the loading part. The load and deflection analysis of the landing gear is also confined only to the loading segment. In Fig.4.3 (b) ‘QR’ represents the change in resistivity corresponding to the elastic deformation of only the austenite phase (i.e. segment ‘AB’ of the stress-strain curve). Assuming the material to remain in austenite condition till the strain of 6% (i.e. strain corresponding to end of SIM segment) the extrapolated value of the resistivity at the end of 6% strain is obtained by extending the line ‘QR’ to meet at point ‘Z’. ‘ZY’ represents the change in resistivity (assuming the material to remain in austenite) for the complete strain range of 6%. ‘ZS’ represents the change of resistivity solely due to the SIM plateau (i.e for ξ changing from 0 to 1). In other words the SIM has resulted in changing the absolute value of the resistivity (at the point ‘C’ on the stress-strain curve) by an amount equal to ‘ZS’. ‘SY’ (ZY-ZS) represents the measured net change in resistivity for the complete loading process ‘OABC’ upto the 6% strain corresponding to the point ‘C’. It is clear that every point on the loading part of the stress-strain curve ‘ABC’ has a unique value of resistivity on the resistivity-strain curve ‘QRS’. In this way the resistivity variations can be interpreted as strain variations during loading. The variation of resistivity with strain is almost linear both in the austenite and SIM segments. The description of the sensory behavior is confined to the loading part of the stress-strain and resistivity-strain curves only. Similar argument can be extended to the unloading curve. It is important to note that the unloading segment on the stress-strain curve corresponds to a flat segment ‘VP’ on the resistivity strain curve of fig 4.2(b). This again points to the fact that in the region ‘FO’ of the

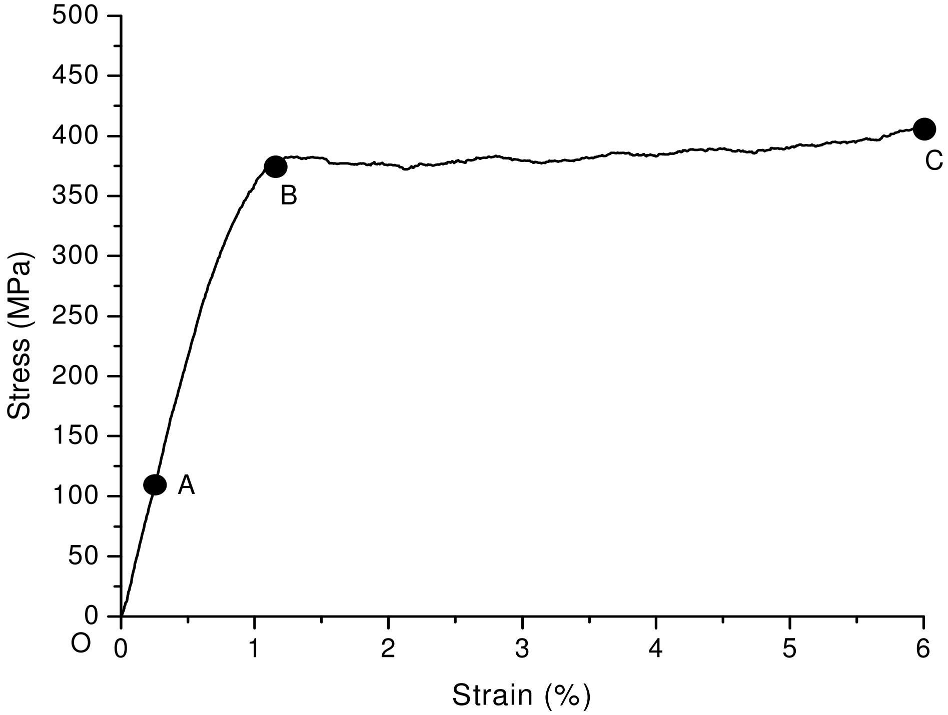

Fig.4.3 (a): Stress-strain curve for loading upto 6% strain amplitude.

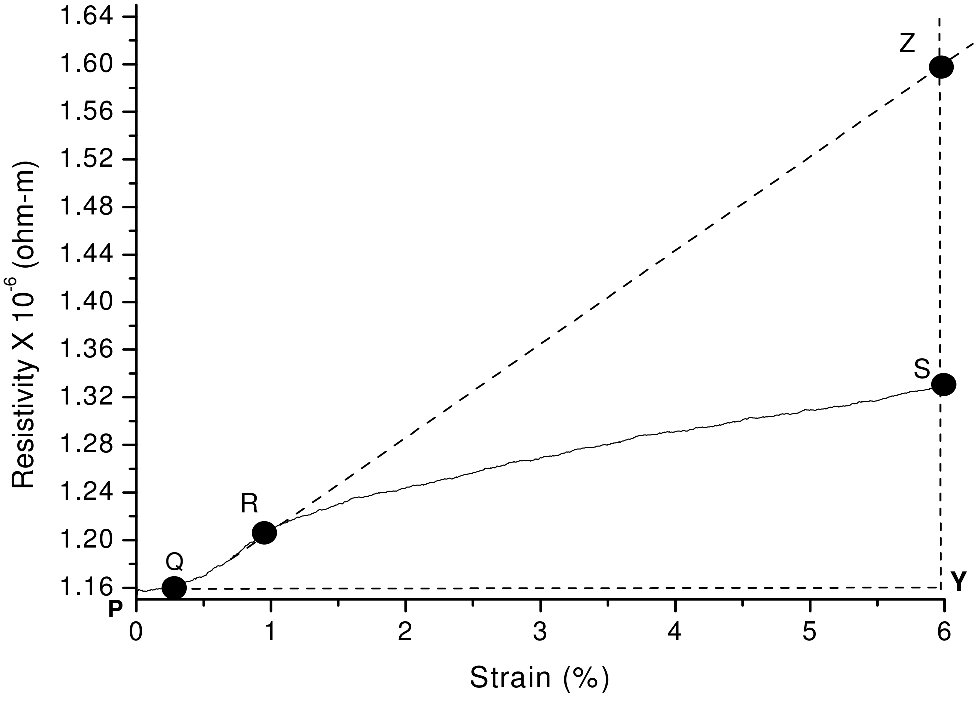

Fig.4.3 (b): The resistivity variation 'ZS' solely due to SIM.

unloading curve (like in 'OA' of the loading curve) where the stresses are low the material may not be in the fully austenite condition.

The resistivity (ρ) is calculated from equation 2.2 of the form ρ = R a/l where 'a' is the area of the cross section of the SMA element, 'R' is the resistance and 'l' is the length. Since large strains of the order of 6% are measured the continuous changes in the parameters 'a' and 'l' is taken into account while computing resistivity. It is assumed that the product of 'a' x 'l' = _V_ where '_V_' is the volume is a constant. For the resistivity experiments described in this work the length of wire samples chosen were 500 to 650 mm respectively. The larger lengths were chosen to minimize the adverse effects of noise in the measurements. Also the lengths are close to the actual length of 1000 mm used in the smart landing gear. Due to the limitation of the test set up it was not possible to increase the length of the test samples beyond 650 mm. At the maximum length of 650 mm the testing was done at two different currents. It is clear from table 1 that resistivity values are largely independent of the current and length. The values of austenite maximum are obtained by extrapolating the segment 'QR' to 6 % strain as shown in figure 4.3. The small variations in the resistivity values for different lengths are attributed to the small changes in voltage owing to the length changes.

Table 1: Resistivity values for different lengths and currents

SL. No.	Length (mm)	Current (mA)	Strain rate (%/min)	Resistivity x10^{-6} (Ohm-m) (at 6% strain)	
				Austenite Max.	SIM Max.
1	500	100	2	1.59	1.33
2	650	100	2	1.69	1.40
3	650	70	2	1.69	1.44

In summary a small constant current has been passed in the SE SMA and the voltage has been measured across the SMA element as it undergoes elastic strain of the order of 6%. The measurement of voltage is simultaneous with the straining of the SMA element as it dissipates energy. In the SIM region the variation of resistivity computed from the measured voltage is linear with the strain in the SMA element.

The sensory information is used only to validate the design. The simultaneous use of SE SMA as a sensor as it deforms and dissipates energy is done in the following manner. A small current (100mA) is passed through the super elastic SMA. The change in length of the SMA is manifest as a change in voltage across SMA, measured in millivolts, when a small constant current of the order of about 100 mA is passed through the SE wire. The voltage signal is acquired using the necessary hardware interface, which is part of the blimp electronic circuitry. The voltage is converted to a frequency signal using a voltage to frequency converter mounted on the blimp. At the ground station the frequency signal is received and re-converted to a voltage signal. Fig.4.4 shows the electrical resistivity (calculated based on the acquired voltage change, area and length across SMA) vs. strain relationship during loading. The resistivity vs. strain curve OAB is having two slopes. The first segment OA represents the elastic increase in length of austenite phase only. The second segment AB (super elastic) represents the change of phase in the plateau region of the stress-strain curve. Therefore, the changes in resistivity are far more pronounced in the segment AB. It is clear that the change of phase (measured as a change in resistivity) is accompanied by a simultaneous change in length. The resistivity vs. strain data shown in Fig. 4.4 is only for the loading curve. For example, at point O, the SMA length is 1000 mm. At points A & B the SMA has undergone a change in length of 15 mm and 60 mm respectively.

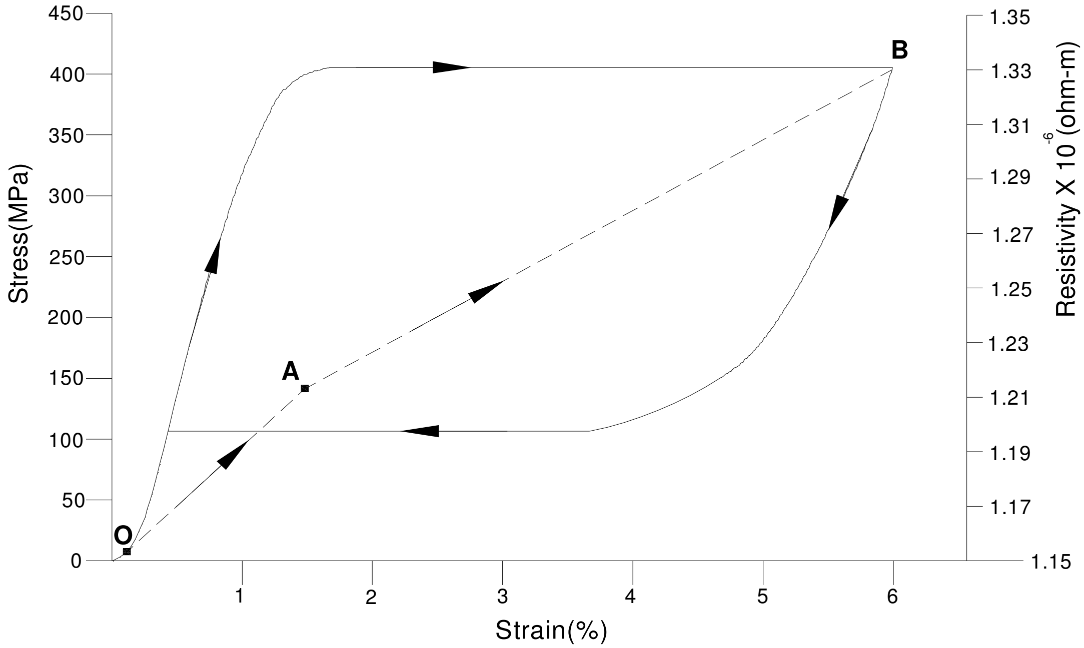

Fig.4.4: Stress vs. strain and resistivity vs strain for SE wire.

Every point on the curve OAB has a unique value of resistivity and SMA length. Thus for a given value of voltage read at the ground station there is a corresponding value of resistivity and SMA length. For a given SMA length the corresponding value of the vertical deflections can be known. The change in length of the SMA is a clear indicator of the energy absorbed by the SMA element and the deformation characteristics of the arch and therefore that of the landing gear also. Thus, this information is a useful sensory feedback (only to validate and if necessary) to modify the design of the smart landing gear. In summary the sensory characteristics of the SE SMA as it dissipates energy has been brought out. Thus the bi-functionality of the smart material which in this case is the SE SMA has been established.

Chapter 5: Strain Rate Effects

5.1: Introduction:

This chapter details the investigations pertaining to the effect of strain rate on tensile and energy absorbing/dissipating properties of SE NiTi thin wires. These are relevant to the use of Ni Ti SE SMAs for energy dissipation applications. An attempt to gain the understanding of the interplay of the ductile behavior, temperature and strain rate effects and energy storage during both tensile testing and cycling has been made. It is important that for the proper design of super elastic SMA based devices such a study should address the following: a) Comparison of energy storage capacity of NiTi SMAs vis-a-vis conventional materials. b) Effect of temperature and strain rate on ductility. c) Influence of strain rate on SIM plateau and energy dissipation. d) The strain rates at which the energy dissipation is optimum and e) Cyclic loading effects. The wires are in austenite condition at room temperature and above. The studies relating to the effects of strain rate on properties of NiTi elements is the subject of current research and have been carried out by Kafka et al, Des Roches , Dolce et al, Tobushi et al , Lin et al, Nasser et al, Humbeeck et al, Ahluwalia et al, Raghavendra et al and Aaltio et al ([39] – [49]). This has been discussed in chapter 1. The interplay of the various issues mentioned above is dealt with. The strain rates of interest (covering a wide range of applications) range from the 'static' tension tests using hydraulic or screw driven machines (i.e., 10^{-5} to 10^{-1}/s) to the 'dynamic' tests (i.e., 10^{-1} to 10^{2}/s or even higher). In this study taking into account the type of machine and the end grips available the strain rates that are studied are in the range of 3.3×10^{-5} to 0.13/sec. For the 100mm length these strain rates translate to 0.2 to 800% /min. For the 30 mm length the range of strain rate investigated is $3.3X10^{-5}$ to $3X10^{-2}$/sec (i.e., 0.2 to 180 %/min). Lin et al [48] & Tobushi et al [49] have used lengths around 30 mm for a comparable diameter of SE wires for strain rate studies. Before going further into the discussions on the strain rates, it is necessary to understand the issues associated with displacement measurements for thin wires.

5.2: Issues in displacement measurements:

Like in the case of conventional tensile testing in the case of Ni Ti thin wires too small differences in the values of the displacements (this in turn results in different values of the residual plastic strain) measured using an extensometer and crosshead have been reported [48]. When the displacement is measured from the crosshead, some slippage may occur in the gripped part of the specimen, influencing the residual plastic strain slightly. The slippage is independent of the gage length. Therefore the larger the gage length the smaller is the percentage of residual plastic strain (in proportion to the total strain) due to the slippage at the grips. In the present work, the displacement has been measured using a crosshead. In view of this it was first decided to choose a gage length of 100 mm so that the grip effects become negligible. The strain rate studies for 100 mm gage length were conducted for the range of 0.2 to 800%/min. These tests provide good insight into the behaviour for the range of strain rates stated above for tensile tests up to failure. However, the drawback with the choice of 100 mm gage length is that for the cyclic tests the wire experienced buckling which adversely influenced the unloading stress and the residual plastic strain parameters. In view of this for the 100 mm gage length only the results of those tests, which do not involve cyclic loading are presented. For the cyclic studies a smaller gage length of 30 mm was chosen and the range of strain rates studied is between 0.2 to 180%/min. For completeness of experimental data and proper co-relation (of various parameters) both tensile tests up to failure and cyclic tests have been conducted on the 30 mm gage length wire. The results of the 100 mm gage length are presented first and then the 30 mm gage length is presented. The tensile test results for 100 mm length are not exactly identical with those for the 30 mm gage length because of the grip and other scale effects but they are very similar. The interplay of the ductile behavior, temperature, strain rate effects, energy storage and cycling is addressed in the subsequent sections.

5.3. Comparison of Energy Storage:

In order to evaluate the energy storage related characteristics of NiTi SMAs it is necessary to compare the NiTi behavior with a conventional steel helical spring and an aluminum tensile testing specimen. Table.1.1 shows that the NiTi SMA has very high specific energy storage capacity in the elastic region compared to both helical steel spring and aluminum flat specimen. This is mainly because of the super elasticity of NiTi SE SMA. Table 1.2 brings out the energy storage comparison in relation to conventional materials such as spring steel, structural steel and aluminium. The energy absorption in the elastic region for a unit volume is as much as 10 times compared to the conventional spring steel, 15 times that of aluminium and about 30 times that of structural steels. Fig.1.2 shows the comparison of the stiffness characteristics of the 0.6 mm diameter NiTi super elastic SMA behavior with that of a helical tensile spring (wire dia=2.5 mm, coil dia=12 mm and length=100mm). It is clear that the NiTi SMA has a far higher energy dissipation characteristic up to about 6% strain. The NiTi SMA stiffness (deflection for a unit load) increases with increasing deformation beyond the 6% strain. This stiffness increase enhances the stiffness of the landing gear device in which it is used similar to the springs.

5.4 Ductile Behaviour of SE SMAs:

The NiTi SMAs are inherently ductile materials. The ductile behavior is present in both the cold worked and heat-treated conditions. The material considered in this study is fully martensite at temperatures less than 6.8°C. It is austenite above 18°C.

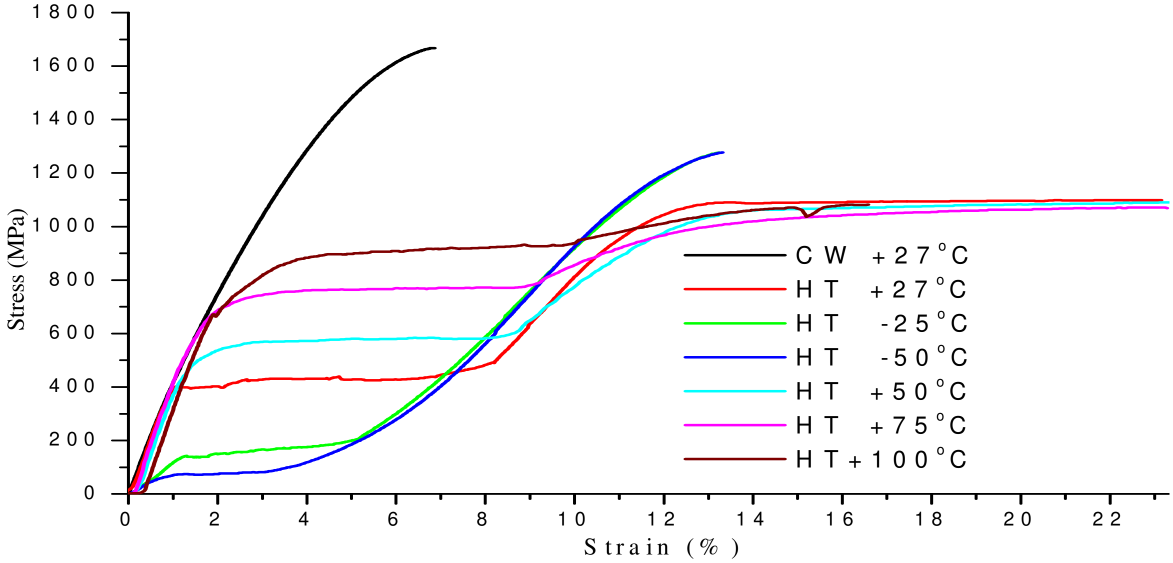

Fig.5.1: Stress-strain plots upto failure for the temperature range of -50 to 100°C.

Fig.5.1 shows the stress-strain plots up to failure at different temps. from -50 to +100°C for a constant strain rate of $3.3X10^{-4}$/sec (2%/min). At –50 and –25°C the material is in the martensite condition.The SIM segments of the loading curves in thetemperature range above 18 °C (27 – 100 °C) shift upwards with increasing temperature

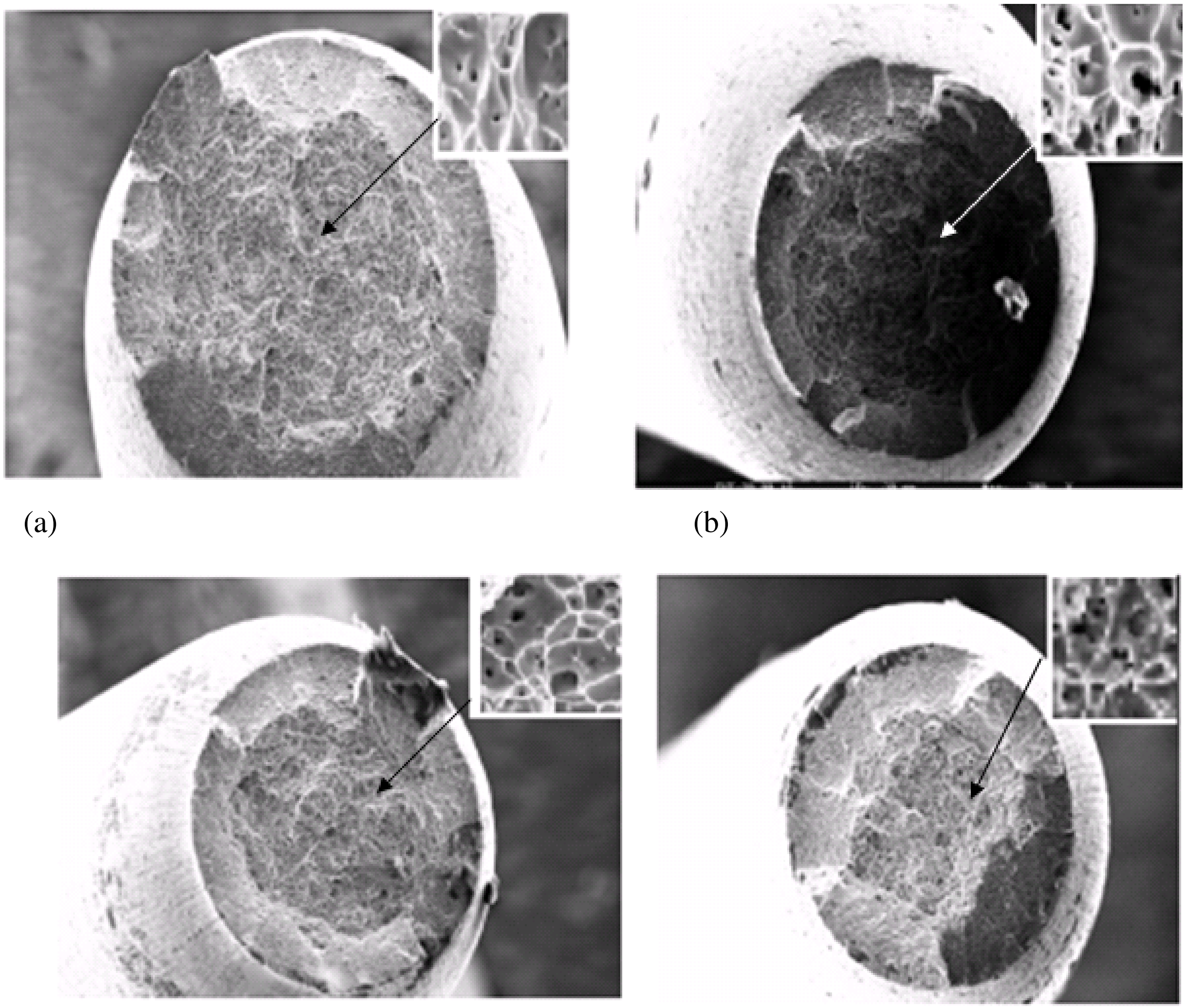

(a) (b)

(c) (d)

Fig.5.2: (a) Ni-Ti SE (cold worked) fractured surface at 27 °C, strain rate = 2%/min. (b) Ni-Ti SE (heat treated) fractured surface at −50 °C, strain rate = 2%/min. (c) Ni-Ti SE (heat treated) fractured surface at 27 °C, strain rate = 2%/min. (d) Ni-Ti SE (heat treated) fractured surface at 100 °C, strain rate = 2%/min. The magnified (3000 X) portions of the central regions are shown in the right top corner.

and are almost parallel to each other (identical slope). The upward shifting of the onset of transformation is in accordance with the familiar Clausius-Clapeyron relationship ($d\sigma/dT \sim 6$; for this material). The fracture surfaces of specimens tested up to failure at

-50ºC & at room temperature (27ºC) at a strain rate of $3.3X10^{-4}$/sec (2%/min) and the fracture surfaces of the material that was tested at a very high strain rate of $1.3X10^{-1}$/sec (800%/min) at room temperature were observed under a scanning electron microscope (SEM). Figs.5.2 (a) to 5.2 (d) show the magnified (3000X) portion of the central region on the right top. Both below M_f & above A_f the fracture surfaces of the heat-treated samples (for tests up to failure) exhibited a typical cup and cone fracture, which is characteristic of materials exhibiting ductility. Even the fracture surface of the cold worked wire exhibited a cup and cone fracture. In addition, at the high strain rate

Table.5.1: Fractography result

Material condition	Test temperature (ºC)	Strain rate (%/min)	Fractography result
Cold worked	27	2	Cup and cone fracture
Heat treated	27	0.2	Cup and cone fracture
Heat treated	27	2	Cup and cone fracture
Heat treated	27	800	Cup and cone fracture
Heat treated	-50	2	Cup and cone fracture
Heat treated	100	2	Cup and cone fracture

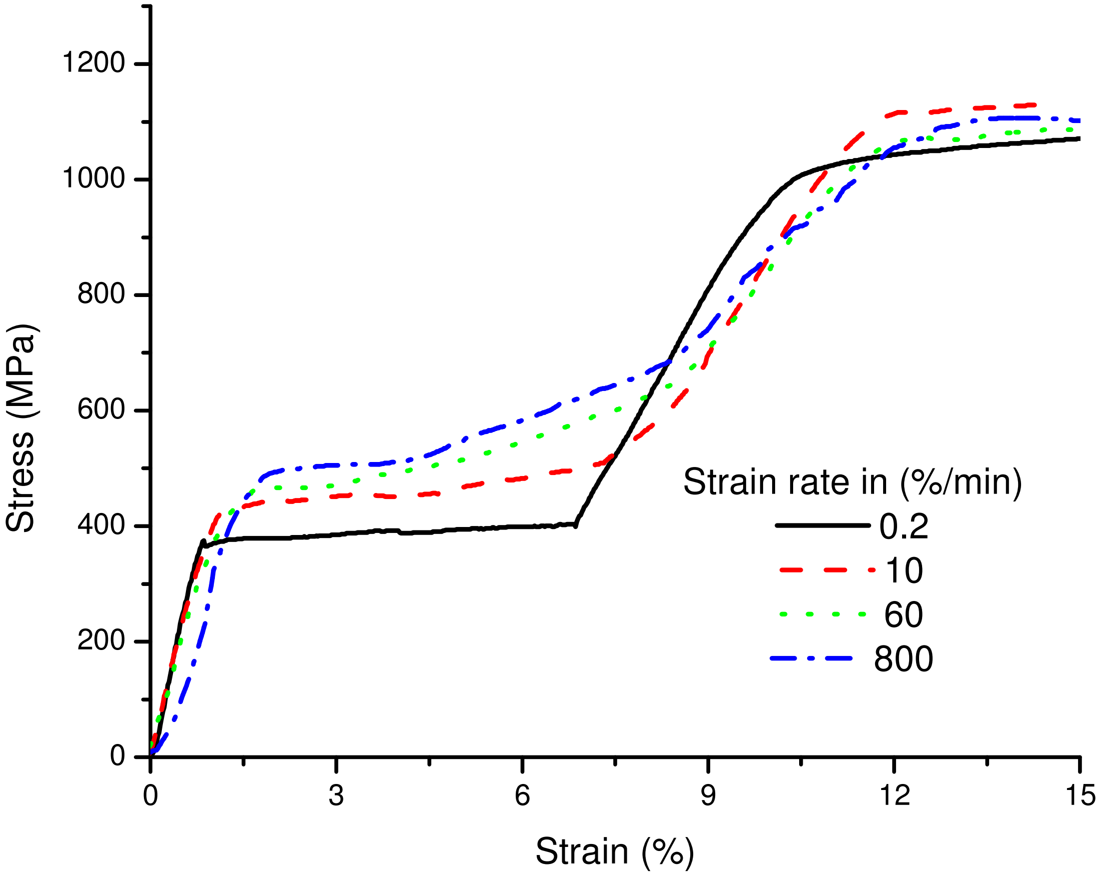

Fig.5.3: Relationship between stress & strain(at 27° C)for the tensile testing upto failure.

(1.3X10^{-1}/sec (800%/min)) also, the material exhibited a cup and cone fracture when it was tensile loaded up to failure. Thus, all the specimens showed cup and cone fracture with ductility. The summary of these tests is given in Table.5.1. Fig.5.3 shows the relationship between stress and strain for the tensile testing up to failure. It is seen that σ_l is at a level of less than 400 MPa for the strain rate value of less than 3.3X10^{-5} /sec (0.2%/min) and about 500MPa for the strain rates of 1.3X10^{-1}/sec (800%/min). The corresponding change in the σ_{es} is from 400 to 600 MPa. The value of 'σ_l' is close to the typical values (400 – 500 MPa) reported in literature [3, 4]. Further it is seen that the slope, n_m, of the SIM plateau region i.e., between the points σ_l and σ_{es} is nearly flat for a strain rate below 8.3X10^{-4}/sec. For strain rates between 8.3X10^{-4} to 3.3X10^{-3}/sec (i.e., 5 to 20%/min) n_m varies between 0.1 to 0.2. For strain rates above 3.3X10^{-3} /sec (20%/min) n_m is in the range 0.2 to 0.25. The summary of these slopes is given in Table.5.2. It is further seen that there is a distinct σ_{es} only up till a strain rate of 1.6X10^{-3}/sec (10%/min). Above these strain rates the σ_{es} is not conspicuous as the SIM plateau segment and elastic region of the stress induced martensite merge. There is a sharp inflection point at lower strain rates and a more gradual change of slope as the strain rate increases. At the highest strain rate tested (1.3X10^{-1}/sec (800%/min)) the inflection point occurs at less than 4% strain compared to the nearly 7% for the lowest strain rate (3.3X10^{-5}/sec (0.2%/min)) as shown in Fig.5.3. The SIM segment of the loading curve translates upwards with increase in strain rates. The upward translation of the SIM formation and elastically deformed SIM has a direct bearing on the stresses at different strains in the elastic region.

Table.5.2: Slope of SIM plateau region.

Sl no	Strain rate range (%/min)	Slope (n_m)
1	0.2 – 5	0
2	5 – 20	0.1 – 0.2
3	> 20	0.2 - 0.25

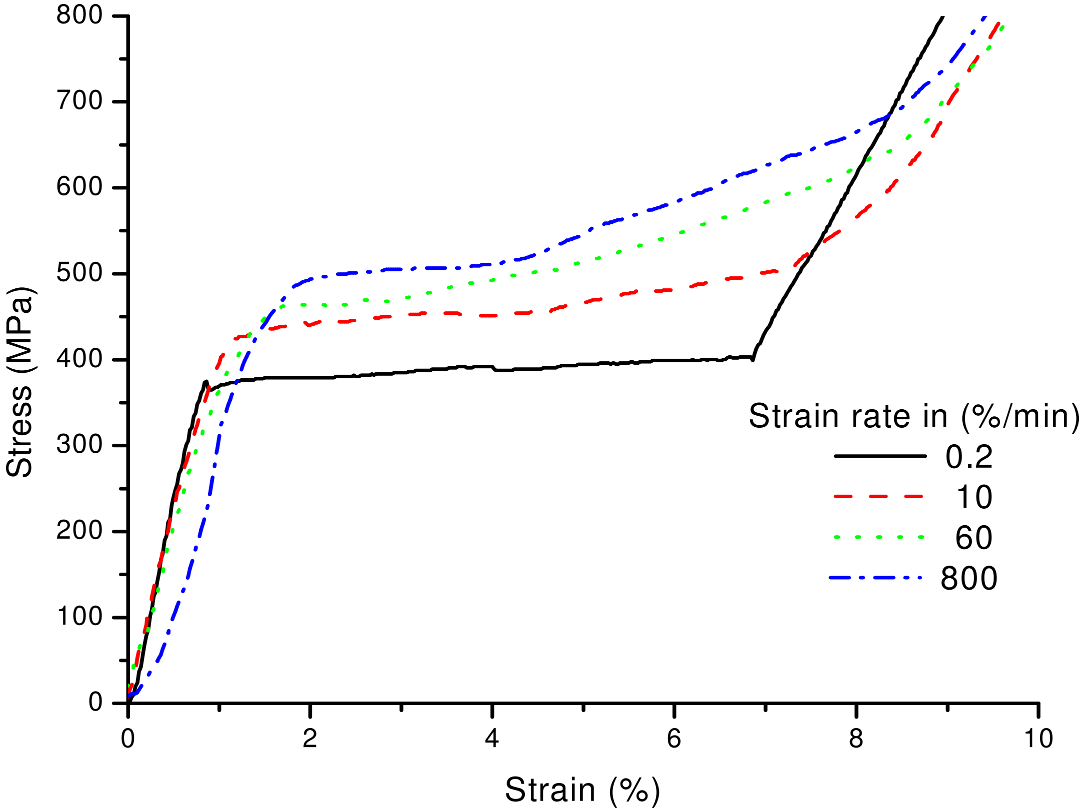

Fig.5.4: Enlarged view of the stress-strain (at 27° C) plot for the tensile testing upto failure.

Fig.5.4 is an enlarged view of the stress-strain plot of Fig.5.3 up to 9% strain. The loading curves up to $1.6X10^{-3}$/sec (10%/min) have three elastic segments during loading. On carefully examining the loading curve at $1.3X10^{-1}$/sec (800%/min) it is seen that there are in fact four "elastic" segments instead of three during loading. Similar behavior is also observed for a strain rate $5.0X10^{-2}$/sec (300%/min). There is an intermediate region between the SIM segment and the "elastically deformed SIM" segment with an intermediary slope. This segment represents a dual phenomena i.e. both SIM formation and elastically deformed SIM co-exist. This segment is seen between the 4% and 9% strain for the strain rate of $1.3X10^{-1}$/sec (800%/min). It is obvious that the SIM formation is not able to cope with the externally imposed strain rates above 5X10^{-2}/sec. Therefore, even before the SIM formation is complete the elastic deformation of the already formed SIM commences which results in the overlapping of the SIM formation and elastic deformation of SIM. Fig.5.5 is a semi-log plot of stress vs. strain rate which shows that the stress at 2,4,6% strain increases with increasing strain rate up to 1.6X10^{-2}/sec (100%/min) beyond which the strain rate has very little effect on the stress.

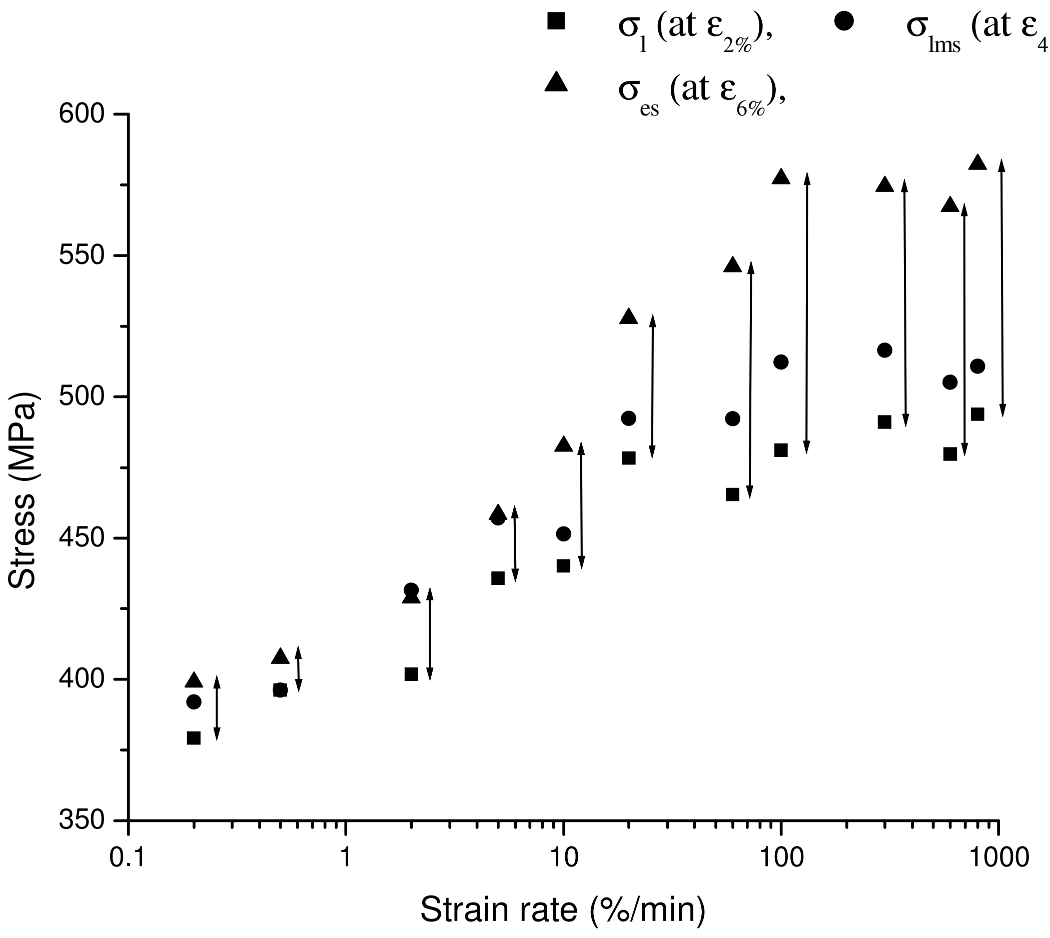

Fig.5.5: Semi-log plot of stress vs strain rate.

5.5. Tensile behavior, fractography & cyclic testing for the 30 mm length wire:

Similar results were obtained from the tensile and fractography tests for the 30 mm length wire as for the 100 mm length wire. It is clear from Table.5.1 that the material undergoes ductile fracture both at low and high strain rates as well as low and high temperatures. Fig.5.6 and Fig.5.7 shows the fractography results obtained from the SEM microscope indicating the gross features of the fracture surface which indicates a cup and cone fracture.

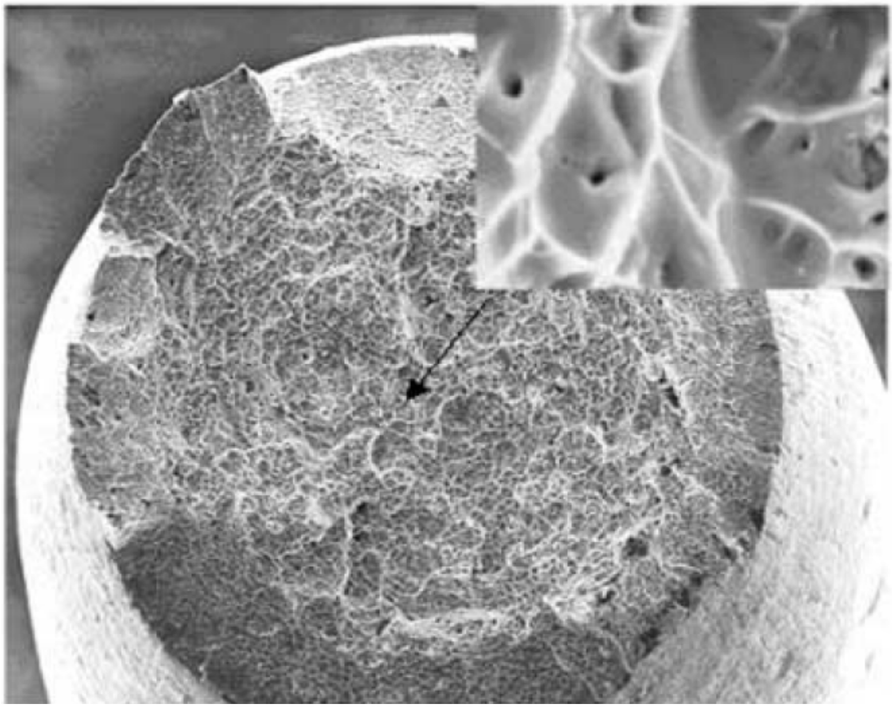

Fig.5.6: NiTi SE (Cold worked) fractured surface at 27 °C, strain rate = 2 %/min. The magnified (3000 X) portion of the central region is shown in the right top corner.

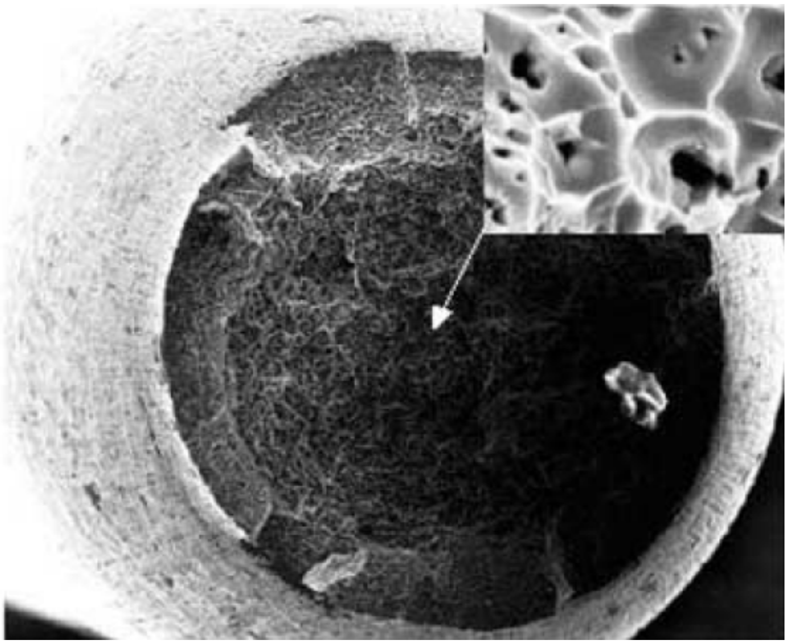

Fig.5.7: NiTi SE (Heat Treated) fractured surface at –50 °C,strain rate = 2 %/min. The magnified (3000 X) portion of the central region is shown in the right top corner.

The maximum strain rate for the 30 mm length wire was limited to 180%/min. For the SIM formation also results similar to the 100 mm length were obtained. Fig.5.8 shows the semi-log plot of stress vs. strain rate wherein the stresses at 2,4,6% strain increases with increasing strain rate up to 60 %/min beyond which the strain rate has very little effect on the stress.

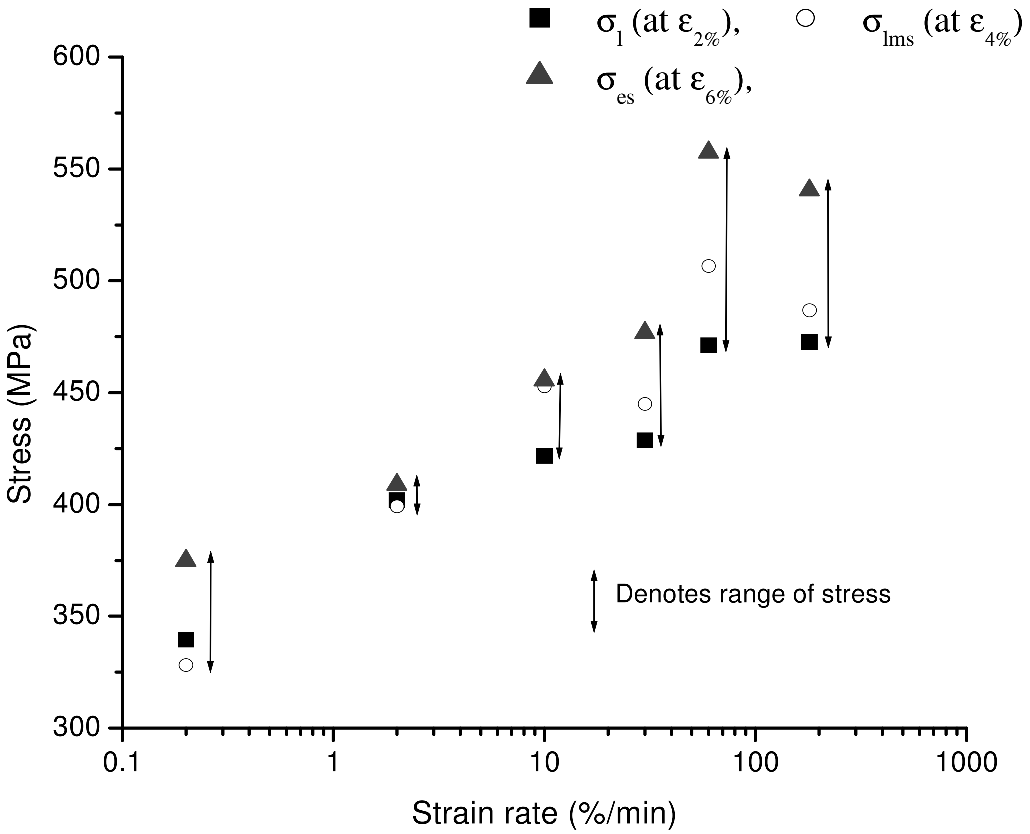

Fig.5.8: Stress vs. strain rate semi- log plot.

For the 30 mm wire cyclic tests were conducted in addition to the tensile tests up to failure. Before studying the effect of strain rate on energy dissipation the maximum cyclic strain amplitude at which the energy dissipation is maximum with minimum permanent plastic strain is found.

Table.5.3: Energy dissipated for varying strain amplitudes

S.No	Strain amplitude (%)	Energy dissipated (E_d) (MJ/m^3)	Residual strain (ε_r) (%)
1	2	2.66	0.07
2	4	6.91	0.03
3	6	15.65	0.13
4	8	24.36	0.11
5	10	26.00	0.80

Table.5.3 summarizes the results of the full cycle test for the strain rate of 0.6 %/min (2mm/min) at different cyclic strain amplitudes viz; 2, 4, 6, 8 & 10% respectively for the 30 mm length wire. It is clear that the energy dissipated increases with increasing strain amplitude. The E_d is high in the strain amplitude range of 4 to 8%. It is seen that the residual strain is within 0.2% for strain amplitudes up to 8%. Since the residual strain reaches a high value beyond the 8% strain amplitude the cyclic test is limited to 8% cyclic amplitude. Since large SE strain amplitude is generally desirable in engineering applications the cyclic tests for different strain rates is done for 6 and 8% strain amplitude. The full cycle testing at 6 and 8% strain amplitude was carried out for different strain rates from 0.2 to 180%/min (i.e., 0.06 to 54mm/min). It is seen from Figs.5.9 & 5.10 that as the strain rate increases the hysteresis loops narrow and translate upwards. The mean point shifts to the higher stress, higher strain regime (with

increase in strain rates). As already mentioned at higher strain rates, there is a overlapping of the SIM formation and elastic deformation of SIM.

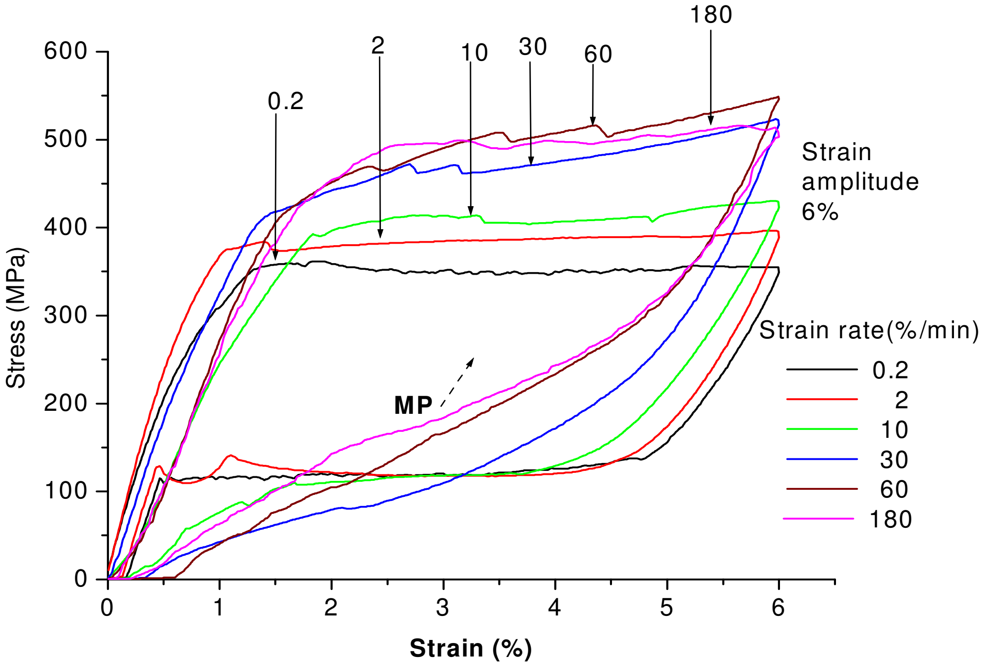

Fig.5.9: Stress vs strain (at 27° C) for different strain rates at a strain amplitude of 6 %.

Since this region already contains a substantial amount of elastically deformed SIM it has a direct effect on reducing the hysteresis loop and therefore the energy absorbing capability during the cycling at 6% and 8% strain respectively as can be seen in Figs.5.9 & 5.10. It has been reported [11] that the increase in stress levels and narrowing of the hysteresis loop with increase of strain rate is due to the self-heating of specimen. The temperature increase is ascribed to the latent heat of transformation. The role of stress relaxation upon formation of stress induced martensite needs to be studied. Therefore, in our view additional experiments are needed to ascertain this on thin wires. While the austenite elastic deformation segment of the loading curve starting from zero stress and strain does not show much variation, the SIM segment of the loading curve translates upwards with increasing strain rates as already stated. The unloading curve has two distinct segments representing unloading of martensite phase and re-transformation of SIM to austenite. These two segments are distinct up to a strain rate of 10%/min. Beyond this strain rate, the two segments of the curve start merging and at the highest strain rate (180 %/min (i.e. 54 mm/min)) tested, the difference in the slopes of the two segments is minimum. The strain rate has a direct on the unloading process and in turn on the energy dissipation capacity.

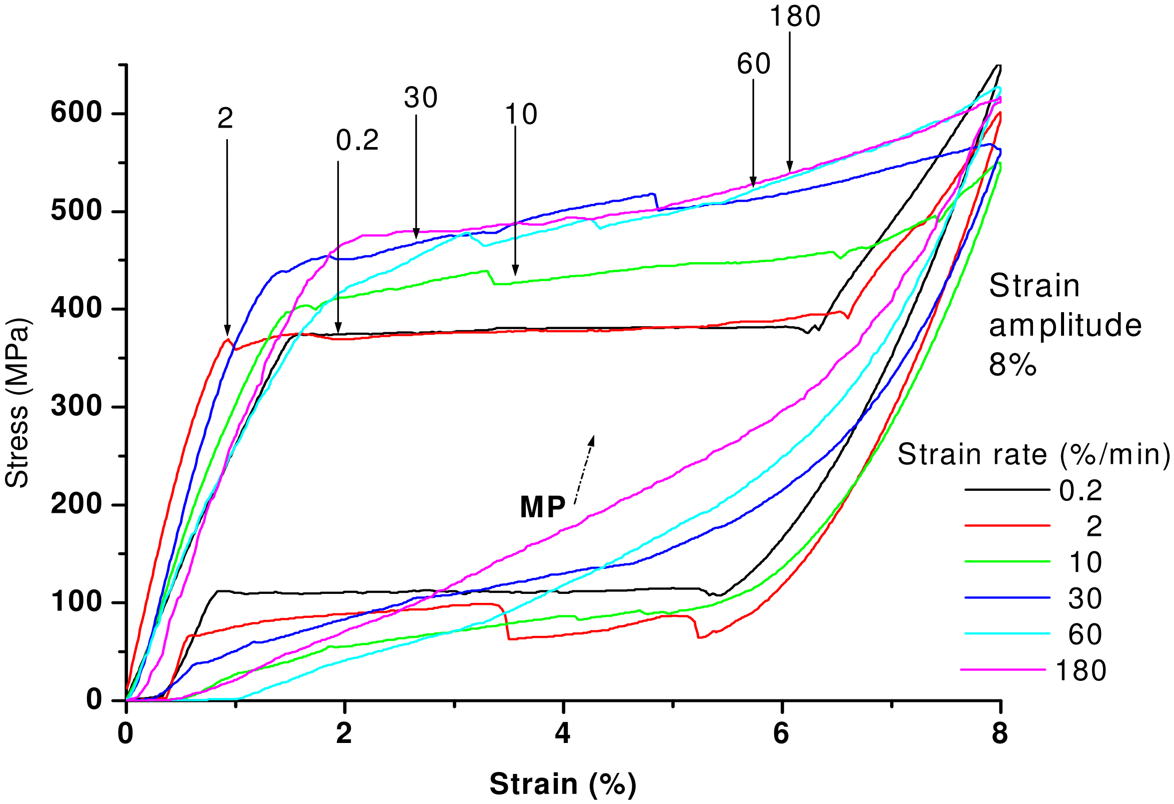

Fig.5.10: Stress vs strain for different strain rates (at 27° C) at a strain amplitude of 8 %.

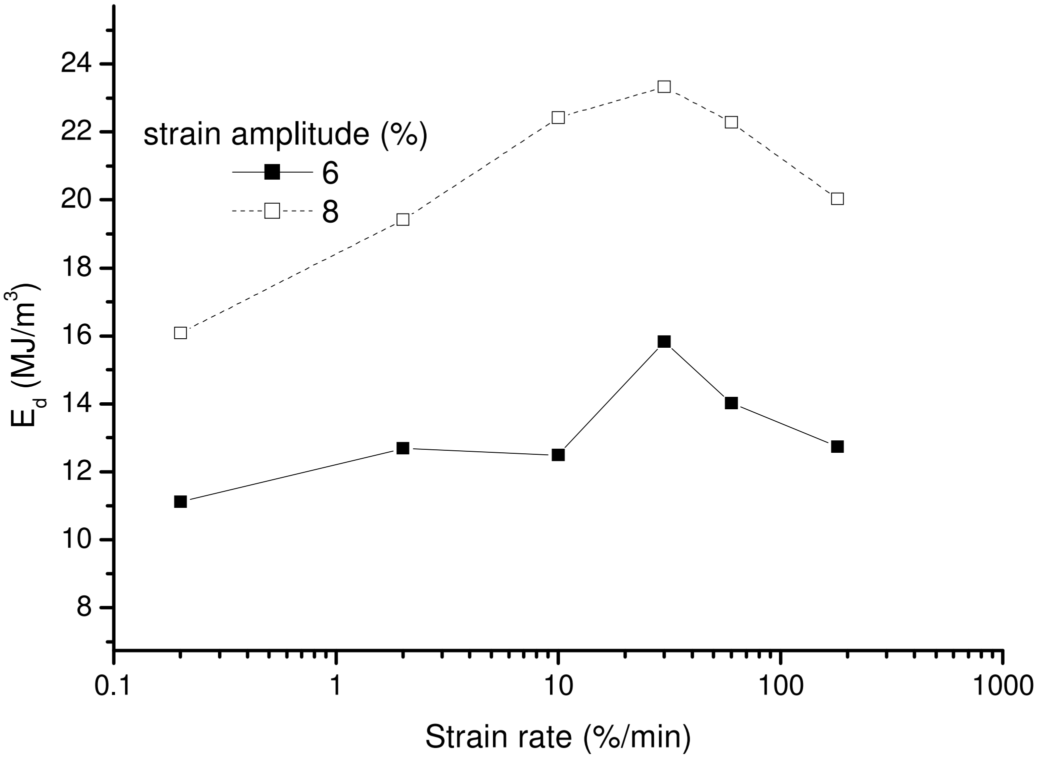

Fig.5.11: E_d vs total strain for constant strain amplitude of 6 and 8%.

Fig.5.11 shows a semi log plot of E_d vs. strain rate for cyclic strain amplitude of 6 and 8%. It is seen that the E_d increases from 0.2%/min (0.06mm/min (0.0027Hz)) and peaks in the range of 30 % to 60 %/min, beyond which the E_d sharply decreases till the maximum strain rate (180 %/min). It is also to be noted that in the same strain rate range i.e. 30 % to 60 %/min (9mm/min) the σ_{es} point is not conspicuous in the stress-strain curve (Fig.5.4). Earlier studies [2, 3] have also reported a decrease in E_d with increase in loading rates from the static loading to dynamic loading. However, Tobushi et al [4] reported a constant E_d in the range of 0.1 to 1 %/min and increases thereafter till 100%/min.

The interplay of the ductile behavior, temperature and strain rate effects, energy storage/dissipation during both tensile testing and cycling can be summarized as follows: it is clear from these experiments (for both the 100 mm and 30 mm length wires) that the Ni Ti SMA alloy possesses inherently ductile characteristics over a wide range of temperatures (-50 to 100^0 C)and strain rates. These include below martensite finish and above austenite finish temperatures. It also includes low (0.2%/min) as well as high (800%/min) strain rates. From Table 5.3 it is clear that the E_d is high above the strain amplitude of 6 %. At lower strain amplitudes the amount of SIM formation is rather low as a substantial amount of loading strain is expended in the elastic deformation of the parent phase which has no energy dissipation capability. This limits the energy dissipation at lower strain amplitude. On the other hand at strain amplitudes beyond 6% the residual strain levels increase thus limiting the utility in SE SMA devices. It is also clear that the SIM formation response is dependent on the strain rate. Similar inferences have been reported in the literature [48], [49] for the similar range of strain rates on SMA thin wires. The hysteresis and therefore the energy dissipation are also dependent on the strain rate. At higher strain rates even before the SIM formation is complete the elastic deformation of the already formed SIM commences. It is obvious that the SIM formation is not able to cope with the externally imposed higher strain rates. Thus in the SIM plateau region there are two competing phenomena viz; the SIM formation and elastic deformation of already formed SIM (EDAFSIM). At a strain rate of 0.2%/min and below the sole phenomena that exists is the SIM formation which manifests as an almost perfect horizontal line. As the strain rate increases the EDAFSIM is observed before the completion of the SIM plateau and as a result the SIM segment of the loading curve translates upwards with increase in strain rates. Also the amount of residual strain at the end of the cycle increases with increase in strain rates. It is clear that the higher strain rates interfere with the SIM formation and also result in higher levels of residual strain. As is clear from Figs. 5.11 and 5.11 the energy dissipation, E_d peaks in the range of 30-60 %/min beyond which it decreases. The decrease in E_d beyond a certain strain rate can probably be explained by the following hypothesis. At low strain rates the SIM predominates and the reverse M to A transformation during the unloading also transcribes an almost perfect flat horizontal line. The E_d increases up to the point where the SIM and the associated M to A predominate. At higher strain rates the EDAFSIM gains ascendency and during the unloading it results in an increase of slope . The increase in slope is because at higher strain rates it is predominantly the EDAFSIM that is recovering and not the SIM. The slope of the EDAFSIM is substantially higher than the almost flat M A transformation. As this slope increases the area under the loading unloading curve decreases as can be seen in Figs.5.9 and 5.10. Therefore at high strain rates the E_d decreases. The energy dissipation is large compared to conventional materials. In the range of strain rates studied, higher the strain rate higher is the slope of the SIM plateau and hence higher is the stiffness of the device (i.e. the stiffening effect provided by the SE SMA on the arch in the landing gear). As the strain rate increases the mean point shifts to the higher stress, higher strain regime. Also, from these studies, it is possible to deduce the optimum strain amplitudes and the optimum energy dissipation for the given range of strain rates. Thus it is clear that the strain rate has a direct bearing on the energy dissipation. These results are useful inputs for the design of SE SMA incorporated devices.

Chapter 6: Cyclic and Fatigue Behaviour

6.1. Introduction:

This chapter relates to the discussions on cyclic and fatigue loading behaviour. The stress-strain cycling between the austenite and martensite phases has similarities with the tension-tension cycling of conventional metals. However, the magnitude of both elastic and plastic strains is far greater compared to conventional metals. Further, in the conventional metal, the magnitude of plastic strain is either comparable to the magnitude of elastic strain or even greater. But, in the case of NiTi thin wires, the magnitude of plastic strains is far lower compared to the magnitude of the elastic strains, when they are used as actuators or for energy dissipation. Since these are thin wires, the fatigue loading is always tension-tension. Also, the mean stress as well as the mean strain keeps shifting by substantial amounts till the material stabilizes, as these materials are thermo-mechanically or stress cycled. This is in sharp contrast to cycling in conventional metals where both the mean strain and mean stress shift by relatively very small magnitudes. It is to be noted that the total strain is kept constant during the strain controlled loading cycles. Depending on the stress and strain levels, the stabilization might take as many as a few hundred cycles. It is well known that the shape memory properties stabilize after a certain number of cycles in the case of both thermal and super elastic Ni Ti SMA alloys. In the thermal SMA the thermo-mechanical cycling (within the elastic range) induces a certain amount of permanently deformed martensite (PDM). This gives rise to the accumulation of the residual strain in the material. In the case of SE SMA the mechanical (tension-tension) cycling is done at constant temperature to study the cyclic behavior. Even here the cycling in the elastic range gives rise to permanently deformed martensite which in turn leads to the accumulation of the plastic strain. Generally the stabilization of the residual strain parameter takes place within a few hundred cycles when the cycling is done within the elastic range. In both the cyclic and fatigue loading experiments the study of the evolution of the plastic strain parameter is important. The stabilization of the plastic residual strain indicates to some measure that the material can be used for a sufficiently long number of cycles at the prescribed strain amplitude and strain rate. However there are situations where the strain amplitudes and stress levels might exceed the elastic range. In such situations it is worthwhile to examine whether the evolution of the plastic strain parameter could fit into the Coffin-Manson type of equations for predicting fatigue life. It is pertinent to mention here that for conventional metals the Coffin-Manson relationship has been used for low cyclic fatigue conditions in cases where the fatigue results from cyclic strain [51]. The investigations carried out by Melton et al, Young et al, Matsui et al and Araujo et al ([50], [52] & [53]) has been briefly described in chapter 1. Tobushi et al have proposed an equation similar to the Coffin- Manson equation for predicting the fatigue life depending on strain amplitude, temperature and frequency. Gong et al and Sittner et al have attempted to model the evolution of super elastic stress-strain cycling behavior. The fatigue behavior related investigations of Yawny et al ,Yan et al Sulpice et al , Wang et al, Zhang et al, Roy et al, Siredey et al and Eggeler et al ([59] – [67]) have been briefly discussed earlier. Many of the above studies addressed the fatigue of either large or very large cyclic strain amplitudes. The present studies also focus on the large cyclic amplitudes. The tension-tension cyclic loading relates to the experiments explained in section 2.3.7. The fatigue loading relates to the experiments explained in section

2.3.8. The evolution of plastic strain is important for the study of both cyclic and fatigue behavior. Section 6.2 deals with the strain amplitudes of 6 & 8% in the elastic range in relation to the energy dissipation characteristics. Section 6.3 deals with even larger cyclic strain amplitudes as high as 15% at stress levels beyond the elastic range. In this section the focus is on the fatigue related aspects only and energy dissipation aspects are not considered.

6.2. Cyclic Loading:

Large cyclic amplitude loading is relevant to the study of SMAs as already stated.

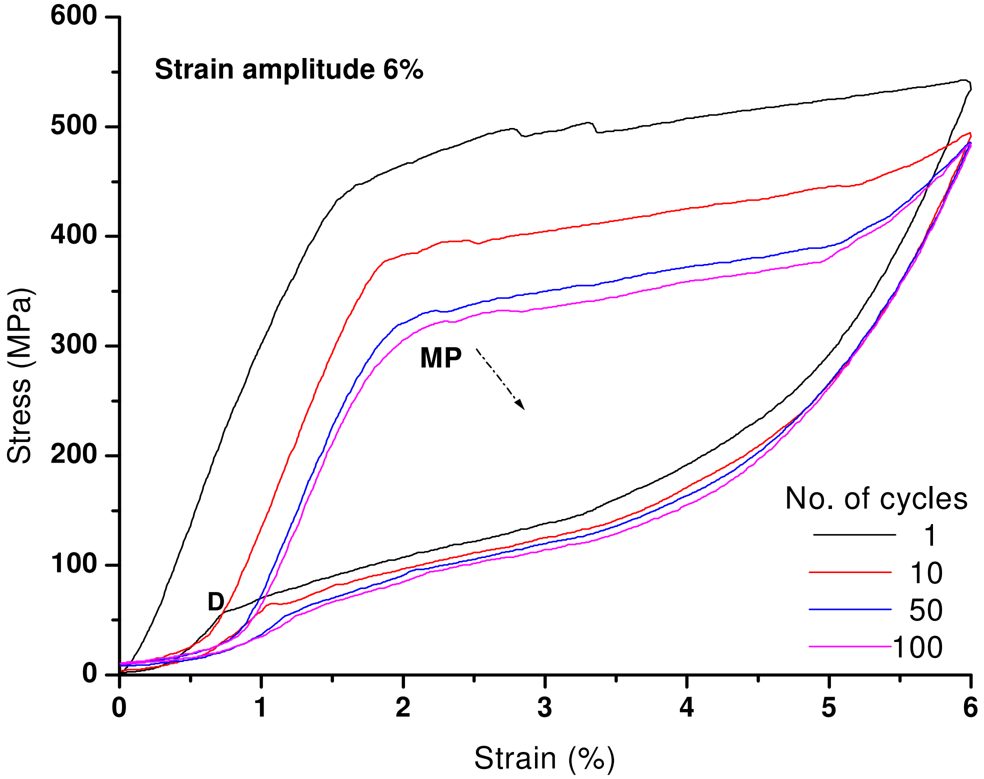

Fig.6.1: Stress vs strain (at 27 °C) for SR of 30%/min till 100 cycles at an amplitude of 6%.

The effect of cycling at a constant strain rate is discussed in this section. Several parameters such as the loading plateau stress, unloading plateau stress and residual strain are relevant here. The residual strain 'ε_r' is the remnant strain after the end of one complete cycle when cycled within the elastic regime. Fig.6.1 shows the stress-strain plot of the cyclic testing for the 1st, 10th, 50th and 100th cycle. A marked difference between the 1st and 100th cycle in terms of E_d (i.e. the enclosed under the stress-strain curve for one complete cycle) is observed. In the first cycle there is a clear change of slope to distinguish the re-transformation of SIM back to austenite and the start of unloading of completely transformed austenite. This is identified as the point 'D' on the stress-strain curve. With cycling the loading plateau stress associated with the onset of SIM decreases and the residual strain accumulates. In the 100th cycle the unloading segment that is associated with the re- transformation of SIM back to austenite merges with the unloading segment of the completely transformed austenite. The distinct change of slope that is identified as point 'D' of the 1st cycle is absent in the 100th cycle as the change of slope resulting from the overlapping of the two processes is more gradual. This merged unloading segment gradually shifts to the lower stress regime. Associated with the shift to the lower stress regime is the accumulation of residual strain with each successive cycle. The residual strain is due to the formation of permanently deformed martensite that accrues during cycle. The rate at which the permanently deformed martensite is formed is more in the initial cycles. Therefore the amount of austenite that is available for transforming to SIM decreases proportionately. Thus the loading plateau stress decreases and the SIM segment shifts to the lower stress higher strain regime. Accordingly it is clear that the mean point also shifts to the lower stress /higher strain regime for the 6% strain amplitude cycling at the strain rate of 30 %/min. This is in contrast to the shift of the mean point to a higher stress/higher strain regime with increase in strain rates. These changes in mean point have implications for the design of superelastic devices.

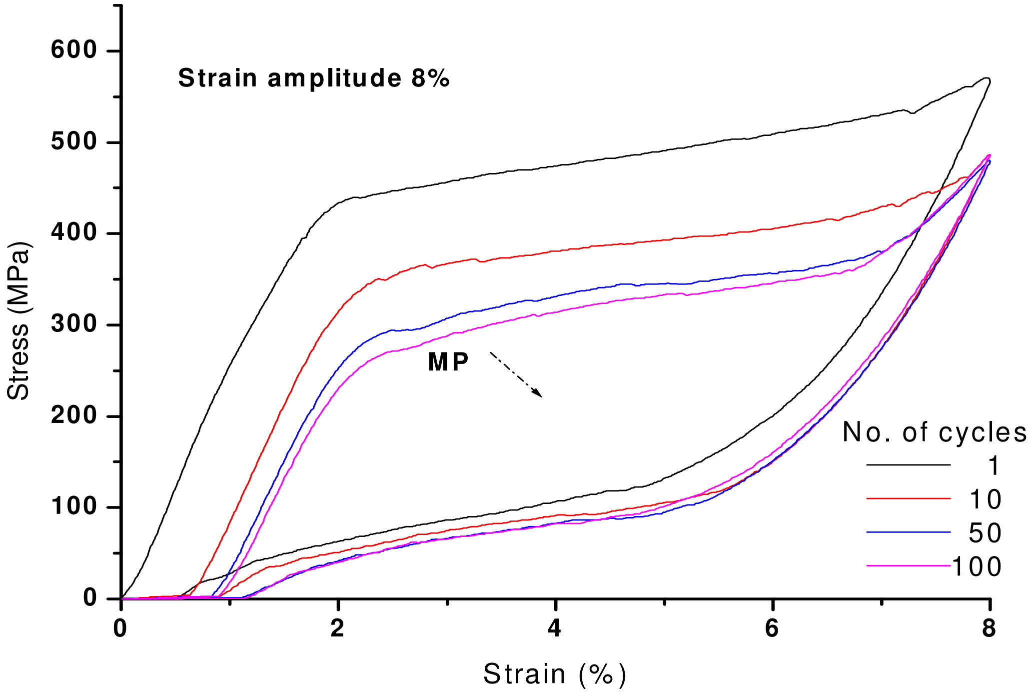

Fig.6.2: Stress vs strain (at 27 ^{o}C) for strain rate of 30%/min till 100 cycles at an amplitude of 8%.

Fig. 6.2 shows the stress-strain behavior for the cycling at strain amplitude of 8%. The results are similar to the cycling at 6% strain. However, the residual strain values are higher. Table.6.1 summarizes the changes in E_d and E_r for the 6 and 8 % strain amplitude cycling respectively. It is clear from the table that the energy dissipation capability at the 100th cycle is about half the energy dissipation capability of the first cycle.

No. of cycles	E_d (MJ/m^3)		E_r (MJ/m^3)		ϵ_r (%)	
	8%[a]	6%[a]	8%[a]	6%[a]	8%[a]	6%[a]
1	22.20	15.13	10.46	9.28	0.33	0.27
10	16.05	10.87	9.90	9.39	0.63	0.47
20	14.98	9.96	9.97	9.37	0.74	0.55
30	14.13	9.45	9.54	9.43	0.78	0.60
40	13.25	8.86	9.58	9.32	0.80	0.62
50	12.92	8.32	9.77	9.15	0.83	0.65
60	12.48	8.38	9.71	9.17	0.85	0.66
70	12.53	8.36	9.67	9.11	0.88	0.68
80	12.04	8.28	9.42	9.13	0.90	0.69
90	11.89	8.15	9.66	9.04	0.93	0.71
100	11.66	7.94	9.50	9.11	0.97	0.72

Table.6.1: Variation of E_d and E_r with respect to number of cycles

a: strain amplitude

Therefore the cycling at a constant strain rate contributes to the reduction in the energy dissipation capability. Fig.6.3 shows the variation of E_d and residual strain with respect to number of cycles. The rate of decrease in E_d is high in the first 10 cycles and progressively decreases in the successive 10 cycles for which the results have been plotted. This is a direct consequence of the high rate of permanently deformed martensite formation with respect to the number of cycles in the first part of the cycling. The energy dissipation is higher for the 8% cycling amplitude compared to the 6% cycling.

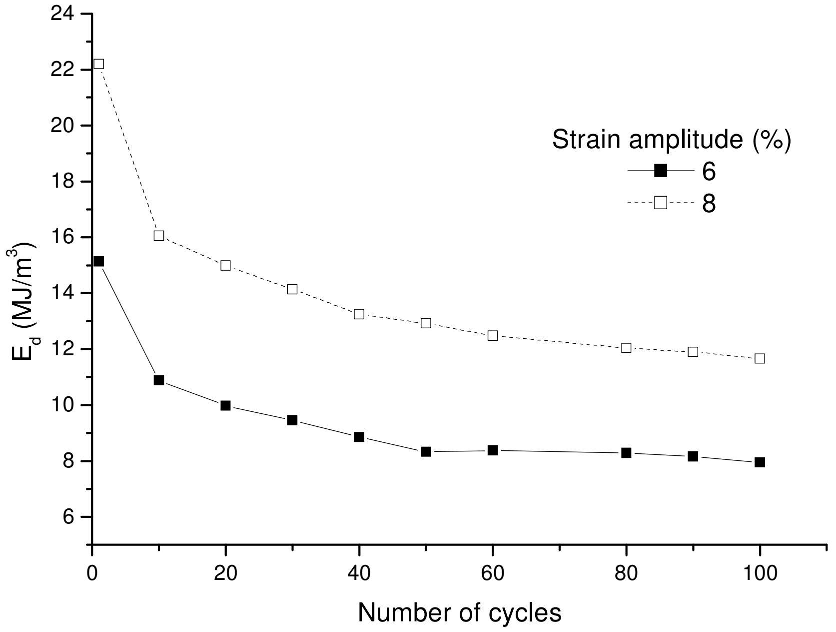

Fig.6.3: E_d vs number of cycles for constant strain amplitude of 6%.

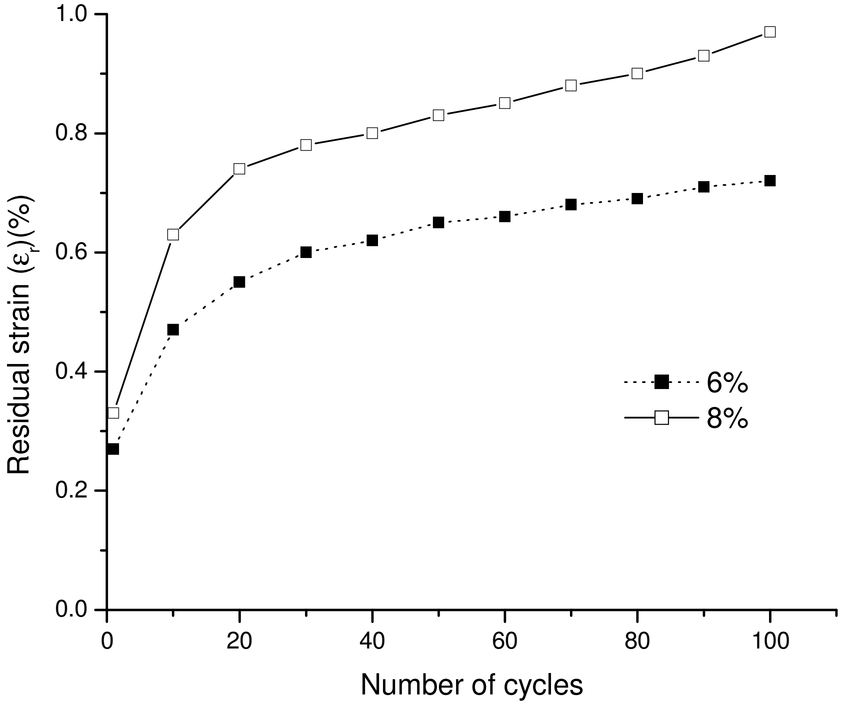

Fig.6.4: 'ε_r' vs. number of cycles for constant strain amplitude of 6 & 8%.

Fig. 6.4 shows the variation of the residual strain for the 6 and 8 % cycling. The residual strain accumulation is higher for the 8% cycling compared to the 6% cycling. Therefore though the E_d was higher for the 8 % cycling since the residual strain is higher this is not favorable from the fatigue point of view. It is clear that there has to be a tradeoff between the choice of the maximum cyclic strain amplitude and the maximum realizable energy dissipation. It is seen that E_d decreases and the residual strain increases with increasing number of cycles and both the parameters stabilize around 80 cycles. Thus it is clear that the stabilization of residual strain and E_d is based on the same underlying mechanism and is related to the SIM formation.

In this section the cyclic strain which was typically in the range of 6-8 % was within the elastic zone. Even within the elastic zone the cycling does result in some amount of residual strain which might be due to the accumulation of permanently deformed martensite. The next section deals with the cycling at very large strain amplitudes (as large as 15 %) by taking the stress to higher regimes.

6.3. Fatigue Behavior:

Predicting the fatigue behavior of NiTi thin wires is one of the prominent issues. The problem is compounded by the fact that it is not possible to introduce a crack in a thin wire and monitor its growth as is done in the case of a conventional metal rectangular cross section specimen. It is against this background that the issues involved in modeling and experimentally measuring the fatigue related properties of NiTi thin wires are discussed. Specific case of fatigue failure of a super elastic NiTi thin wire subjected to very large amplitude (with strain values as large as nearly 15 %) cyclic fatigue loading is considered and the experimental result is compared with theoretical prediction using the Coffin-Manson method. The amount of plastic deformation in each cycle is a useful parameter to predict the fatigue behavior. Based on this information the fatigue degradation of the material is predicted using the Coffin-Manson method.

Fig.6.5. shows a typical plot consisting of one complete first cycle and the loading part of the second cycle for a strain level of 10.0 % above the 100 N load and 1.5 % initial strain. The maximum stress value in the first cycle corresponds to 702.12 MPa (around 200 N) and the total strain value corresponds to 11.5%.

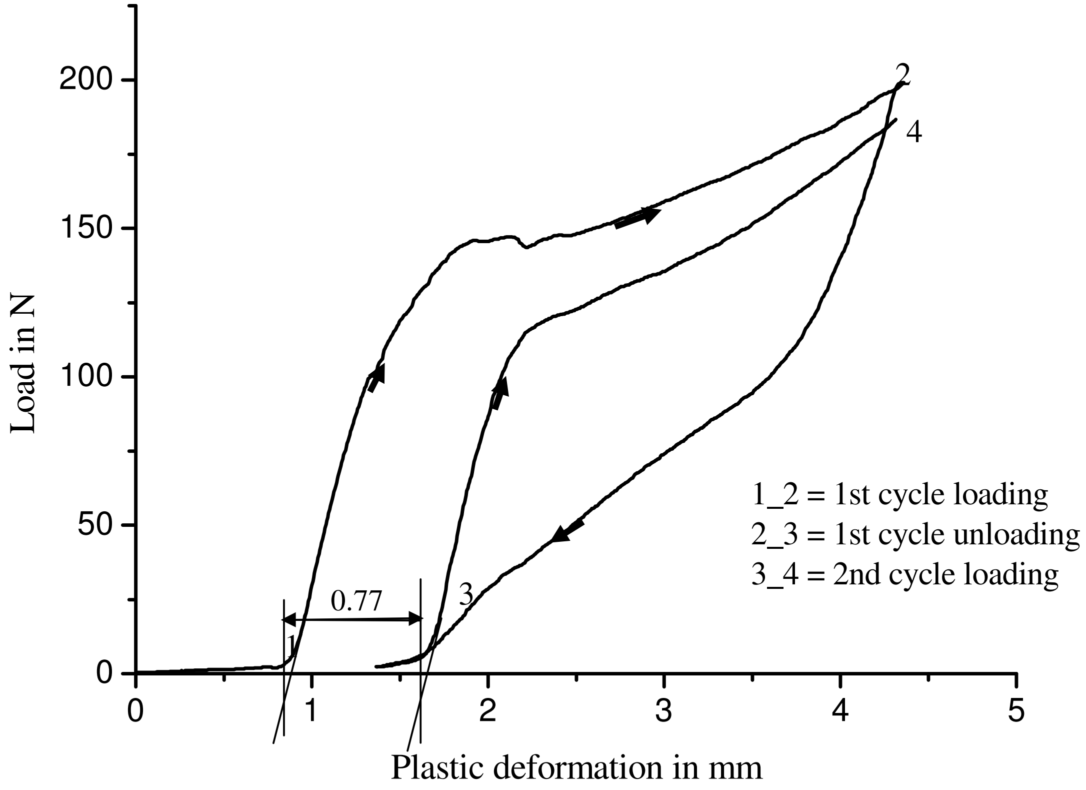

Fig.6.5: Plastic deformation in the first cycle

While undergoing the stress-strain (tension – tension) cycling the super elastic NiTi wire is converted from austenite to martensite during loading and back to austenite during unloading. Coffin – Manson relationship, equation 1.2, of the form

$$N_f^{\beta}\Delta\varepsilon_p = K$$

explained in chapter 1 is used for predicting the fatigue life to failure. Fig.6.6 shows the plot of plastic strain per cycle (measured from the experiments) against number of cycles to failure (N_f) from which the coefficients β and K are obtained to be 0.62 and K=0.5 respectively. 'AB' is the straight line fit of the failure data points. 'β' is the slope of the line AB. Extrapolating the line BA results in intersection on the 'y' axis at point C (i.e, the strain intercept for N_f =1). 'OC' on the 'y' axis represents the constant 'k'. The plastic strain per cycle between the 1st and 2nd cycle with respect to the different strain levels, measured number of cycles to failure and that calculated from the Coffin-Manson relationship are shown in Table.6.2.

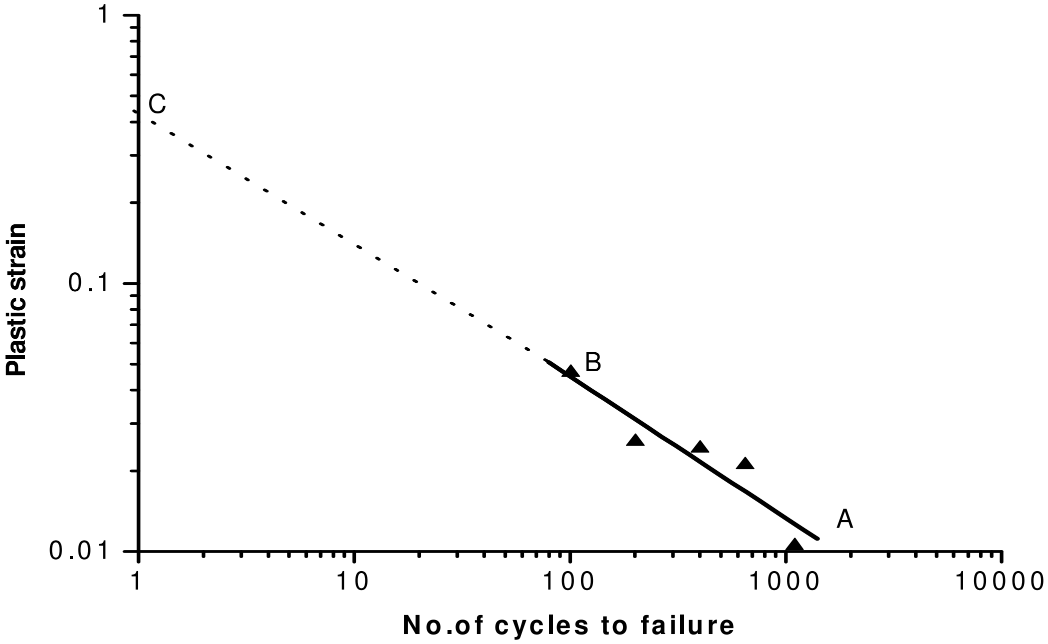

Fig.6.6: Plastic strain per cycle vs. No. of cycles to failure

SL NO.	Total Strain (%)	Plastic Strain per cycle ($\Delta\epsilon_p$)	Cycles to failure - computed (N_f)	Cycles to failure - measured (N_f)
1	14.83	0.0456	46	100
2	11.5	0.02567	119	200
3	9.0	0.02425	130	400
4	8.17	0.021	163	650
5	6.5	0.0105	497	1100

Table.6.2: Comparison of measured and calculated 'N_f' to failure at different strain levels.

As can be seen from the table.6.2 the imposed cyclic strain amplitudes are large and are in the elastic-plastic regime for NiTi SE SMAs (i.e. in the high stress regime). The magnitude of plastic strain per cycle obtained between the 1st and 2nd cycle is proportional to the imposed strain amplitude. Though the computed result from the Coffin-Manson equation shown in the table is only about 40% of the actual measured failure value, it shows a trend similar to that for conventional metal fatigue behavior predicted using the coffin-Manson relationship. The results of section 6.2 wherein the cycling was within the elastic regime and section 6.3 where the cycling was in the elastic-plastic regime is summarized as follows:

In the elastic regime the cyclic strain amplitude of 6% at a strain rate of 30%/min gives good energy dissipation properties. The accumulated residual plastic strain is within 1%. The 8% cyclic strain amplitude though has a higher level of energy dissipation the plastic strain is higher which adversely affect the fatigue life of the material. The stabilization of the energy dissipation property and residual strain takes place at the same number of cycles and is related to the same underlying mechanism. The stabilization of E_d and residual strain for the case of 6 % strain amplitude cycling can be hypothesized as follows. In the first few cycles the residual strain accumulation is large. The residual strain is due to the PDM (resulting from large transformation strain reversals) which cannot transform back to austenite. Therefore the amount of austenite available progressively decreases in each cycle. The material composition of the initial elastic deformation segment is no longer fully austenitic. It is a mixture of austenite and PDM. Therefore the elastic strain and the threshold stress (i.e. the SIM onset stress) of this initial elastic deformation segment progressively decreases. Thus the area under the loading-unloading curve and therefore the energy dissipation progressively decreases. The accumulation of the PDM is also the reason for the gradual merging of the SIM unloading segment and the reverse M to A segment. The PDM progressively stabilizes the material and after a certain number of cycles (which is about 100 for the 6% strain amplitude cycling) the PDM is responsible for complete stabilization at which point we say that the E_d and residual strain values have stabilized. Beyond the stabilization the amount of PDM remains more or less constant for a relatively large number of cycles. These observations are important from the point of designing SE SMA devices. The implications for the design of SE SMA devices in relation to strain amplitude, energy dissipation and energy dissipation are thus brought out.

In section 6.3 the focus is mainly on evolution of the plastic strain parameter and not on the energy dissipation characteristics. The plastic strain between successive cycles is used to arrive at the parameter 'β' which is fit into the Coffin-Manson relation to predict the fatigue life. This method of fatigue life prediction using the empirical method gives some idea of the fatigue of the material.

J.M.Young et al [4] used the Coffin-Manson relationship for predicting *In Vivo* failure of pseudoelastic NiTi devices under low cycle, high amplitude (range of 2.5 to 18.2%) rotational bending fatigue at rotational speeds of 100-1000 rpm. In the present case the fatigue cyclic testing is in the tension-tension mode with strain amplitudes in the range of 6.5 to 15 % with a loading rate of 1mm/sec. The experimental values of failure lives obtained in the present study are comparable with that reported by J.M.Young et al.

A further discussion in relation to the large strain and high stress imposed in the present set of fatigue experiments is relevant.

Two important parameters, net stress and net strain, affect the fatigue behavior of NiTi thin wires just as the amplitude of stress and strain affects the fatigue of conventional metals. It is quite common to have a fatigue life of 100,000 cycles if the net strain is limited to 1 % and the net stress is limited to 100 MPa (about 28 N for a 0.6 mm diameter wire). At the other extreme, if the net stress is about 500 MPa (about 145 N) and the net strain about 6 %, then the wire would have a fracture life of only a few hundred cycles. It is important to bear in mind that in the present experiment, the value of plastic strain range is about 1/4th the value of the total strain range of 6- 15%, which is characteristic of a super elastic SMA. The net stress as the material is cyclically loaded and unloaded is about 500 MPa (about 145 N) in the experiment. The cycling strain rate is 1 mm/sec. Therefore, this combination of 500 MPa (145 N) stress, 15 % strain and 1mm/sec strain rate is the upper limit at which one can use this material. Since the fatigue testing is severe in terms of all the three parameters, the wire has fractured at a value as low 100 cycles. It is to be noted that the total cyclic strain is kept constant during both the cyclic (within elastic regime) and fatigue (elastic-plastic regime) loading experiments. The amount of elastic and plastic strain however keeps changing in a predictable manner during the course of the cycling. These inferences again serve as useful inputs for the design of SE SMA based devices.

Chapter 7: Design, Fabrication, Testing and Analysis of the Smart Landing Gear

7.1. Introduction:

The design and development of the SE SMA incorporated polymeric carbon composite smart landing gear that ensures soft landings for the RC Blimp is based on a novel design approach. The design is of a generic nature and is applicable to a large class of vehicles. The soft landing is required to ensure that shock and vibration are minimized (to protect the sensitive payload). It is also important that the design incorporates crashworthy features into the landing gear system. Tho et al [71] refers to the design and development of high energy absorbing skid landing gear for helicopters. Stephens et al [72] deal with the development of a dynamic analytical methodology for analyzing the structural behavior of a helicopter skid gear during a high-energy landing. Airoldi [73] and Philips [74] demonstrate crashworthy designs using metal alloy systems. The drawbacks with metallic skids are the landings are hard. Many times the metal skids undergo plastic deformation in response to the impact energy and require frequent replacements. In this chapter the details of the fabrication, design, testing and analysis of the smart landing gear that overcomes the drawbacks of the metallic skids and still ensures soft landings is presented. Prior to this a brief account of the tensile testing of polymeric composites in different configurations is given. The landing gear needs to be secured properly to the envelope and to the main frame. This is done by means of dog-ears. The results of the testing of the landing gear are also briefly given in this work. It is appropriate here at this juncture to discuss the design philosophy for the landing gear.

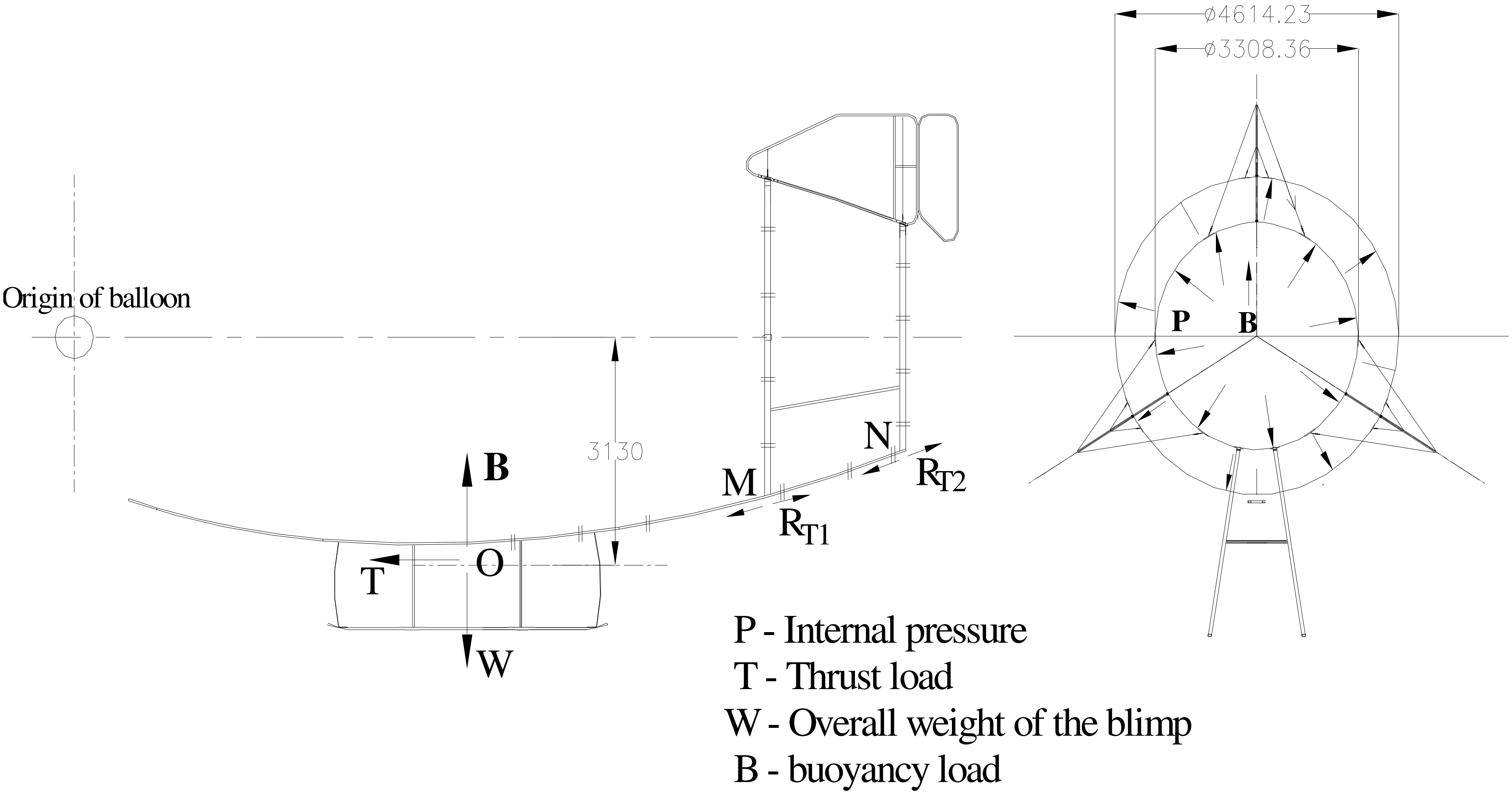

Fig.7.1: Free body diagram for the RC-blimp.

7.2. Design Philosophy for the landing gear:

Fig.7.1 is the free body diagram showing the loads acting on the blimp. The lift (B) load generated by the helium gas filled envelope is balanced by the overall weight (W) of the blimp at point ‘O’. The thrust (T) developed by the engine is mainly reacted at the two rings as reaction forces RT_1 and RT_2 at points ‘M’ and ‘N' respectively. The rings and the landing gear are secured to the envelope by means of dog ears. The landing gear design incorporating polymeric carbon composites and Ni Ti SE SMA provides two load paths for reacting the impact loads; the primary and the secondary. The primary load path is stiff and undergoes very little elastic deformation. The secondary load path which is more flexible [consisting of the curved arch (made of cane with CFRP wrapping) and SE SMA element] also takes a substantial amount of load, undergoes large elastic (buckling) deformations and in the process dissipates large quantities of energy (The secondary load path members are expended after a certain fixed number of cycles). The arch which is in the secondary load path undergoes elastic buckling because of the curved geometry. During impact (loading) the arch buckles elastically and the plateau region of the SMA ensures required compliance. Immediately after the impact (unloading), the SMA reverts back to its undeformed position. In the process of loading and unloading due to the material hysteresis the SE SMA dissipates energy in the form of heat. This feature of having a secondary load path with SE SMA significantly enhances the crash worthy characteristics of the smart landing gear and ensures soft landings as explained in the subsequent sections. Even without the SMA, the landing gear design has two load paths; the primary and the secondary. In this configuration without SMA the arch is the only member in the secondary load path . The arch and beam together do serve the purpose of landing by absorbing the energy of impact, though the energy dissipation capability is very less (i.e. soft landings are not ensured). When the SMA is connected to the arch and thus integrated to the landing gear it brings about a quantum jump in the energy dissipation capability and ensures soft landings during impact.

It is pertinent here to mention that the polymeric composites designed in the conventional sense as in the present case possess very little energy dissipation capability. On the other hand, composites do have multiplicity of failure mechanisms and if designed properly can be made to dissipate substantial amounts of energy. In such situations they become expendable members. However, this discussion is outside the purview of this thesis. Primarily the landing gear has to be designed to absorb the kinetic energy of descent. Figure 7.2 shows the downward force and reaction loads on one of the two segments when the airship impacts the ground. These are estimated based on the maximum gas lift and the velocity of descent. The maximum gas lift for the 320 m^3 airship is 2800 N; the reaction load is assumed to be 60% [84] of this value (assuming a descent rate of 1.5 m/sec) which is 1680 N. Applying a factor of safety of 1.5 on this load, an ultimate load of 2500 N is considered. During landing the skid is assumed to make an angle of 20 degrees with the ground. Since there are two identical sub-units of the skid, each segment will take half of the load i.e. 1250 N.

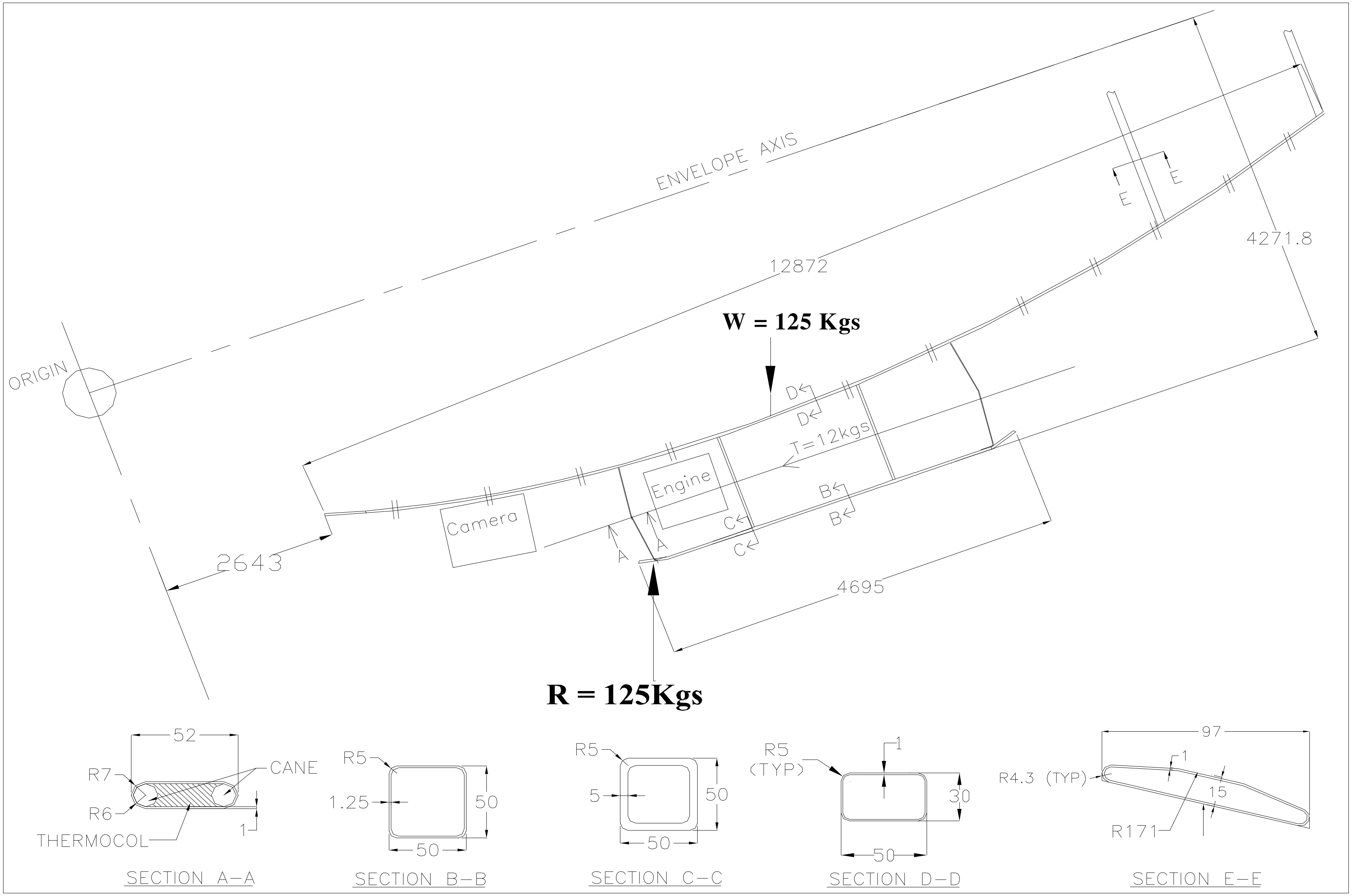

Fig.7.2: The inclined configuration and other details of the landing gear during impact

Fig.7.3 shows the enlarged view of the smart landing gear which comprises landing beams, arches and super elastic NiTi SMA elements. Carbon Fibre Reinforced Plastic (CFRP) is used for the landing beam which first sees the load on impact, cane (naturally occurring plant product) wrapped with CFRP is used for the arch along with the super elastic SMA. The sizing of the arch and landing beam is done in such a way so as to meet the dual requirements of low weight and high energy dissipation while undergoing 'large elastic' (large non-linear recoverable elastic strain) deformations in order to ensure soft landings when the airship impacts the ground. The inherently large energy dissipating character of the super elastic SMA element in the tensile mode of deformation along with the superior elastic bounce back features of the SE SMA, arch landing beam configuration have provided the ideal solution. In order to address the unusually large deformations arising primarily due to the geometric non-linearity a non-

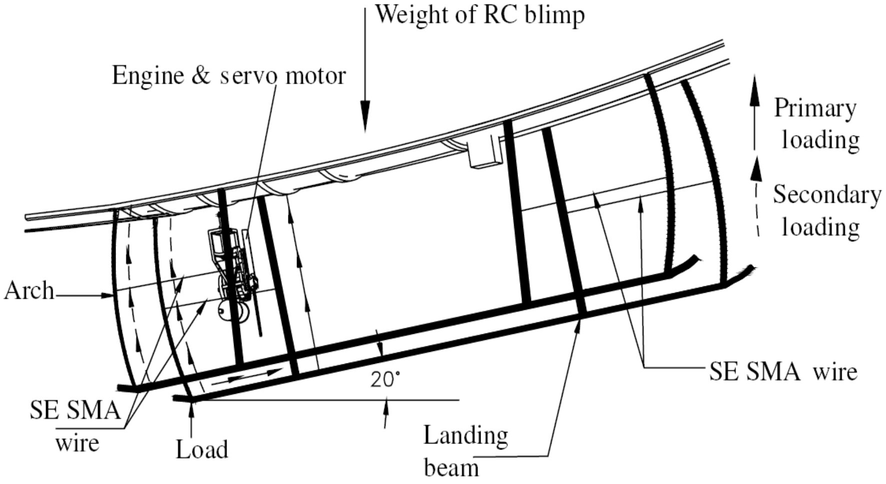

Fig.7.3: Landing gear

linear analysis based on classical and FEM approach has been used to analyze the structure.

The landing gear, which is part of the structural framework, serves the purpose of absorbing impact energy during landing. The impact energy during landing can cause severe shock and therefore render these gadgets ineffective, and even damage them. Therefore, the landing gear (comprising of landing beam, arch and superelastic SMA element) shown in Fig.7.3 has to be designed in such a way that it absorbs the maximum impact energy during landing.

In order to prove the relative superiority of the super elastic SMA incorporated carbon composite smart landing gear, it was considered appropriate to design a conventional aluminum metal landing gear consisting of a helical tensile spring in one option and a compression spring in another. These two options were evaluated against the SMA

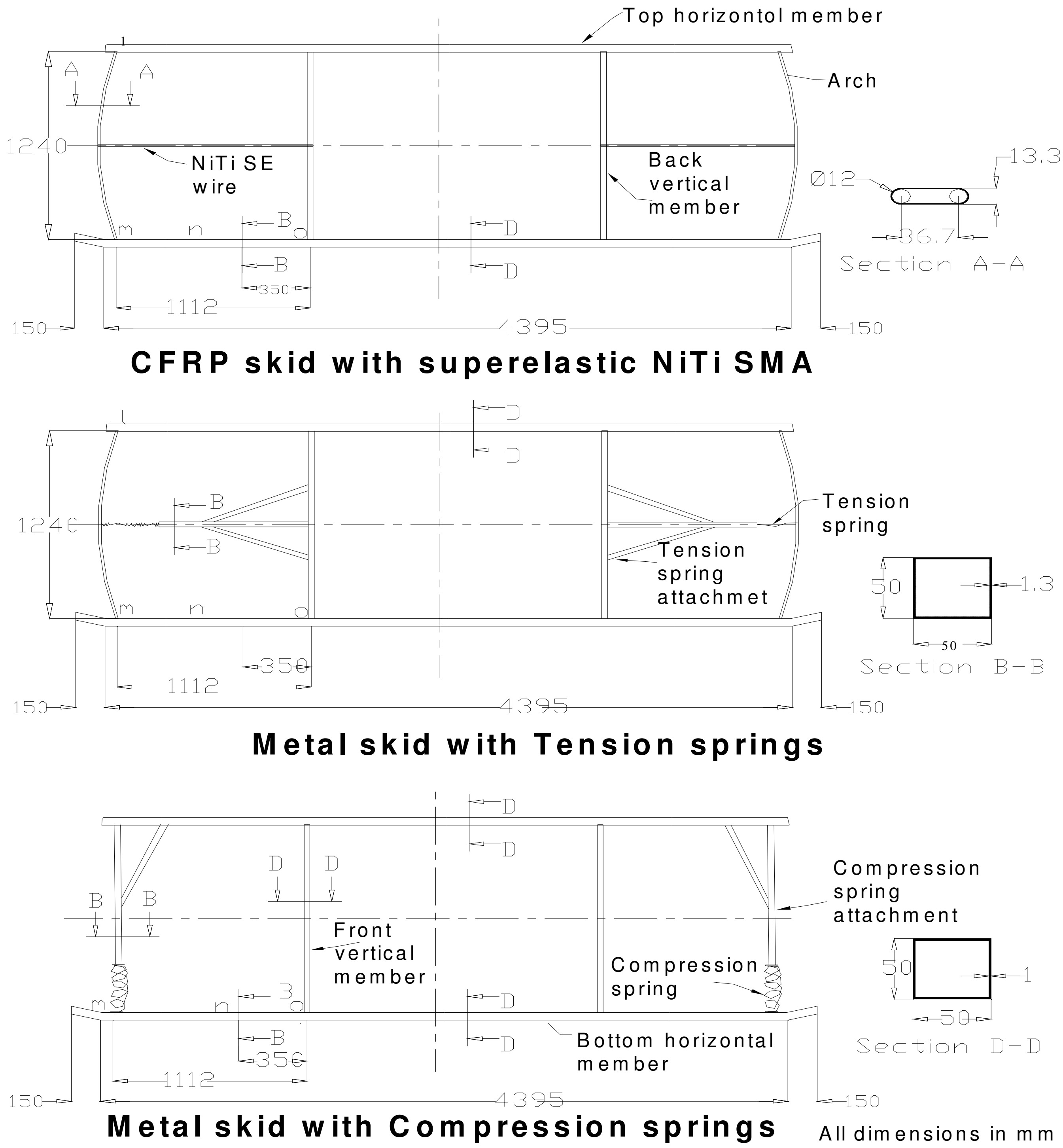

CFRP skid with superelastic NiTi SMA

Metal skid with Tension springs

Metal skid with Compression springs

Fig.7.4: Comparison of different landing gears

based CFRP smart landing gear. Fig.7.4 and Table.7.1 bring out the comparison between the landing gears. It is very clear from the table that the super elastic SMA incorporated carbon composite smart landing gear weighs far less than an equivalent aluminum landing gear either with a helical tensile spring or a compression spring.

Further, even within the smart landing gear the SE SMA was replaced with a steel wire and the relative superiority of using the SE SMA wire along with the CFRP arch is thoroughly discussed. To ensure soft landing in this design a part of the landing gear referred to as the arch incorporates a satisfactory configuration in terms of geometry and weight of natural cane, carbon composites and NiTi based SE SMA.

Table.7.1: Comparison of the landing gear performance using different materials

Parameters	Superelastic SMA based CFRP smart landing gear	Aluminum landing gear with tensile spring	Aluminum landing gear with compression spring
Weight (N)	160	257.35	247.47
Maximum deflection (mm)	48	48	48
Maximum load (N)	2500	2500	2500

This is designed to undergo 'large elastic' deformations and can be expended after using it for a fixed number of cycles (typically a few hundred). The arch is connected to a landing beam which first experiences the load during impact while landing.

As shown in Fig.7.3 the arch is curved outwards and while loading (during impact) the curvature further increases. When the super elastic SMA is connected to the arch the SE SMA element is in tension. The arch and the SMA together provide the required compliance, which is required to achieve large elastic deformations. The blimp design assumes the landing to be nose down at an inclination of about 20 degrees to the ground (Fig.7.3). To take care of the unforeseen nose up landings the landing gear sub-units are mirrored about the vertical axis (Fig.7.4). Therefore, the construction of the landing gear unit is symmetric about this axis shown in Fig.7.4. The landing gear is effective for landing at inclinations less than 20 degrees also.

7.3. Tensile Testing of Polymeric Composite Materials:

Polymeric Composites are those materials, which contain fiber reinforcements in a polymer matrix. The tensile behavior of these composites has been investigated by many researchers. M.M. Shokrieh et al [3] reported on tensile behaviour of unidirectional glass/epoxy composites under both quasi static and intermediate strain rates in the range of 0.001–100 s^{-1}. They observed that the tensile modulus and strain to failure increase slightly by increasing the strain rate. Taniguchi et al [7] characterized the dynamic tensile strength of unidirectional Carbon/Epoxy composites and presented an empirical failure criterion. K. Gliesche et al [8] carried out investigations of in-plane shear properties of ± 45°carbon/epoxy composites using tensile testing and optional deformation analysis and showed that the shear behaviour is affected by the layer thickness and/or by the weight per unit area of the reinforcement. W.V. Paepegem, et al [9] modeled the highly nonlinear shear stress-strain response of glass fiber-reinforced composites. S.H. Lee et al [10] and A. Godara [11] investigate the damage mechanisms in polymeric composites. T.P. Skourlis [12] deals with the effect of temperature on the inter phase. Z H. Karadeniz et al [85] present a numerical study on the coefficients of thermal expansion of fiber reinforced composite materials. The evaluation of tensile properties of natural bamboo fibers in a polymeric matrix is covered in K. Okubo et al [86].

In the present work the reinforcements considered are carbon and glass. The matrix is epoxy resin system. The quasi static tensile testing has been carried out on unidirectional and bi-directional polymeric composites. The fibers possess much higher strength and moduli compared to the matrix. The mechanical properties in a given direction are proportional to the amount of fibers oriented in that direction. Both the strength and moduli reduce considerably when the angle of the applied load deviates from the direction of the fibers in the composites [76]. It is possible to realize a wide range of mechanical properties by changing the fiber orientation in the polymeric composite. Fig.7.5 shows the carbon and glass composites in different orientations. The SE SMA and naturally occurring cane material behavior is also included. In table 7.2 the important mechanical properties viz; tensile strength, young's modulus, Poisson's ratio, failure strain and approximate value of design strains are tabulated. Fig.7.6 shows the stress-strain behaviour of the polymeric composites with different orientations. The unidirectional CFRP specimen has a tensile strength as high as 1500 MPa and a modulus as high as 130 GPa with a relatively low failure strain of 1.5%. The density of CFRP is as low as 1.6 g/cm^3. Specific strengths and stiffness's are obtained by dividing the strength and stiffness values by the densities of the materials. The high specific strength and specific stiffness values of UD CFRP composites are ideally suited for design of stiffness critical aerospace structures such as wing, fin etc. This explains the low design strain values for carbon composites which are as low as 0.3%. This is the case for the UD, BD tensile and in-plane shear strains in carbon composites. For the case of glass composites since the failure strains are relatively higher the design strain is also marginally higher at a value of 0.5%.

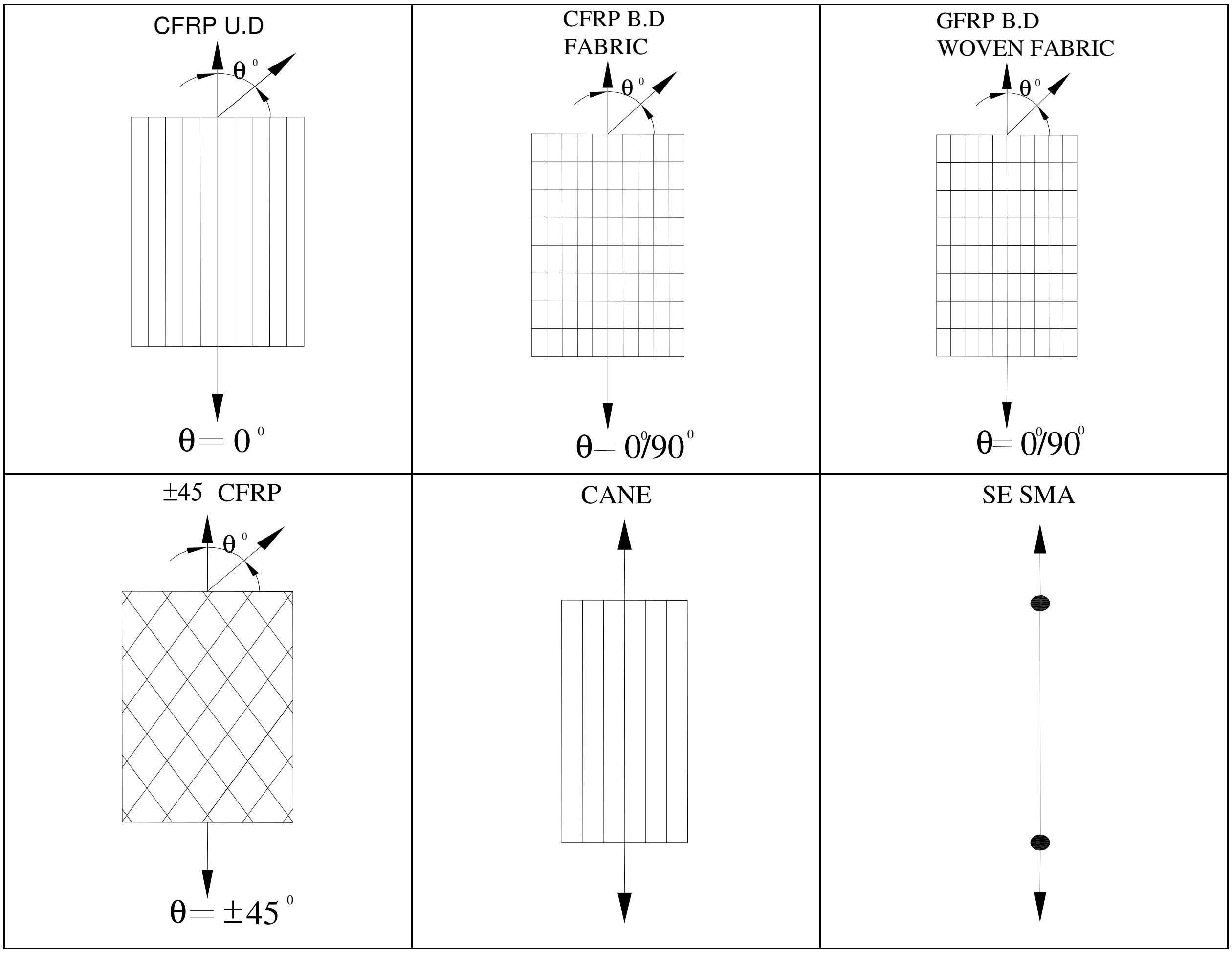

Fig.7.5: Loading direction and fiber orientation for different materials.

In the Fig. 7.6 the CFRP B.D test coupon has tensile strength values as low as 600 MPa and moduli of 60 GPa. It is therefore clear that the change in orientation of some of the lamina fibers (in relation to 0 deg. orientation of Fig 7.5) to 90 deg. results in lowering of the strength and stiffness values. Likewise for the case of GFRP the tensile strength and modulus are further reduced to 400 MPa and 20 GPa respectively. This is because the glass fibers have lower strength and moduli compared to the carbon fibers.

The failure strain of the glass composites is however marginally higher compared to the failure strains of carbon composites. The in- plane shear properties of a ± 45 deg. orientation CFRP is strikingly different from the tensile properties of a 0 deg. UD CFRP test specimen. Fig.7.5 also shows the loading direction (i.e. 0 deg.) and the orientation of the specimens. The shear strength and shear moduli are as low as 100 MPa and 5 GPa respectively. The important thing to notice here is that the gross failure strains are large (higher than 10 %) due to the large plastic strain. This is because the mechanism of failure during the in-plane shear of a ± 45 deg. CFRP specimen is much different from the 0 deg. unidirectional CFRP test specimen. During in-plane shear as the specimen is loaded axially as shown in Fig. 7.5, the angle between the fibers, which is initially ± 45 deg., continuously changes towards smaller values with the yielding of the weaker matrix. The plastic yielding of the matrix starts around 2 % strain as can be seen in the same figure. The loading is resulting in a continuous re-orientation of the fiber

Table.7.2: Strength and Moduli of Polymeric Composites and Cane.

Type	Strength (MPa)	E (GPa)	Poisson's Ratio	Design Strain (%)	Failure Strain (%)
CFRP UD	1500 (Tensile)	130 (Tensile)	0.3	0.3	1.5
CFRP BD	600 (Tensile)	60 (Tensile)	0.04	0.3	1.5
+/- 45 CFRP	100 (shear)	5 (shear)	--	0.7	---
GFRP BD	400 (Tensile)	20	0.3	0.5	2
Cane	15 (Tensile)	4	--	0.5	---

angles, which is manifest as a very large plastic strain. The large plastic strain

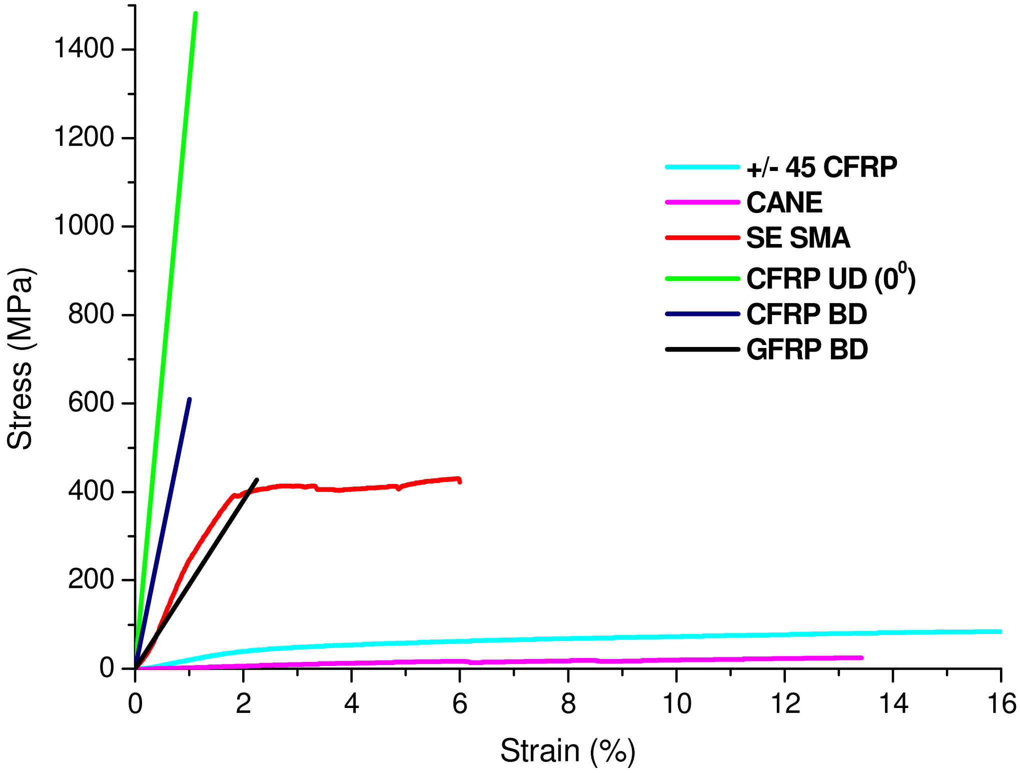

Fig.7.6: Comparison of CFRP in different orientations along with SE SMA & cane.

capability of the ± 45 deg. oriented FRP needs to be examined for the development of large deformation structural members like the arch of the landing gear which can be expended after one time use. The naturally occurring cane (plant material), which is used as a reinforcing core in the arch of the landing gear, has also been subjected to tensile testing. The tensile strength was as low as 15 MPa (approx), although the failure strains were large exceeding 10%. This is used as reinforcement for the arch to provide both bending and shear stiffness. The failure of the cane was in the form of peeling out in the form of concentric cylinders. This was actually a case of failure due to shear between the concentric layers. However further discussions regarding the failures of both the ± 45 deg oriented CFRP and cane is outside the purview of this thesis.

7.4. Design and Testing of Dog Ears:

The dog-ears are used to tie the landing gear and other structural members to the envelope. Fig 1.2 shows the schematic of the different dog-ear locations on the RC Blimp. The dog ears are made of polyurethane (PU) coated nylon fabric and they have been stitched in different configurations as shown in Fig.2.7. The dog-ears are bonded to the envelope and they are used to tie the skid to the envelope and also the rings to the envelope. The dog-ears that are used to tie the skid to the envelope resist the vertically acting downward static and inertial loads due to engine, engine mount and other engine accessories as well as the weight of the skid itself. They are located at different positions along the length of the skid as shown in Fig 1.11. Likewise the dog-ears that are used to tie the rings to the envelope serve the purpose of transferring the thrust developed by the engine to the envelope. They are located all along the circumference of the ring as shown. Table.7.3 shows some of the important design loads for the dog-ears which are arrived at based on the loads generated by the thrust of the engine, the weight of the engine and other sub-systems. The factor of safety (F.O.S) is arrived at based on the acceleration levels the different sub-systems are subjected to. The purpose of testing the dog ear is to determine the maximum load carrying capacity of different configuration of dog ears for vertically acting downward load, horizontally acting thrust loads and guy wire lift loads. Based on the tests the different configurations of the dog-ears are selected and the number of dog-ears is finalized. Table.7.4 summarizes the results of testing the different of dog-ears; type a-d. Based on the results of the testing the sizing of the dog ears is done.

Table.7.3: Assumed loads for dog ear design for RC blimp.

Sl No.	Loads	Force (N)	F.O.S.	Design Loads (N)
1.	Thrust	600	2	1200
2.	Engine and accessories	600	3	1800
3	Fin Load	250	2	500
4	Guy wire Loading	300	2	600

Table.7.4: Dog-ear testing results; initial yield and ultimate failure load.

Type	(Initial Yield/Debond/Tear) Load (N)	Ultimate failure load (N)
A	450	650
B	400	1250
C	600	950
D	600	850

7.5. Fabrication:

The landing gear is made of composite material such as carbon fiber reinforced composite (CFRP), glass fiber reinforced composite (GFRP), cane and SE SMA. The fabrication of the landing gear is done using wet lay-up technique with LY-5210 resin and HY-932 hardener as already stated.

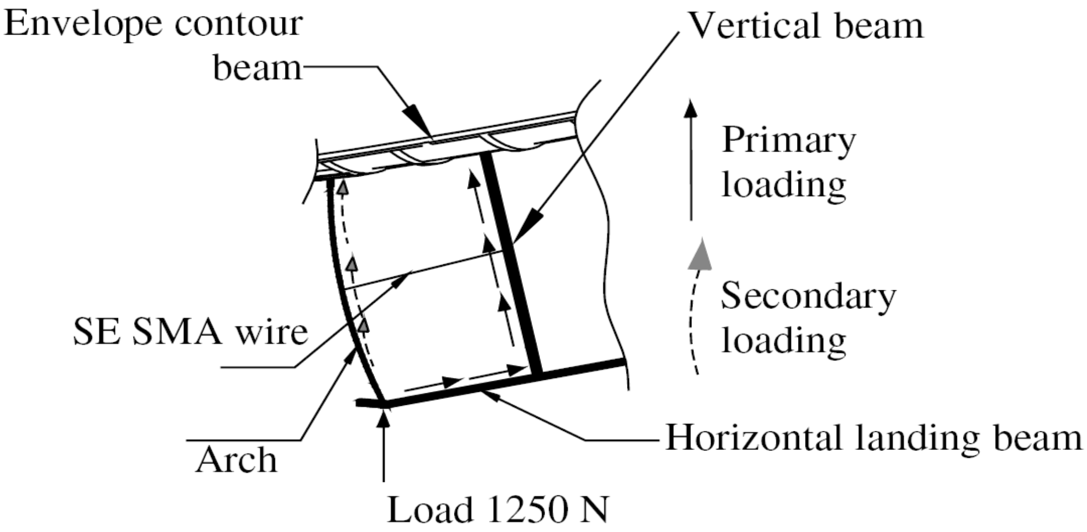

Fig.7.8: Enlarged view of subunit containing arch, landing beam and vertical beam.

Fig.7.8 is an enlarged view of the landing gear sub unit comprising of an arch, a horizontal landing tubular beam, a vertical tubular beam and part of the airship envelope contour beam. Fig.7.9 shows the details of landing beam where l-m refers to the arch and m-n-o to the segment of the landing beam, which first sees the impact. The thickness of the segment is minimum (and of constant value) in the range m – n and is varying from n (section B-B) to o with maximum at o (section C-C) as shown. Figs.7.10 a-d shows the tooling and assembly of the beams. The arch cross section (Fig.7.11 (a)) shows the thin CFRP layer wrapped around the cane, which is the core (as well as the structural reinforcing element for the arch).

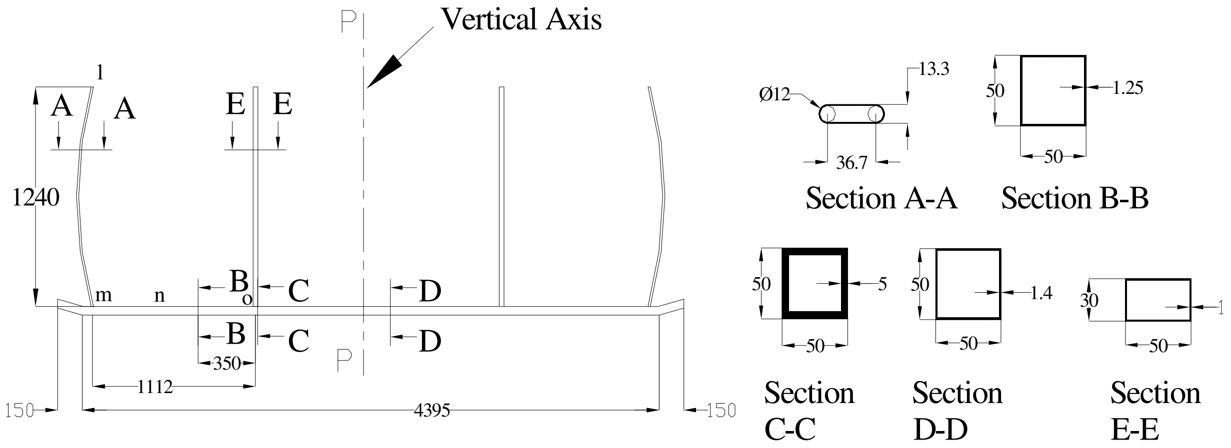

Section A-A Section B-B

Section C-C Section D-D Section E-E

Fig.7.9: Details of landing gear.

After several trials of different combinations, the natural cane material wrapped with CFRP B.D fabric proved to be the satisfactory choice meeting the requirement of adequate elastic deformations and minimum weight. The sub-unit comprises of vertical and horizontal CFRP tubes and arch. Fig 7.9 shows the vertical and horizontal tubes, which are of square section. The tubes and arch are made of wet layup with the resin system described earlier. Fig.7.10 (a), (b) & (c) shows the thermocol cores and matched die wooden outside tooling used for the fabrication of the tubes. The horizontal landing beam is stepped. Therefore as shown in Fig.7.10 the thermocol core is suitably stepped using a wire-cutting machine.

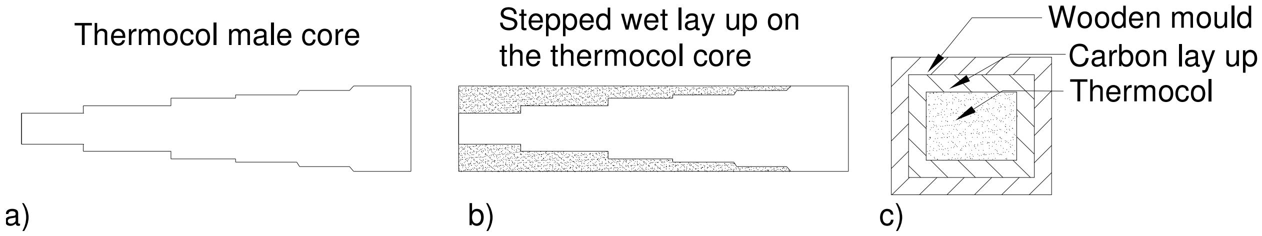

Fig.7.10: (a) Male thermocol core, (b) Stepped carbon wet layup on thermocol male core, (c) Assembly of wooden mould, carbon layup & thermocol.

Fig. 7.10 (d) shows the exploded view of the BD carbon wet layup for one longitudinal half of the stepped landing beam. The 0^o warp is along the length of the beam and 90^o weft is in the perpendicular direction to the beam.

Fig.7.10 (d): Exploded view of one half of the stepped landing beam lay up.

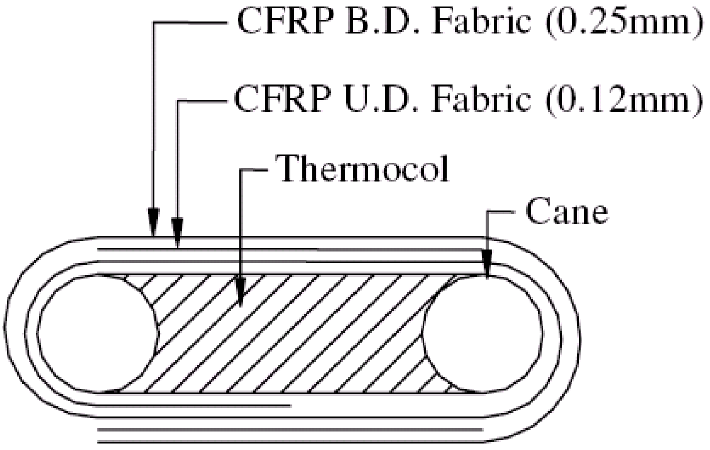

Fig.7.11 (a) Cross-sectional view of arch.

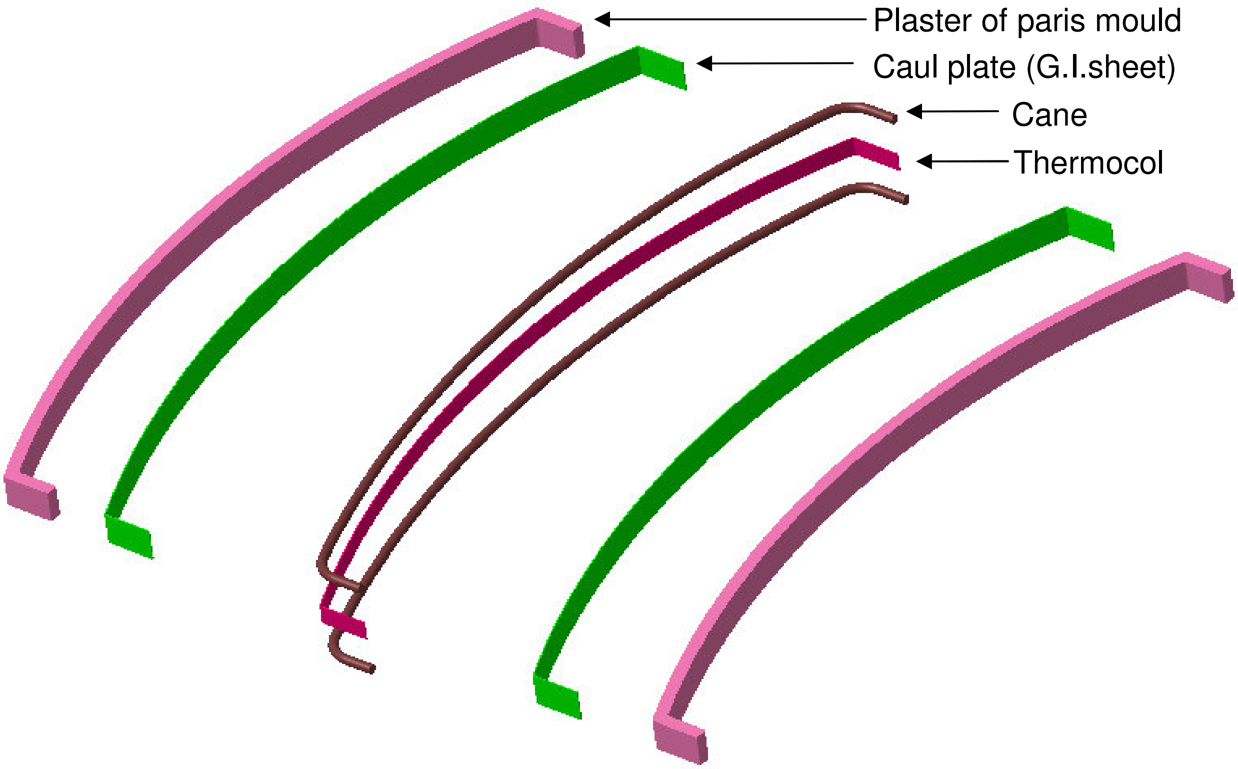

Fig.7.11 (b) Exploded view of the different components of the arch.

Fig.7.11 (c) Assembled view of the different components of the arch.

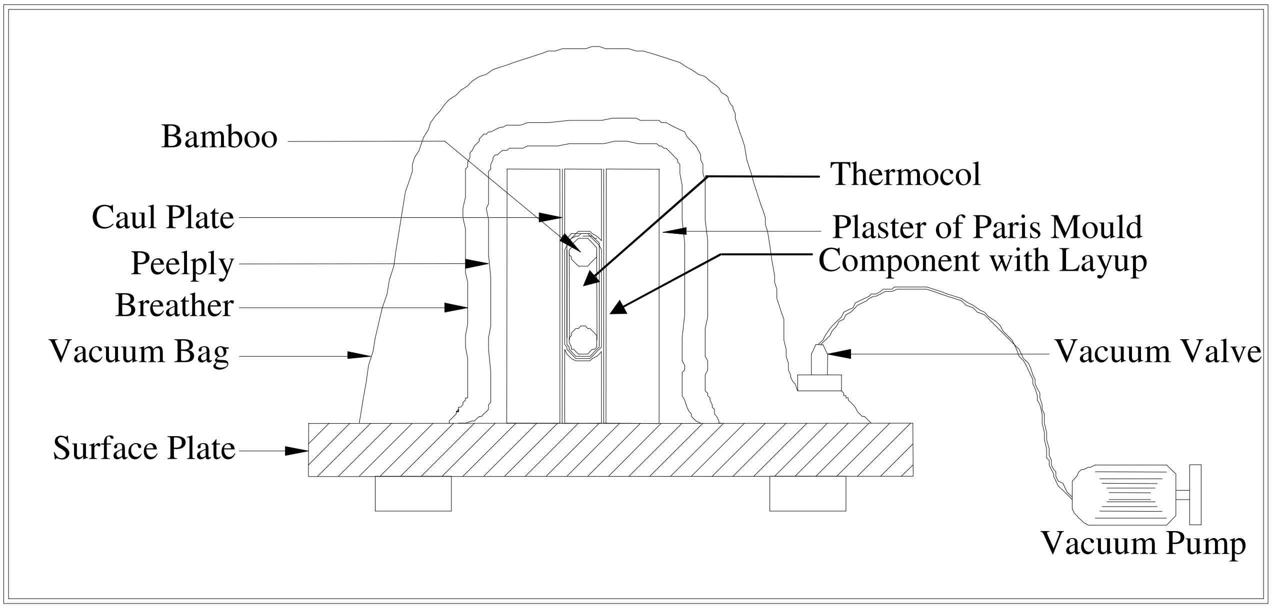

Fig.7.12: Fabrication setup of arch under vacuum.

The fabrication of the arch was done as follows; first the cane which is a naturally occurring plant material having a low young's modulus was shaped and bent to the required profile. Fig 7.11 (a) shows the thermocol used as a spacer between the cane cores. The thermocol and cane together constitute the male core for the arch. The layup consists of B.D wet fabric and pre-cured U.D fabric which is wound around the male core as shown. The layup with the male core is sandwiched between two G.I sheets, which serve as caul plates. Fig.7.11 (b) is the exploded view of the part and tooling which shows plaster of paris moulds on either side of the caul plate. Fig.7.12 is a schematic of the entire assembly that is placed in a vacuum bag with vacuum pressure of about 1 bar applied for 24 hrs to cure the part.

7.6. Energy Dissipation process in Landing Gear:

The landing gear is designed to have two load paths. Fig 7.8 denotes these two load paths viz; primary (vertical and horizontal landing beam) and secondary (curved arch and SMA) . As the landing gear sees the impact (loading) the arch buckles elastically and curves outwards because of the geometry shown in Fig.7.8. As it curves outwards it forces the SE SMA into a tensile mode of deformation. Immediately after the impact the arch regains its original shape (unloading) and the SMA gets back to its original undeformed position. During the process of loading and unloading the SE SMA dissipates the impact energy in the form of heat. Fig.7.13 (a) – (d) illustrates the sequence of the energy dissipation process in the landing gear sub-unit. The position of the tracer (filled circle) indicates the stress – strain level at different times. For the purpose of clarity, it is assumed that the impact-loading consists of four events (E1 – E4). As is clear from the Fig. 7.13 (a), at E1, the super elastic SMA is placed in the arch such that the strain level is about 0.5 % (given pre-strain) and the stress level is around

100 MPa i.e., the initial stress-strain position is just below the unloading stress. At E2 when the impact event takes place the stress reaches a value that is close to the super elastic plateau stress of about 400 MPa. The corresponding strain level is over 1%. At E3, the super elastic strain level of nearly 6% is reached, at more or less a constant value of plateau stress, along with a corresponding 'large elastic' deformation of the CFRP arch. At E4, the unloading of the SMA takes place, which is simultaneous with the recoil of the landing gear. The austenite gets converted to martensite while undergoing the large super elastic strain (loading plateau) and gets re-converted to austenite while undergoing the large super elastic strain recovery (unloading plateau). The unloading plateau stress is also referred to as the recoil stress and the recoil takes place at a relatively much lower value of stress. This feature enhances the stability characteristics of the vehicle during the recoil period. The events 2 and 3 together constitute the process of energy dissipation and elastic recoil in the landing gear sub-unit. In total there are 4 such sub-units in the landing gear, 2 sub-units in the front and two in the rear as shown in Fig.7.3. For the testing and analysis only one sub-unit (comprising of an arch, SMA element and a landing beam) is considered. The testing and analysis has not been done on the whole landing gear.

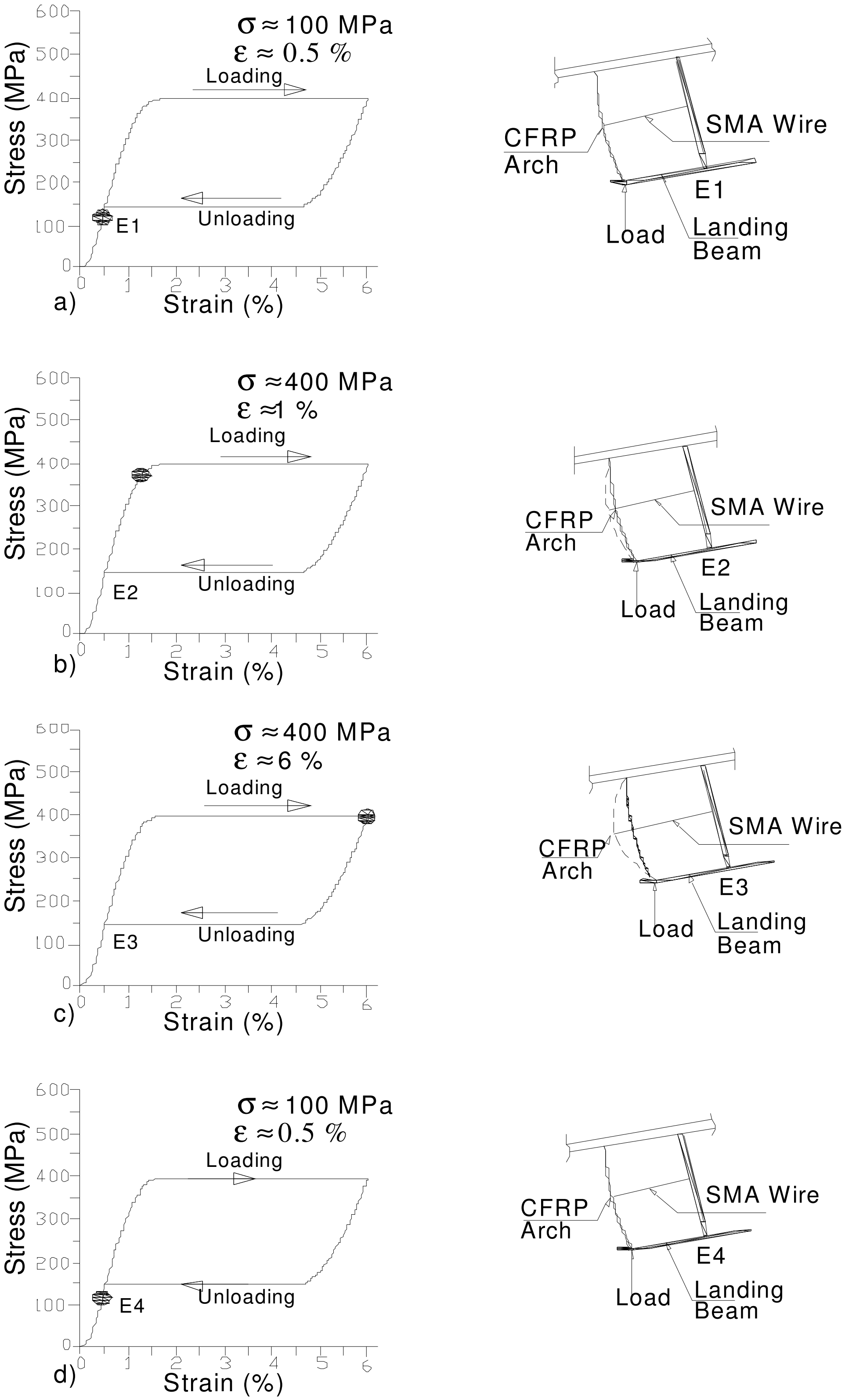

Fig.7.13: Sequence of energy dissipation in landing gear illustrated through events ‘a’ to ‘d’.

7.7: Design and Analysis:

The landing gear system comprising of beam, arch and SMA is designed to cater for the requirement of high-energy absorption and dissipation during landing. As mentioned earlier the landing gear design provides two load paths for reacting the impact loads; the primary and the secondary. The material used for the sub-unit comprising of arch and landing beam is primarily carbon/epoxy bi-directional fabric and the fabrication method is wet lay up. A small amount of cured UD prepreg layer is bonded with the arch. The reinforcement for the arch is naturally occurring cane. The core is generally required only to provide the shear stiffness. However, here since the arch has to undergo large elastic deformations the core has to possess both shear and longitudinal bending stiffness. Being a highly fibrous material having low density the cane was chosen here as the reinforcing core. The cane enables the arch to undergo large elastic deformation. The lay up that is wound round the thermocol core is generally orthotropic in nature with the warp being in the 0° direction and weft in the 90° direction. As seen in Fig.7.5 the strain characteristics of CFRP differ significantly from the SE SMA and naturally occurring cane material. As the geometry (Fig. 7.8) clearly shows, the arch by virtue of its shape and material composition can undergo large elastic deformation. The combined system (comprising of arch, horizontal landing beam and SMA) exhibits primarily geometrical non-linear behavior. In order to realize the smart landing gear with energy dissipation features the design and FE analysis approach that was adopted is presented here. Modeling a geometrically non-linear system with classical methods is not feasible. This is because in the classical method, the assumption is that the structure is in the linear elastic regime. It is assumed that the structure undergoes only small deflections. The classical solutions for large deflection behavior are quite complex. Therefore the analysis of the landing gear system is addressed through finite element (FE) methods. However, during the preliminary design stage the sizing of the arch and beam was done based on classical strength of materials approach. In order to simplify the analysis during this stage the arch and the beam were considered separately. The sizing of the two components was based on the assumed load-sharing requirement and their individual deflections were computed.

In the landing gear, the nonlinear behavior is primarily due to the geometric nonlinearity associated with the arch and the SE SMA. In the FE analysis the arch and beam are modeled with the beam elements (CBEAM) and the SMA wire is modeled with the CELAS element in NASTRAN. The beam consists of 15 elements, the arch consists of 20 elements and the SMA wire is modeled with 1 element. Preliminary convergence studies were done before finalizing the FE model. The beam cross section is modeled as a hollow stepped beam of maximum dimension 50 x 50 mm and as a bidirectional CFRP material with $[0 / 90^\circ]$ orientation. An equivalent modulus of 30GPa obtained from tests conducted on specimens cut from actual test component is used. It may be noted that the modulus obtained here is lower than that reported in Table 7.2 and that normally found in published literature for CFRP and GFRP material. The reduction in modulus can be attributed to factors such as fabrication process, deviation in fiber orientation, environmental effects, and so on. The arch which contains CFRP wound around the cane material as shown in Fig.7.11 (a) is modeled as an equivalent rectangular cross section of 50 x 13.3 x 1.2 mm. A modulus of 14GPa is used for the arch section in the analysis. The SMA behavior is modeled in a simplified bilinear way. In the FE model the beam end is (constrained of all translations and rotation) given a 'fixed' boundary condition. The upper end of the arch is given a hinged condition. This way the arch closely simulates the real structure.

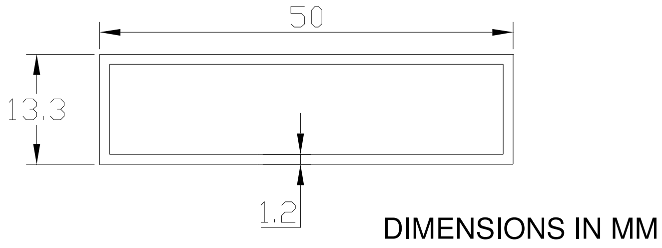

Fig.7.14: Equivalent section of arch used in FE model

Fig 7.14 shows the area of the equivalent arch section that is adopted through the rule of mixtures considering the areas and moduli of both cane and CFRP layers wound over the cane section.

Fig.7.15 shows the SMA behavior modeled as a bi-linear spring element having stiffness K_1 and K_2.

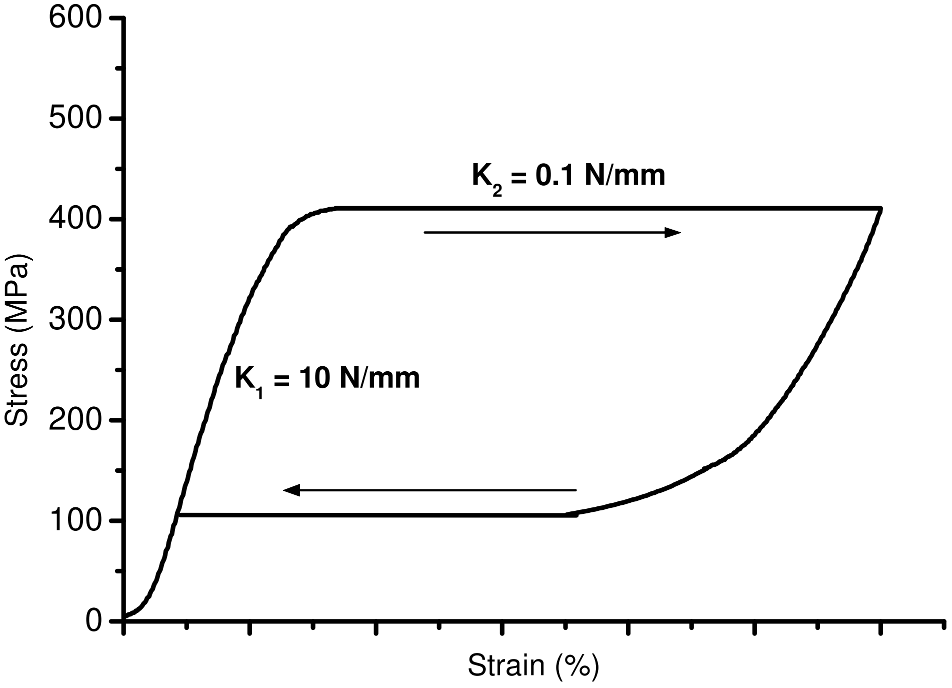

Fig.7.15: Equivalent SMA bi-linear spring stiffness for FE model.

The elastic deformation of the austenite (segment 1) is given a stiffness value K_1=10N/mm and the plateau region (segment 2) a stiffness value K_2=0.1N/mm.

Fig.7.16 shows the important stages in the design and analysis process. The procedure followed in the design and FE analysis is as follows:

1. First the curved arch containing natural cane and CFRP was analyzed.
2. Next the curved arch was integrated with the beam of constant cross-section.
3. The beam was configured as a stepped member.
4. The SMA was integrated with the stepped beam and the curved arch.

For the analysis of the arch, the section considered was rectangular as shown in Fig.7.14 from bending considerations. This was analyzed for different moduli

Figure	Total load (N)	Young's modulus (GPa)	Deflection, δ_v, (mm)
a) 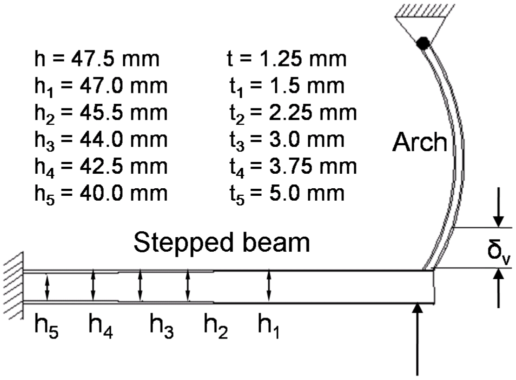	1000	Arch = 14 Beam = 30	41.9
b) 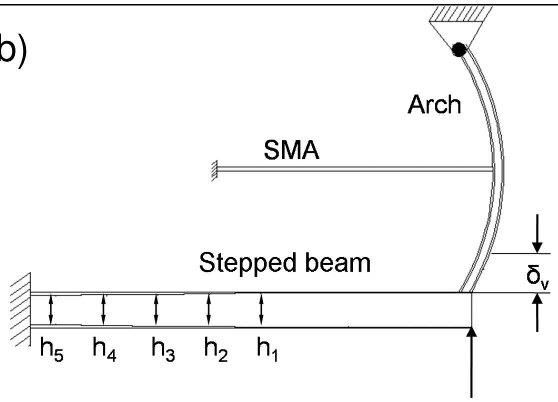	1250	Arch = 14 Beam = 30	42.1

Fig.7.16: Stages in the analysis and design process –analysis results

corresponding to the different materials viz; CFRP and GFRP. For the same maximum stress values, the weight of GFRP was higher. Therefore, it was decided to use CFRP.

In order to address the problem of achieving large elastic deformations, the curved shape of the arch was considered to enhance the elastic deformations. The curved arch was first integrated with the beam of constant cross-section. Given the high stiffness and limited strain capability of carbon composites the elastic deformations (i.e. vertical deflections at the impact point) were grossly inadequate and there was little energy dissipation. In view of this, as shown in Fig. 7.16 (a) it was decided to have a stepped CFRP beam which can give larger vertical tip deflections. With the stepped beam (where ‘h’ represents the depth of the rectangular beam cross section and‘t’ represents the CFRP lay up thickness) a revised analysis was carried out. There was an improvement in the elastic deformation at the impact point but the arch was not sufficiently stiff and the maximum load it could withstand was limited to 1000N. Also the configuration of Fig.7.16 (a) did not meet the energy dissipation considerations (as there is no hysteresis involved between the loading and unloading for the CFRP material).

From the above studies it was clear that a smart material such as SMA with large recoverable elastic deformations, which can stiffen the arch such that the arch could withstand a higher load of 1250 N and possess high-energy dissipation capabilities, had to be used. Fig.7.16 (b) shows the results of analysis for the configuration integrating SMA, curved arch and stepped beam. It is clear that the SMA substantially increases the load carrying capacity of the landing gear sub unit while retaining the elastic deformations. Introducing the super elastic SMA wire in the geometrically non-linear system substantially enhances the energy absorbing and dissipating capability of the system. The SMA wire will, during its deformation stiffen the arch and increase the load carrying capacity of the arch considerably. The SMA is a non-linear elastic material. However in the analysis, which has been done only for the loading part the SMA behavior is simplified as a bilinear element.

7.8: Testing of the smart Landing gear:

The testing of the landing gear sub-unit was carried out for 3 configurations. Table.7.5 summarizes the results of the tests for the three different configurations.Fig.2.4 shows the configuration of the landing gear. Fig. 2.5 shows the experimental set up for

Table.7.5: Summary of experimental results (deflection)

Parameter	C1	C2	C3
Maximum vertical load (N)	1250	1000	1200
δ_h at 1000N load (mm)	40	51	11.5
δ_v at 1000N load (mm)	37	42	20
δ_h at 1200N load (mm)	51	———	15.5
δ_v at 1200N load (mm)	45	———	25
δ_h at 1250N load (mm)	55	———	———
δ_v at 1250N load (mm)	49	———	———

C1: configuration 1 (with SMA); C2: configuration 2 (without SMA);
C3: configuration 3 (with steel wire).

the arch and landing beam segment incorporating the SMA element. The following aspects of the landing gear are elaborated:

i) The combined benefit of CFRP beam, natural cane reinforced CFRP arch & SMA.

ii) The comparison of SMA wire with a steel wire for energy dissipation.

As already discussed the experiments are done for three configurations, namely C1, C2 & C3. Tests conducted on the arch and the arch-SMA combinations have shown a nearly nonlinear load-deflection pattern which is generally in agreement with the analysis prediction. Before going into the details of the testing it is necessary to compare the stress-strain characteristics of the SMA wire and the stainless steel wire.

Fig.7.17 shows the comparison of the super elastic SMA and stainless steel (S.S) wire.

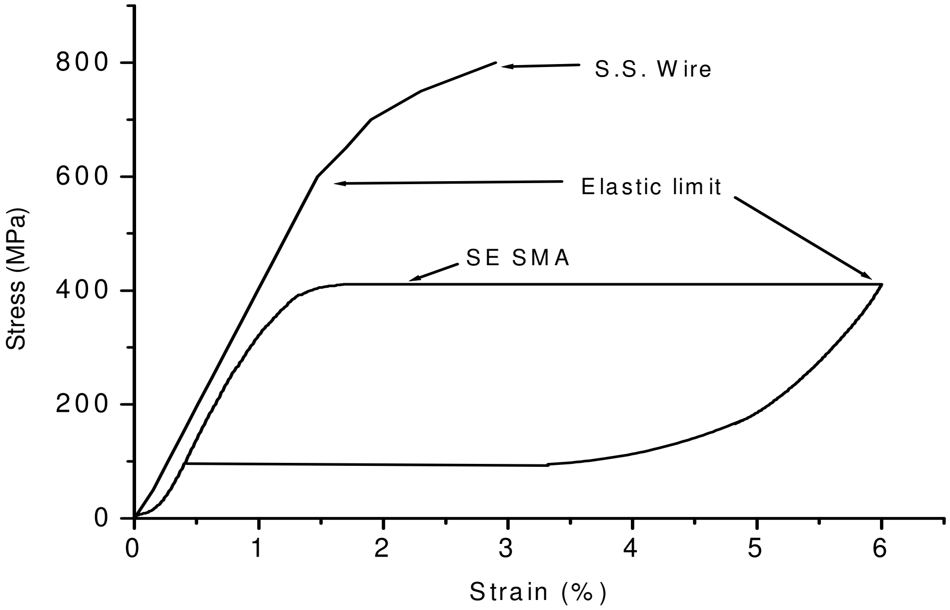

Fig.7.17: Comparison of super elastic SMA and stainless steel (S.S) wire.

If on the other hand a steel wire of identical diameter as SMA element is used in the landing gear, then, since the maximum elastic deformation of the steel element is less than 2% (as opposed to 6 – 8 % for the superelastic SMA) and the modulus is far higher than the super elastic SMA, therefore the compliance of the landing gear sub-unit will be quite different from the case of using SMA wire. Also, the more important aspect is that in the elastic region an identical mass of the steel wire will dissipate very little energy compared to the super elastic SMA element during the loading – unloading cycle.

The characteristics of the steel wire will affect not only the load sharing between the arch and the beam but also the magnitude of the elastic deformation of the landing gear unit (i.e. the deformations will be far less than desired and therefore the energy dissipated will also be very low). Also, the steel wire does not possess sensory characteristics like the super elastic SMA described earlier. In order to validate the design concept, a steel wire of identical dimensions as that of SMA wire was used in the experiment and the sub-unit was loaded up to 1200 N. This case is referred to as configuration 3. The loading was stopped at 1200 N as signs of failure were noticed (i.e. some unusual acoustic activity was observed). The focus of the testing as well as analysis is on the vertical deflection of the sub-unit and loading sharing of the arch, beam and SMA element. Figs.7.18 and 7.19 give the comparison of load vs. vertical

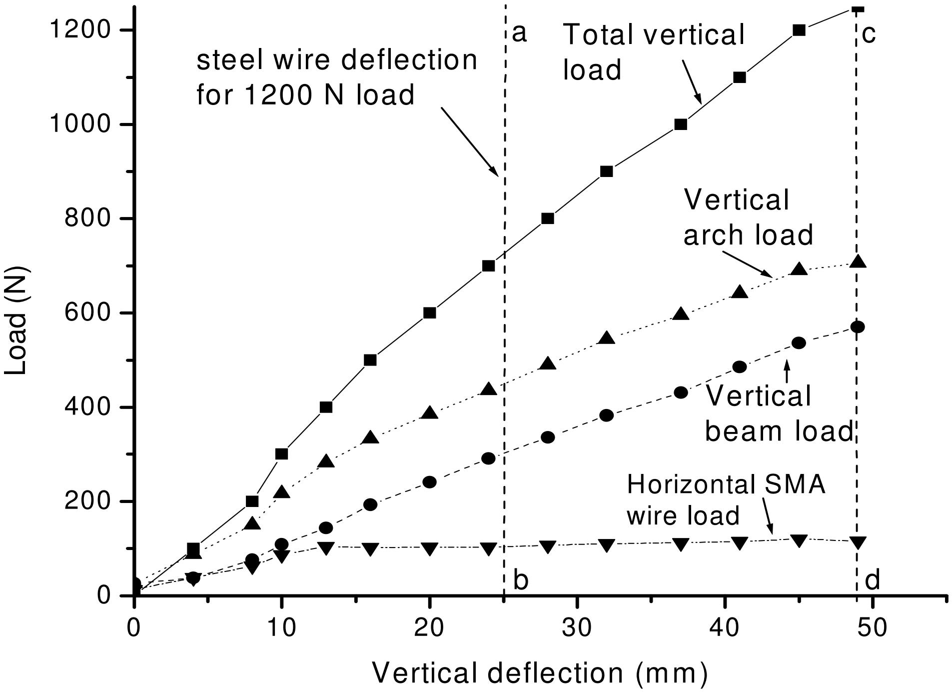

Fig.7.18: Load vs vertical deflection for C1.

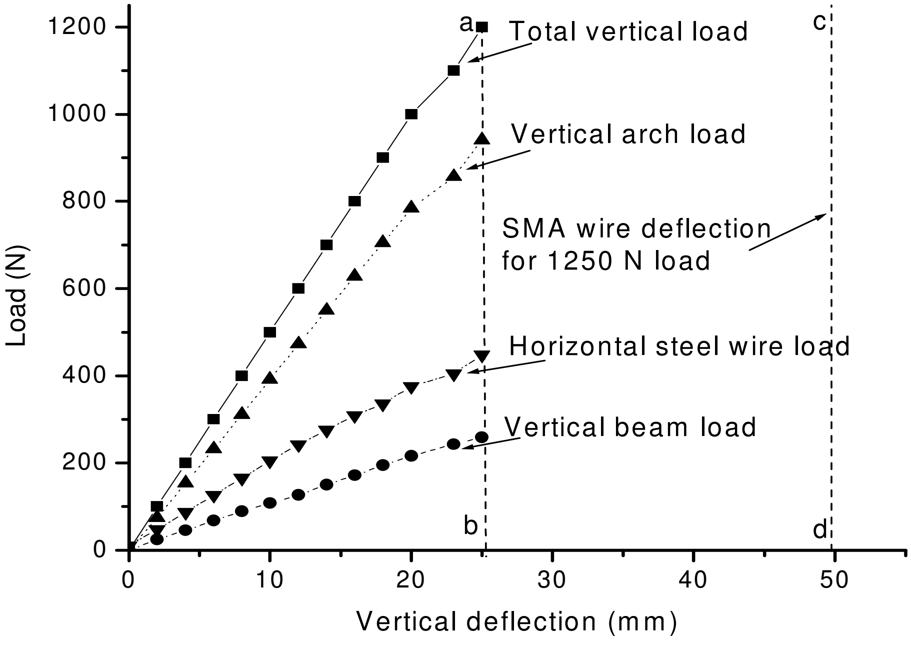

Fig.7.19: Load vs vertical deflection for C3.

deflection for the subunit using SMA (C1) and steel wire (C3) for the testing. In these figures the different load parameters are related as follows: ‘Total vertical load = Vertical arch load + Vertical beam load’. (As shown in Fig. 2.5 the load cell 1 monitors the total vertical load, load cell 2 monitors the vertical arch load and load cell 3 monitors the horizontal SMA load). The dotted line ‘ab’ in these figures indicates the maximum vertical deflection for the configuration C3 where a steel wire is used. Likewise ‘cd’ indicates the maximum vertical deflection for the configuration C1 where an SMA wire is used. From Fig. 7.18, it is clear that for C1 for a total vertical load of 1250 N the vertical deflection is 49 mm and the arch takes about 55% of the total load. In contrast as is evident from Fig. 7.19, for C3 when the steel wire is fixed in place of SMA, owing to its higher modulus (and limited strain capability) the steel wire stiffens the arch and therefore the arch takes a much higher load of about 85% of the total load (over 30% higher). The elastic deformation is however nearly 50 % less than configuration 1(i.e. with the SMA element). Therefore, a steel wire (replacing SMA) cannot ensure the desired ‘large elastic’ deformation (and in the process energy dissipation) of the landing gear sub-unit. We have also seen from analytical studies discussed earlier that though a helical steel spring (replacing SMA element) can give a deflection identical to that of configuration 1 the weight of resulting landing gear is far too high. (Refer Table 7.1).

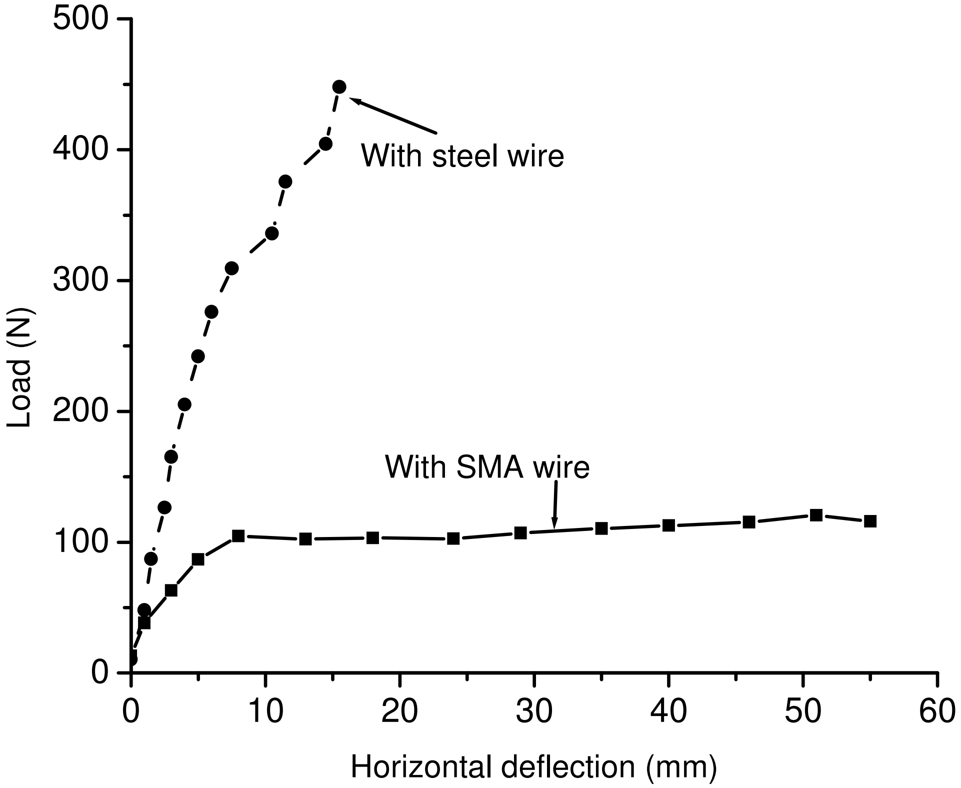

Fig.7.20: Load vs horizontal deflection for stainless steel and SMA wire (From C1 and C3)

Fig.7.20 shows the test results of load vs horizontal deflection for stainless steel and SMA materials in the sub-unit for the loading part. The behavior closely approximates the bilinear model for SMA assumed in Fig. 7.16. The SMA has a substantial plateau region which corresponds to the deformation between the events t = 1 and t = 2 sec. described in Fig. 7.13. The plateau region of the SMA ensures required compliance between the arch and SMA as the sub-unit is vertically loaded. This contributes to the higher load withstanding capability of C1 configuration.

7.9: Comparison of analysis and testing:

Figs.7.21 and 7.22 show the comparison of experimental result of testing (i.e. considering the total vertical load) and non linear analysis (NLA) for configurations C1 (with SMA) and C2 (without SMA) respectively.

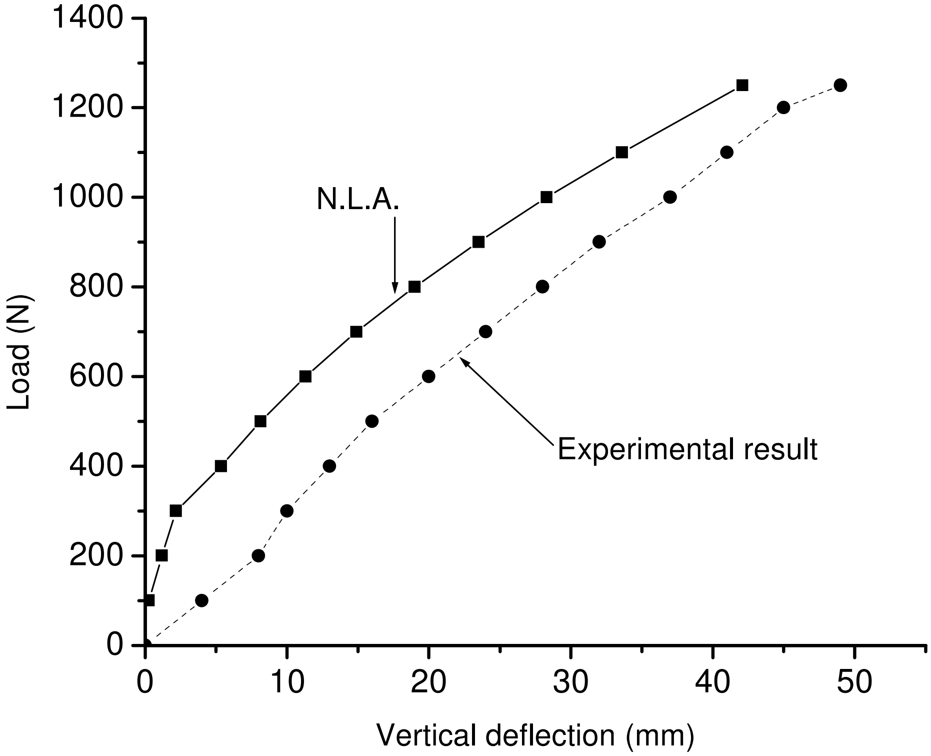

Fig.7.21: Comparison of N.L.A and experimental result; load vs vertical deflection (δ_v) for C1.

The analysis results are not presented for the C3 configuration (with steel wire) as it is very clear from section 7.8 that this configuration is unsuitable as it does not meet the energy dissipation requirements of the landing gear. The NLA captures the geometric non-linearity of the landing gear structure reasonably well. The focus of the testing as well as analysis is on the vertical deflection of the sub-unit and loading sharing of the arch and beam. The co-relation between analysis and experiment is good. For configuration 2, the test had to be stopped at 1000 N load, as there were indications of CFRP failure in compression on the inner surface of the arch. This was confirmed by the acoustic emissions, which were audible.

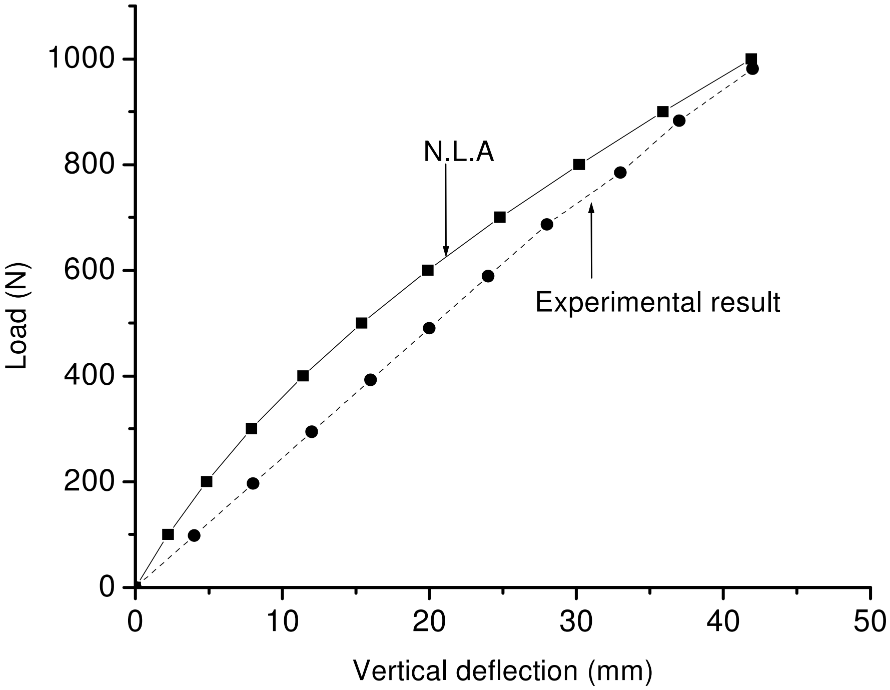

Fig.7.22: Comparison of N.L.A and experimental result; load vs vertical deflection (δ_v) for C2.

Therefore the results are first compared at 1000N for configurations C1 and C2. As seen in Table 7.6 the analysis prediction of the load sharing for both configurations is generally in agreement with the testing results. From the testing it is seen that the load taken by the SMA stiffened arch for C1 is 58 % of the total load of 1000N while undergoing a vertical deflection of 37 mm. For the test configuration C2 without SMA at a load of 1000N the vertical deflection was 42 mm and the load taken by arch was 50% of the total load. The results clearly indicate that the arch is getting stiffer when the SMA element is attached to it. The arch is able to share a higher load and thereby the total load carrying capacity of the landing gear increases. Due to the stiffening effect provided by the SMA it was possible to increase the loading on the sub-unit to the maximum design value of 1250 N. Here again, the prediction of the analysis regarding the load sharing is in agreement with the testing. The analysis however shows a marginally lower value of deflection compared to the testing. Table.7.6 gives the summary of the comparison of analysis and testing relating to Figs. 7.21 and 7.22.

Table.7.6: Summary of load sharing between arch, beam, and SMA.

Load Case	Total load (N)		Load sharing (N)				Deflection (mm)	
	Testing	Analysis	Testing		Analysis		Testing	Analysis
			Arch	Beam	Arch	Beam	δ_v	δ_v
C1	1250	1250	680	570	690	560	49	42.1
C1	1000	1000	580	420	618	382	37	27.2
C2	1000	1000	503	497	479	521	42	41.9

C1: configuration 1 (beam, arch and SMA); C2: configurations 2 (beam and arch), The total elastic vertical deflection δ_v of landing gear for configuration C2 i.e. without SMA is 42 mm (corresponding to a maximum load of 1000 N). This vertical deflection increases to 49 mm for configuration C1 i.e. with SMA (corresponding to a maximum total load of 1250 N).

As stated above the analysis gives lower value of deflections for both configurations C1 and C2. The modulus that is taken as the input from experiment is constant for the entire structure in the analysis. However, in reality the modulus does change from zone to zone within the structure due to process deficiencies and/or deviations in layer orientations. Therefore the experiment is bound to give a larger value of deflection compared to the analysis. The difference between analysis and experiment is more pronounced for the C1 configuration with SMA. This is due to the fact that the actual SMA behaviour (which has been approximated as bilinear) is not completely captured by the FE analysis. For the C2 configuration without SMA also the analysis generally indicates lower values of deflection compared to the experiment. There is relatively much better agreement between the analysis and experiment for this configuration. Therefore the FE analysis is able to capture the behavior of the structure better when the SMA is not integrated. At the maximum load of 1000 N for this configuration, the almost identical deflection values of the experiment and analysis as seen in Fig. 7.22 is purely coincidental.

In the smart landing gear the landing beam segment weighs about 5.11 N and the arch weighs about 4.4 N but the SMA weighs only about 0.05 N. A small amount of SMA suitably placed (0.5% of the total weight of the sub unit) as in configuration 1 results in an increase of total load carrying capacity of the sub unit by about 25% and increases the vertical elastic deformations by about 20%. This clearly establishes the energy dissipating super elastic character of the SMA element while it (SMA) undergoes an elastic deformation of more than 4% and dissipates energy. These characteristics ensure the desired soft landing for such types of vehicles. As can be seen from Table 7.6, there is good correlation between analysis and experiment for both the configurations i.e. with and without SMA. With SMA element the maximum load carrying capacity increased from 1000 to 1250 N. It can be seen that for the configuration 1, the arch along with SMA is taking slightly more than 50% of the total load i.e. 680 N of the total 1250 N. It has to be pointed out that both the testing and analysis indicate roughly 50% of the total load going to the arch and SMA combination and 50% to the beam. In other words the primary load path and the secondary load path share the load equally. This type of load sharing is central to the design philosophy of the landing gear as discussed earlier. It is important to point out that the sensory information from the SMA discussed in chapter 4 does not in any way improve the performance of the landing gear and is used only to validate the design.

The work presented in this chapter is summarized as follows: Advanced polymeric composites (carbon and glass) in different orientations have been tested for the tensile and in-plane shear properties. The properties which are of interest are; ultimate tensile strength, ultimate tensile strain, modulus of elasticity and poisson's ratio. Polymeric composites, naturally occurring cane and SE SMAs are materials with diverse mechanical properties. These have been effectively integrated based on a novel design philosophy. Central to the novel landing gear design incorporating polymeric carbon composites and Ni Ti SE SMA is the provision of two load paths; the primary and the secondary. The primary load path is stiff and undergoes very small elastic deformations. The secondary load path is more flexible [consisting of the curved arch (made of cane with CFRP wrapping) and SE SMA element] and undergoes elastic (buckling) large deformations and in the process dissipates large quantities of energy. The secondary load path members are expended after a certain fixed number of cycles. The sizing of the arch and landing beam in the smart landing gear is done in such a way as to meet the dual requirements of low weight and high energy dissipation while undergoing 'large elastic' (large non-linear recoverable elastic strain) deformations in order to ensure soft landings when the airship impacts the ground. The inherently large energy dissipating character of the super elastic SMA element in the tensile mode of deformation along with the superior elastic bounce back features of the SE SMA, arch landing beam configuration have provided the ideal solution. In order to address the unusually large deflections arising due to geometric non-linearity a non-linear analysis based on FEM approach has been used to analyze the structure.

The total elastic vertical deflection δ_v of landing gear for configuration C2 i.e. without SMA is 42 mm (corresponding to a maximum load of 1000 N). This vertical deflection increases to 49 mm for configuration C1 i.e. with SMA (corresponding to a maximum total load of 1250 N). In the smart landing gear the landing beam segment weighs about 5.11 N and the arch weighs about 4.4 N but the SMA weighs only about 0.05 N. A small amount of SMA suitably placed (0.5% of the total weight of the sub unit) as in configuration 1 results in an increase of total load carrying capacity of the sub unit by about 25% and increases the vertical elastic deformations by about 20%. This clearly establishes the energy dissipating super elastic character of the SMA element while it (SMA) undergoes an elastic deformation of more than 4% and dissipates energy.

An SE SMA incorporated polymeric carbon composite smart landing gear which not only ensures soft landings but also possesses substantial crashworthy features has thus been successfully demonstrated.

Chapter 8: Conclusions

The investigations pertaining to "NiTi Super Elastic Shape Memory Alloys for Energy Dissipation in Smart Systems for Aerospace Applications" has tried to address the whole gamut of issues covering heat treatments, sensory property evaluation, strain rate effects, cyclic and fatigue behaviour of the material. After addressing these issues the NiTi material has been successfully integrated into the polymeric composite smart landing gear for aerospace applications.

The heat treatment given to the SE SMA materials hold the key to the control of their mechanical properties, in particular the energy dissipation in the present context. The wires heat treated at different temperatures have also been compared in relation to the optimum plateau stresses, energy dissipation and residual strain characteristics.

The sensory function of SE SMA is associated with the energy dissipation characteristics. The sensory function has been evaluated by passing a small constant current in the SE SMA and the voltage has been measured across the SMA element as it undergoes super elastic strain.

The SE SMA element that is used in the landing gear is subject to a wide range of strain rates. Tensile tests up to failure for different strain rates from 0.2 to 800%/min have been carried out. The temperatures have been varied from -50 to + 100 ^{0}C. Some limited fractography studies on cold worked and a few selected heat-treated specimens after tensile testing have been carried out.

The cyclic tests presented in this work deal with the cyclic strain amplitudes of 6 and 8 % respectively within the elastic regime for the SE SMA. One set of experiments involve determining the strain amplitude at which the energy dissipation is maximum with minimum permanent set in the material after the first cycle. The second set of experiments involves strain controlled cycling up to 100 cycles and studying the evolution of energy dissipation and plastic strain parameters.

The stress-strain cyclic fatigue loading involving very large strains in the high stress regime has been carried out. The strain cycling was done at 1mm/sec on 30 mm length wires. The evolution of the plastic strain parameter is the key to predicting fatigue life. The plastic strain between consecutive cycles from different failure tests is taken and constants are derived. These constants are fit into the Coffin-Manson relationship for predicting the fatigue life.

Polymeric composites, naturally occurring cane and SE SMAs are materials with diverse mechanical properties. These have been effectively integrated based on a novel design philosophy. Central to the novel landing gear design incorporating polymeric carbon composites and Ni Ti SE SMA is the provision of two load paths; the primary and the secondary. The sizing of the arch and landing beam in the smart landing gear is done in such a way so as to meet the dual requirements of low weight and high energy dissipation while undergoing ‘large elastic’ deformations in order to ensure soft landings when the airship impacts the ground.

An SE SMA incorporated polymeric carbon composite smart landing gear which not only ensures soft landings but also possesses substantial crashworthy features has thus been successfully demonstrated.

Based on the above studies the following conclusions are made:

1. The NiTi SE SMA wire heat treated at 500 °C possesses the optimum energy dissipation characteristics for the landing gear application. The heat treatment imparted to the cold worked wire holds the key to the control of mechanical properties. It is clear that for a given superelastic NiTi SMA wire with a certain degree of cold work the heat treatments in a narrow range of 450 - 600 °C bring about a substantial change in the properties. The increase in ductility of a heat treated wire possessing the energy dissipation character can be as much as eight times compared to a cold worked wire. Similarly in this narrow range of heat treatments the dissipated energy in one complete cycle can vary by as much as 60%.
2. The utility of the sensory feedback to validate the design of the smart landing gear has been brought out. In summary, the sensory characteristics of the SE SMA as it dissipates energy have been brought out. Thus the bi-functionality of the smart material which in this case is the SE SMA has been established.
3. It is clear from these experiments that the NiTi SMA alloy possesses inherently ductile characteristics over a wide range of temperatures and strain rates. These include below martensite finish and above austenite finish temperatures. It also includes low (0.2%/min) as well as high (800%/min) strain rates. The energy dissipation E_d is high above the strain amplitude of 6 %. At lower strain amplitudes the amount of SIM formation is rather low as a substantial amount of loading strain is expended in the elastic deformation of the parent phase which

has no energy dissipation capability. This limits the energy dissipation at lower strain amplitudes. On the other hand at strain amplitudes beyond 6% the residual strain levels increase thus limiting the utility in SE SMA devices. It is also clear that the SIM formation response is dependent on the strain rate. The hysteresis and therefore the energy dissipation are also dependent on the strain rate. The energy dissipation in NiTi SE SMAs is large compared to conventional materials. As the strain rate increases the mean point shifts to the higher stress, higher strain regime. Also, from these studies, it is possible to deduce the optimum strain amplitudes and the optimum energy dissipation for the given range of strain rates. These results are useful inputs for the design of SE SMA incorporated devices.

4. In the elastic regime the cyclic strain amplitude of 6% at a strain rate of 30%/min gives good energy dissipation properties. The accumulated residual strain is within 1%. The 8% cyclic strain amplitude though has a higher level of energy dissipation; the accumulated residual strain is higher which adversely affect the fatigue life of the material. The stabilization of the energy dissipation property and residual strain takes place at the same number of cycles and is related to the same underlying mechanism. Beyond the stabilization the amount of permanently deformed martensite remains more or less constant for a relatively large number of cycles. These observations are important from the point of designing SE SMA devices. The implications for the design of SE SMA devices

in relation to strain amplitude, energy dissipation and energy dissipation are thus brought out.

5. The Coffin-Manson Law is a useful relationship to get an estimate of the fatigue life where large super elastic cyclic amplitudes are involved for NiTi thin wires. The plastic strain is a prominent parameter in modeling fatigue behavior.
6. The proposed landing gear design (incorporating polymeric composites, naturally occurring cane and SE SMAs) is of generic nature and provides an alternate method of developing an efficient (high energy dissipation with low system weight) landing gear with satisfactory geometry. The design provides two load paths to react the impact loads; the primary and the secondary. The primary load path is stiff and undergoes very little elastic deformation. The secondary load path, which is more flexible, takes a substantial amount of load and undergoes large elastic (buckling) deformations. The SE SMA is integrated effectively into the secondary load path and forced into a tensile mode of deformation during impact loading and in the process it absorbs/dissipates energy. This is another key aspect of the design. The elements of the primary load path are designed for low strain and large no. of cycles whereas the elements of the secondary load path are expendable after a relatively less number of cycles. This design applies for a “large class of vehicles” including aerospace vehicles (such as airships, rotorcraft and other light unmanned air vehicles). It can also be extended to the automobiles such as motorcycles, cars etc. to serve the purpose of energy dissipation during impact loadings. This design concept can be considered in

automobiles as an alternative to the existing shock absorbers and also in other impact zones. Currently the shock absorber systems in automobiles are part of one single load path. In the place of the single load path, the proposed design consisting of two or even more than two load paths can be experimentally examined. The concept of the two load paths can be extended to several designs. The central load path can be the primary one and there can be two secondary load paths incorporating SE SMA elements on either side of the primary load path that are symmetrically placed. It must be added that even without the SMA in the proposed design, the landing gear system can perform the function of energy absorption. The effective integration of a very tiny fraction (as a weight percentage) of the SE SMA in the secondary load path can however bring about a substantial benefit of several orders in the energy dissipation capability. As stated above this design approach can be extended to a large variety of vehicles.

References:

1 G.A. Khoury and J.D. Gillett, “Airship Technology,” Cambridge Univ. Press,

  a. Cambridge, England, U.K. (1999), Pg. 11.

2 R.M. Jones, Mechanics of Composite Materials, 2nd ed., Taylor and Francis. Inc., Philadelphia (1999), Pg.23.

3 M. M. Shokrieh and M.J. Omidi, “Tension behaviour of unidirectional glass/epoxy composites under different strain rates,” J. Comp. Struct. (2008) – In Press.

4 Taniguchi, Norihikio, Nishiwaki, Tsuyoshi, Kawada and Hiroyuki, “Experimental Characterization of Dynamic Tensile Strength in Unidirectional Carbon/Epoxy Composites,” J. Adv. Comp. Mater. 17 (2008), Pg.139-156.

5 K. Gliesche, T. Hubner and H. Orawetz, “Investigations of in-plane shear properties of ±45°-carbon/epoxy composites using tensile testing and optional deformation analysis,” J. Comp. Sci. Tech. 65 (2005), Pg.163-171.

6 W.V. Paepegem, I.D. Baere and J. Degrieck, “Modelling the nonlinear shear stress-strain response of glass fiber-reinforced composites, Part I : Experimental Results” J. Comp. Sci. Tech. 66 (2006), Pg.1455-1464.

7 S.H. Lee, H.Noguchi and S.K.Cheong “Static Behavior characteristics of Hybrid Composites with Nonwoven Carbon Tissue,” J. Comp. Mater. 37 (2003), Pg.233-252.

8 A. Godara and D. Raabe, “Influence of fiber orientation on global mechanical behaviour and mesoscale strain localization in short glass-fiber-reinforced epoxy polymer composite during tensile deformation investigated using digital image correlation,” J. Comp. Sci. Tech. 67 (2007), Pg.2417-2427.

9 T.P. Skourlis and R.L. McCullough, “The effect of temperature on behaviour of the interphase in polymeric composites,” J. Comp. Sci. Tech. 49 (1993), Pg.363-368.

10 K. Okubo, T. Fujii and Y. Yamamoto, “Development of bamboo-based polymer composites and their mechanical properties,” J. Comp. Struct. 35 (2005), Pg.377-383.

11 S. Banerjee, and K. Madangopal, “Shape Memory Effect,” J. Mat. Mater. Proc. 8 (1996), Pg.123-138.

12 L. Delaey, R.V. Krishnan, H. Tas and H. Warlimont , “Thermoelasticity, pseudo elasticity and the memory effects associated with martensitic transformations,Part 1 structural and microstructural changes associated with the transformations, ” J. Mater. Sci. 9 (1974), Pg.1521-1535.

13 R.V. Krishnan, L. Delaey, H. Tas, H. Warlimont, “Thermoplasticity, pseudo elasticity and the memory effects associated with martensitic transformations, Part2 The macroscopic mechanical behaviour,” J. Mater. Sci. 9 (1974), Pg.1536-1544.

14 K.A. Tsoi, R. Stalmans, J. Schrooten, M. Wevers and Y.W. Mai, “Impact damage behaviour of shape memory alloy composites,” Mater. Sci. Eng. A. 342 (2003), Pg.207-215.

15 P. Sittner, V. Michaud and J. Schrooten,“Modelling and material design of SMA polymer composites,” J. Mater. Trans. 43 (5) (2002), Pg.984-993.

16 P. Sittner, D. Vokoun, G.N. Dayananda, and R. Stalmans, “Recovery Stress generation in shape memory Ti50i, Ni45, Cu5 thin wires” J. Mater. Sci. Eng. A 286 (2000), Pg.298-311.

17 S. Jayasankar, G.N. Dayananda, M. Subba Rao, “Hybrid Composites for Morphing Applications'' XV NASAS Conference, Coimbatore, India (2007).

18 G.N. Dayananda, V. Shankar, M. Subba Rao and M.A. Farook, “Active Shape Control of an Aerofoil Using Shape Memory Alloys” Proceedings of the Third International Conference on Advances in Composites, ADCOMP-2000, Bangalore, India (2000), Pg.392-399.

19 Indian patent no: 655/Del/1996 titled “An Hingeless Control Surface”.

20 G.N. Dayananda, P. Senthil Kumar and M. Subba Rao, "Development of SMA based actuator mechanisms for deployment of control surfaces" Proceedings of Fourth International conference on Smart Materials, Structures and Systems, Bangalore, India (2005), Pg.SB131- SB138.

21 Indian patent no: 1063/Del/2002 "A novel device using shape memory and superelastic alloys for effecting and controlling swiveling movement"

22 G.N. Dayananda and V. Shankar, "The Design of a NiTi based Shape Memory Alloy Actuator" J. Aerospace Sci. Tech. 55 (2003), Pg.268-274.

23 I. Mihalcz, "Fundamental characteristics and design method for Nickel-Titanium shape memory alloy," J. Period. Polytech. Ser. Mech. Eng. 45 (1) (2001), Pg.75-86.

24 T.W. Duerig, Melton, D. Stockel and C.M. Wayman "Engineering Aspects of Shape Memory Alloys," Butterworth-Heinemann Ltd (1990), Pg.11, 12.

25 K. Otsuka and C.M. Wayman, "Shape Memory Materials," Cambridge University Press (1998), Pg.139.

26 K.W.K. Yeung, C.Y. Chung, K.M.C. Cheung, W.W. Lu and K.D.K. Luk, "Effect of Heat-Treatment on Phase Transition Temperatures of a Super elastic NiTi Alloy for Medical Use," Proceedings of the International Conference on Shape Memory and Super elastic technologies and Shape Memory Materials (SMST-SMM 2001), China (2001).

27 D. Faviera, Y. Liub, L. Orgeasa, A. Sandela, L. Debovea and P.Comte-Ga, "Influence of thermomechanical processing on the super elastic properties" Mater. Sci. Eng. A 429(1-2) (2006) 130-36.

28 X.J. Yan, D.Z. Yang and X.P. Liu, "Influence of heat treatment on the fatigue life of a laser-welded NiTi alloy wire," J. Mater. Character 58 (2007), Pg.262-266.

29 S. Zinelis, T. Takase, K. Ogane, G.D. Papadimitriou, M. Darabara, “The effect of thermal treatment on the resistance of nickel-titanium rotary files in cyclic fatigue,” J. Mater. Character. 103 (2007), Pg.843-847.

30 J. Frenzel, J. Pfetzing, K. Neuking and G. Eggeler, “On the influence of thermomechanical treatments on the microstructure and phase transformation behaviour of Ni-Ti-Fe shape memory alloys,” Mater. Sci. Eng. A 481-482 (2008), Pg.635-638.

31 Q.S.Liua, X. Maa, C.X. Linb and Y.D. Wub, “Effect of the heat treatment on the damping characteristics of the NiTi,” Mater. Sci. Eng. A 438-440 (2006), Pg.563-566.

32 H. Li, Chen-Xi Mao and Jin-Ping Ou “Strain self-sensing property and strain rate dependent constitutive model of austenitic shape memory alloy: Experiment and theory,” J. Mater. Civil Eng. 17-6 (2006), Pg. 676-685.

33 V. Novak, G.N. Dayananda, P. Sittner and K.K. Mahesh, “On the electric resistance variation of NiTi and NiTiCu SMA Wires in thermo mechanical tests,” ESOMAT Conference, Bochum, Germany (2006).

34 V. Antonucci, G. Faiella, M. Giordano, F. Mennella and L. Nicolais, “Electrical resistivity study and characterization during NiTi phase transformations,” J. Thermo. Acta 462 (2007), Pg.64-69.

35 M. Pozzi and G. Airoldi, “The electrical transport properties of shape memory alloys,” J. Smart Mater. Struct. 273-275 (1999), Pg. 300-304.

36 J. Uchil, K.K. Mahesh, K.G. Kumara, “Electrical resisitivity and strain recovery studies on the effect of thermal cycling under constant stress on R-Phase in NiTi shape memory alloy,” Physica B 324 (2002), Pg.419-428.

37 G. Airoldi, D.A. Lodi and M. Pozzi, “The Electric Resistance of Shape Memory Alloys in the Pseudoelastic Regime,” IVth European symposium on martensitic transformations, J. Phys. IV France 07 (1997), Pg.C5-507-C5-512.

38 J.L. Jin and Y.H. Chi, "Mechanical Properties and Electrical Resistance of TiNi Shape Memory Alloy," Proceedings of the International Conference on Shape Memory and Super elastic technologies and Shape Memory Materials

a. (SMST-SMM 2001), China (2001).

39 V. Kafka and D. Vokoun, "Background of two characteristic features of shape memory phenomena," J. Intel. Mater. Sys. Struct. 17 (2006), Pg.511-520.

40 R. DesRoches, M.ASCE, Jason McCormick, and Michael Delemont "Cyclic Properties of Superelastic Shape Memory Alloy Wires and Bars," J. Struct. Eng. 130 (1) (2004), Pg.38-46.

41 M. Dolce, D. Cardone "Mechanical behavior of shape memory alloy for seismic applications 2. Austenite NiTi wires Subjected to tension," Int. J. Mech. Sci. 43 (2001), Pg.2657-2677.

42 C. Brinson, I. Schmidt, and R. Lammering "Stress-induced transformation behavior of a polycrystalline NiTi shape memory alloy: micro and macro mechanical investigation via in situ optical microscopy," J. Mech. Phys. Sol. 52 (2004), Pg.1549-1571.

43 Sia Nemat-Nasser, Wei-Guo "Superelastic and cyclic response of NiTi SMA at various Strain rates and temperatures" J. Mech. Mater. 38 (2006), Pg. 463-474.

44 J.V. Humbeeck, and L. Delaey "The influence of strain rate, amplitude and temperature on the hysteresis of a pseudo elastic Cu-Zn-Al single crystal", Colloque c5, J. De Phys. (1981), Pg.1007-1011.

45 R.A. Raghavendra, J. Fengchun, S.V. Kenneth, T.G. George III, "Response of NiTi shape memory alloy at high strain rate: A symmetric investigation of temperature effects on tension-compression asymmetry," Acta Mater. 54 (2006), Pg. 4609-4620.

46 I. Aaltio, M. Lahelin, O. Soderberg, O. Heczko, B. Lofgren, Y. Ge, J. Seppala and S.P. Hannula, “Temperature dependence of the damping properties of Ni-Mn-Ga alloys,” J. Mater. Sci. Eng. A 481-482 (2008), Pg.314-317.

47 R. Ahluwalia, T. Lookman and A. Saxena, “Dynamic strain loading of cubic to tetragonal martensites,” J. Acta. Mater. 54 (2006), Pg.2109-2120.

48 P.H. Lin, H. Tobushi, “Influence of Strain Rate on Deformation Properties of NiTi Shape Memory Alloy,” Int. J. JSME. A 39 (1) (1996), Pg. 117–123.

49 H. Tobushi, Y. Shimeno, “Influence of Strain Rate on Superelastic Properties of TiNi Shape Memory Alloy,” J. Mech. Mater. 30 (1998), Pg. 141–150.

50 K.N. Melton, O. Mercier, “Fatigue of NiTi thermo elastic martensites,” J. Acta. Metal. 27 (1978), Pg.137-144.

51 George E. Dieter 1988 “Mechanical metallurgy” Materials Science and Metallurgy, McGraw-Hill Book Company (UK) Limited (1988) Pg.285-287, 387-394.

52 J.M. Young, Krystyn J.Van Vliet ‘Predicting *In Vivo* failure of pseudoelastic NiTi devices under low cycle, high amplitude fatigue’ J Biomed Mater Res Pt B Appl Biomater. 72B (2005) 17-26

53 R. Matsui, H. Tobushi, Y. Furuichi and H. Horikawa, “Tensile deformation and rotating-bending fatigue properties of a highelastic thin wire, a superelastic thin wire, and a superelastic thin tube of NiTi alloys,” J. Eng. Mater. Tech. 126 (2004), Pg.384-391.

54 C.J.D. Araujo, M. Morin and G. Guenin, “Fatigue behaviour of NiTi-Cu thin wires SME,” colloque C5, J. De. Phys. 7 (1997), Pg. C5.501-C5.506.

55 R.L. Holtz, K. Sadananda, M.A. Imam, 1999 “Fatigue thresholds of NiTi alloy near the shape memory transition temperature” Int. J. Fatigue 21 (1999), Pg.S137-S145.

56 R.M. Tabanli, N.K. Simha, B.T. Berg, “Mean stress effects on fatigue of NiTi,” Mater. Sci. Eng. A 273-275 (1999), Pg.644-648.

57 R. Lahoz, J.A. Puertolas, “Training and two-way shape memory in NiTi alloys: influence on thermal parameters,” J. Alloys and Comps. 381 (2004), Pg.130-136.

58 Young Liu, Zeliang Xie, Jan Van Humbeeck, “Cyclic deformation of NiTi shape memory alloys” Mater. Sci. Eng. A 273-275 (1999), Pg. 673-678.

59 A. Yawny, J. Olbricht, M. Sade and G. Eggeler, “Pseudoelastic cycling and ageing effects at ambient temperature in nanocrystalline Ni-rich NiTi wire,” J. Mater. Sci. Eng. A 481-482 (2008), Pg.86-90.

60 W. Yan, C.H. Wang, X.P .Zhang and Y-W. Mai, “Theoretical modeling of effects of plasticity on reverse transformation in superelastic shape memory alloys,” J. Mater. Sci. Eng. 354 (2003), Pg-146-157.

61 L. S-Sulpice and S.A. Chirani and S. Calloch, “Super-elastic behavior of shape memory alloys under proportional cyclic loadings,” Mater. Sci. Eng. A 481-482 (2008), Pg.174-177.

62 X. Wang, B. XU and Z. Yue, “Phase transformation behaviour of pseudoelastic NiTi shape memory alloys under large strain,” J. Alloys. Comps. 463 (2008), Pg.417-422.

63 X.P. Zhang, H.Y. Liu, B. Yuan and Y. Pzhang, “Superelasticity decay of porous NiTi shape memory alloys under cyclic strain-controlled fatigue conditions,” J. Mater. Sci. Eng. A 481-482 (2008), Pg.170-173.

64 D. Roy, V. Buravalla, P.D. Mangalgiri, S. Allegavi and U. Ramamurthy, “Mechanical characterization of NiTi SMA wires using a Dynamic mechanical analyzer,” Mater. Sci. Eng. A 494 (2008), Pg.429-435.

65 N. Nayan, D. Roy, V. Buravalla and U. Ramamurthy "Unnotched fatigue behavior of an austenitic Ni–Ti shape memory alloy" Mater. Sci. Eng. A (2008), doi:10.1016/j. msea.2008.07.025.

66 N. Siredey, A. Hautcoeur and A. Eberhardt, "Lifetime of superelastic Cu-Al-Be single crystal wires under bending fatigue," Mater. Sci. Eng. A 396 (2005), Pg.296-301.

67 G. Eggeler, E. Hornbogen, A. Yawny, A. Heckmann and M. Wagner, "Structural and functional fatigue of NiTi shape memory alloys," Mater. Sci. Eng. A 378 (2004), Pg.24-33.

68 B. Del Monte and R.P. Barone, United Technologies Corp., U.S. Patent for "A Crashworthy Landing Gear for an Aircraft," No. CA 2205489, (1994).

69 A. Airoldi and G. Janszen, "A Design Solution for a Crashworthy Landing Gear with a New Triggering Mechanism for the Plastic Collapse of Metallic Tubes," J. Aerospace Sci. Tech. 9 (2005), Pg. 445–455.

70 N.S. Philips, R.W. Carr and R.S. Scranton, "Crashworthy Landing Gear Study," U.S. Army Air Mobility Research and Development Laboratory Tech. Rept. (1973), Pg.72-61.

71 C.-H Tho, C.E. Sparks, A.K. Sareen, M.R. Smith and C. Johnson, "Efficient Helicopter Skid Landing Gear Dynamic Drop Simulation Using LS-DYNA," Proceedings of the American Helicopter Society 59th Annual Forum, American Helicopter Society International, Inc., Alexandria, VA (2003).

72 B.E. Stephens and W.L. Evans, "Application of Skid Landing Gear Dynamic Drop Analysis," Proceedings of the American Helicopter Society 55th Annual Forum, American Helicopter Society International, Inc., Alexandria, VA (1999), Pg.1644-1652.

73 A. Airoldi and L. Lanzi, "Multi-Objective Genetic Optimization form Helicopter Skid Landing Gears," Proceedings of the 46th AIAA/ASME/ ASCE/AHS/ASC

Structures, Structural Dynamics, and Materials Conference, American Institute of Aeronautics and Astronautics, Inc., Washington, D.C., (2005).

74 A.K. Sareen, M.R. Smith and J.V. Howard, “Helicopter Skid Gear, Dynamic Drop Analysis and Test Correlation,” Proceedings of the American Helicopter Society 54th Annual Forum, American Helicopter Society International, Inc., Alexandria, VA (1998), Pg.1267-1274.

75 J. Van Humbeeck, “Shape Memory Alloys: A Material and a Technology,” J. Adv. Eng. Mater. 3 (2001), Pg. 837–849.

76 M.C.Y. Niu, Composite Aircraft Structures, Conmilit Press Ltd (1993).

77 CIBA-GEIGY, Instruction sheet no. T.91b (1990).

78 Design studies on a Demonstrator Radio-Controlled Lighter-Than-Air-Vehicle, I-888-01/C-CADD/PD 0105 (2005).

79 Tinius Olsen T-series Tensile Test Machines instruction manual (2004).

Zwick technical manual Z150/SN5A.

80 ASTM standard D 3039 “Tensile testing of fiber composite materials”.

81 ASTM standard D 5228 “In plane shear testing of fiber composite materials”.

82 NAL test report; DOC.NO.RCBLIMP-TESTREP-01 “Dog ear test report”.

83 G.A. Khoury and J.D. Gillett, “Airship Technology,” Cambridge Univ. Press, Cambridge, England, U.K (1999), Pg.11.

84 Z H. Karadeniz and Dilek Kumlutans “A numerical study on the coefficients of thermal expansion of fiber reinforced composite materials,” J. Comp. Struct. (2007), Pg.1-10.

85 K. Okubo, T. Fujii and Y. Yamamoto, “Development of bamboo-based polymer composites and their mechanical properties,” J. Comp. Struct. 35 (2005),Pg.377-383.